

# **Scattering of Light by Plasmonic and Dielectric Nanoparticles and its Application in Subwavelength Imaging**

Yasaman Kiasat Dolatabadi

NATIONAL UNIVERSITY OF SINGAPORE

2014

# **Scattering of Light by Plasmonic and Dielectric Nanoparticles and its Application in Subwavelength Imaging**

Yasaman Kiasat Dolatabadi

A THESIS SUBMITTED FOR THE DEGREE OF  
DOCTOR OF PHILOSOPHY  
DEPARTMENT OF ELECTRICAL AND COMPUTER ENGINEERING  
NATIONAL UNIVERSITY OF SINGAPORE

2014

Statement of Originality

I hereby certify that the content of this thesis is the result of work done by me and has not been submitted for a higher degree to any other University or Institution.

.....24.01.2014.....

Date

Yasaman Kiasat

## **Acknowledgments**

There are many people whom I wish to thank for the help and support they have given me throughout my PhD studies. Foremost, I would like to express my sincere gratitude to my supervisors Dr. Li Er Ping and A/P. Chen Xudong. I am grateful for their invaluable guidance, insights and suggestions which helped me throughout this work. Besides my advisors, I would like to thank Professor Boris Luk'yanchuk , Dr Zsolt Szabo for their support. Last but not the least, I would like to thank my parents, my brother, and my sister and my friends for always being there when I needed them most, and for supporting me through all these years. Especially, I would like to thank my dear friend Syiavash for standing by me through tough time.

Finally, I wish to acknowledge my PhD study is sponsored by Agency of Science, Technology And Research (A\*STAR),Singapore under the postgraduate program.

# Summary

As a beam of light hits an object, the object's information is transferred to the scattered light with various wave vectors including both propagating and evanescent components. The propagating components carry the large features of an object and can reach the far field, while the miniature details of any object are carried by the scattered evanescent components, localized in the object's near field, and cannot reach the far field. Consequently, the resolution of the ultimate image is always "diffraction-limited". During the past decade, numerous efforts have been devoted to overcome diffraction limit. The near-field scanning optical microscope (NSOM/SNOM) enables a resolution of a few ten nanometers by collecting the evanescent waves localized in the objects near field. However, it has many limitations, related to a very low working distance and extremely shallow depth of field. Also the transmission efficiency of a small aperture is very low. It also takes a long time for scanning over a large sample area for a high resolution imaging. The diffraction limit can be also overcome by some other techniques, e.g. with surface-plasmon superlenses, nanoscale solid-immersion-lens and molecular fluorescence microscopy, negative refractive index super lens which is related to the enhancement of evanescent waves within a slab of artificial material with a negative refractive index and far-field super lens (FSL).

In spite of the impressive progress in this field, surface plasmon polariton (SPP) energy loss, sophistications in nanofabrication, specific laser sources, and parameter configuration of SPP excitation are factors which hamper far-field and near-field subwavelength imaging in the whole visible spectrum. In various fields of science, technology and medicine there is a continual need to obtain increasingly higher resolution images.

This research is motivated by the opportunity to develop an artificial media with effective optical property to manipulate light for the application in subwavelength imaging. Analytic and numerical investigation is allocated to apply the field that is scattered by metallic or dielectric nanoparticles, for the

near-field and far-field subwavelength imaging. An aggregate of plasmonic nanoparticles with different shapes and orientations are embedded in a dielectric host is studied for near-field tunable subwavelength imaging. An effective medium theory is extended to the optical range to homogenize the optical property of the metal-dielectric mixture. Optimal values for shape, dimension, and orientation of nanoparticles and their probability distribution function (PDF) are provided for successful near-field subwavelength imaging for different frequencies in the optical range.

Far-field subwavelength imaging with a dielectric particle in white light source is studied to overcome (i) the sensitivity of plasmon resonance on the frequency of the incident light, (ii) inevitable metal loss in metal-based subwavelength imaging techniques. A complete analytical explanation of near-field virtual image formation by dielectric micro-spheres is presented for the first time.

# Contents

Acknowledgments	i
Summary	ii
List of Figures	vii
List of Tables	xv
Acronyms	xvi

## Chapter 1

### Introduction

1.1 Negative Index of Refraction and Super Resolution	1
1.2 Negative Refraction in Optical Regime	5
1.3 Estimation of the Unit Cell Size of Metamaterials for Subwavelength Imaging	7
1.4 Near Field Superlens	10
1.5 Motivation	12
1.6 Thesis Outline	14
Reference	17

## Chapter 2

### The Validation of Maxwell-Garnett effective Medium Theory

2.1 Introduction	19
2.2 Assumptions of Effective Medium Model	19
2.3 The Size of the Nanoparticles	20
2.4 Geometry of Nanoparticles Assembly	28
2.5 General Bounds for Effective Medium Theory	31

2.6 Conclusion	34
Reference	36

### **Chapter 3**

#### **Tunable Subwavelength Imaging with Metal-Dielectric**

3.1 Effective Medium Theory	38
3.2 Optics of a Single Homogenous Isotropic Layer	44
3.3 Tunable Composite Superlens	47
3.4 Optimized single layer tunable composite superlens	51
3.5 Imaging with Multilayer Composite Superlens	56
3.6 Conclusions	61
Reference	62

### **Chapter 4**

#### **Subwavelength Imaging with Metal Dielectric Composite Made of Non-Spherical Nanoparticles**

4.1 Introduction	63
4.2 Effective Medium Theory for composites with non-spherical nano particles	64
4.3 Polarisability components of an ellipsoid	65
4.4 Effective Permittivity of composites made of randomly oriented inclusions	66
4.4.1 Randomly oriented inclusions	67
4.5 Imaging with randomly oriented non-spherical nano particles	68
4.5.1 Subwavelength imaging with single layer composite lens	69
4.5.2 Subwavelength imaging with layered composite-dielectric lens	71
4.6 The effect of the shape	73
4.7 Effective Permittivity of composites made of aligned inclusions	74
4.8 The importance of systematic solution for wave propagation in layered anisotropic medium	76
4.8.1 Explicit Expressions for E-Field and H-Field Polarizations	79
4.8.2 General Transfer Matrix	81
4.8.3. The Transfer Function Development	82



4.9 Imaging with aligned non-spherical nano particles	86
4.10 Conclusion	92
Reference	94

## **Chapter 5**

### **Analytic investigation of Magnified Virtual Image Formation in Near-Field with Microscope**

5.1 Introduction	97
5.2 Near Field Optics, Microscopic vs. Mesoscopic	99
5.3 Optical Resonance and Near-Field Enhancement Effects	101
5.4 Theoretical challenge for Light Interaction with Mesoscopic Structures	102
5.5 Formulation of the Problem and Methodology	103
5.5.1 Rigorous Multipole Expansion	107
5.5.2 Scattered Field	111
5.5.3 Verification of Calculations	116
5.5.4 Poynting vector lines extrapolation and virtual image formation	121
5.6 Conclusion	128
Reference	130

## **Chapter 6**

### **Conclusion and Future Work**

6.1 Conclusion	131
6.2 Suggestion for Future Work	136

<b>List of Publication</b>	139
----------------------------	-----

## List of Figures

Figure 1.1	The proposed amplification of evanescent waves in a perfect lens	2
Figure 1.2	Experimental verification of double negative materials in optical range(a) A schematic of the array of paired nanorods (b) Field-emission scanning electron microscope images of the fabricated array and a single pair of nanorods	6
Figure 1.3	Fishnet structure: (a) resonant magnetic structure with non-resonant electric grating, and (b) Electron microscope images of the fabricated material.	6
Figure 1.4	The requirement of high spatial harmonics for subwavelength imaging (a) the Fourier transform of the source and the Transfer Function, (b) the intensity distribution of the source and image: the highest spatial harmonic which is passed has a wavelength of 21.24 nm.	8
Figure 1.5	The quality of the image as a function of the bandwidth of the transfer function. The error function is the sum of absolute difference of the intensity of the field in object plane and image plane, figure 1.4 (b), which is normalized to the number of samples in the space domain	9
Figure 1.6	Optical super lensing with silver slab operating near Ultra-violet wavelength	11
Figure 2.1	UV-visible absorption spectra of 9, 22, 48, and 99 nm gold nano particles in water	23

Figure 2.2	Decomposition of the electric permittivity of silver into free and bound electron contributions. In (a) the real part, while in (b) the imaginary part of the electric permittivity is shown	25
Figure 2.3	Dielectric function for nanoparticles with different radius (a) Real part (b) Imaginary part	26
Figure 2.4	The effective permittivity of metal dielectric composites made of silver nanospheres with different radius (a) Real part (b) Imaginary part	26
Figure 2.5	Normalized scattering coefficients for different sizes of silver nanoparticle embedded in SiO <sub>2</sub> (a) the contribution of higher order modes for nano particles (b) the particle radius that the second harmonic contribution becomes prominent	27
Figure 2.6	A cell of composite medium immersed inside the effective homogenous background	28
Figure 2.7	Wiener bounds (W) and Hashin-Shtrikman (HS) bounds and MG theory for the effective permittivity of a mixture with $\epsilon_i = 2.5$ and $\epsilon_e = 1$ (a) The spherical inclusions $\epsilon_i$ in the environment $\epsilon_e$ (b) The spherical inclusions $\epsilon_e$ in the environment $\epsilon_i$	33
Figure 3.1	Macroscopic structure of (a) Maxwell-Garnett (b) Bruggeman	38
Figure 3.2	Lorentz sphere concept for calculating local field	39
Figure 3.3	the effective complex permittivity of silver nanoparticles embedded in silica host for different filling fractions of silver (a) Real part (b) Imaginary part	41
Figure 3.4	Effective permittivity of silver silica composite	42

approximated by MG theory (a) Negative permittivity for sub-wavelength in different wavelength is realized by composite super lens (b) the amount of composite's loss is smaller in comparison with bulk silver

Figure 3.5	Effective permittivity of silver silica composite approximated by Bruggeman theory (a) Real part (b) Imaginary part	43
Figure 3.6	Reflection and transmission of TM wave at the semi-finite isotropic-isotropic interface	44
Figure 3.7	Forward and backward propagating TM waves	45
Figure 3.8	Transfer function of silver slab CST simulation versus analytical calculation (a) Schematic of silver slab in CST (b) Agreement of analysis and simulation	47
Figure 3.9	Imaging system set up	49
Figure 3.10	$\lambda=397$ nm, Slab thickness = 20 nm, (a) Composite ( $\epsilon = -1 - i 0.172$ ) (b) Silver ( $\epsilon = -3.71 - i 0.059$ )	50
Figure 3.11	$\lambda=385$ nm, Slab thickness = 30 nm, (a) Composite ( $\epsilon = -1 - i 0.092$ ) (b) Silver ( $\epsilon = -3.51 - i 0.054$ )	50
Figure 3.12	$\lambda=375$ nm, Slab thickness = 30 nm, (a) Composite ( $\epsilon = -1 - i 0.067$ ) (b) Silver ( $\epsilon = -2.78 - i 0.05$ )	50
Figure 3.13	Design of the imaging device with the single layer composite lens. The first column refers to the lens with thickness of 20 nm and surrounded with air, while in the second column the thickness of the lens is 30 nm and it is surrounded with SiO <sub>2</sub> . The error surfaces, which are	55

searched by the optimization procedure are presented in (a) and (b). The markers indicate optimized results obtained with constraints on the filling factor. The transfer functions of the composite lenses are presented in (c) and (d). The intensity distributions in the source and image planes are plotted in (e) and (f). For reference the transfer function and the image without the lens are presented as well

Figure 3.14	The intensity distributions in the image plane corresponding to points 1-4 of figure 3.13 (a) and (b). Intensity in the image plane formed by (a) air-composite-air (b) SiO <sub>2</sub> -composite-SiO <sub>2</sub>	56
Figure 3.15	The configuration of the multilayer lens	57
Figure 3.16	Transfer function of silver-PMMA layered structure CST simulation versus analytical calculation (a) &(b) Schematic of silver slab in CST (c) Magnitude of transfer function (d) Phase of the transfer function	58
Figure 3.17	Imaging with the multilayer lens. In (a) the transfer functions, and in (b) the images corresponding to the parameters presented in Table 3.2 are shown. The intensity distribution of the source and of the image for the lens, with parameters presented in the fourth row of the table3.2, along with the reference image without the lens are shown in (c)	60
Figure 4.1	The geometry of an ellipsoid. The semi-axes $a_x$ , $a_y$ and $a_z$ fix the Cartesian co-ordinate system.	64
Figure 4.2	A composite randomly oriented nano-ellipsoid particles	67
Figure 4.3	the optical property of mixture with randomly oriented ellipsoids	68

Figure 4.4	The image formation of the imaging system made of composite thin film layers separated with dielectric slabs	69
Figure 4.5	Subwavelength imaging (a) with and without lens (b) imaging with single layer composite-dielectric lens for composite made of inclusions with different ellipsoidal shape	70
Figure 4.6	(a) Subwavelength imaging with and without multilayer composite-dielectric lens (b) imaging with multilayer composite-dielectric lens for composite with inclusions of different ellipsoidal shape	72
Figure 4.7	The effect of the shape of inclusions on the effective permittivity (a) real part, (b) imaginary part of metal-dielectric composite. The metallic inclusions are Ag embedded in SiO <sub>2</sub> as a host medium. The filling fraction for all composites is 0.5	74
Figure 4.8	A composite with aligned nano-ellipsoid particles	75
Figure 4.9	The optical property of mixture with aligned ellipsoids	75
Figure 4.10	Incidence, reflectance and transmittance of a plane wave	82
Figure 4.11	Transfer matrix development flowchart for the $l_{th}$ layer	83

Figure 4.12	Imaging with composite made of aligned nano-ellipsoid VS Imaging with composite made of randomly oriented nano-ellipsoid (a) Subwavelength imaging with composite made of randomly oriented prolates and composite made of aligned prolates (b) Tensor of effective permittivity (c) Real part of permittivity tensor for the frequency that the imaging is realized (d) Imaginary part of permittivity tensor for the frequency that the imaging is realized	88
Figure 4.13	Imaging with composite made of aligned nano-ellipsoid VS Imaging with composite made of randomly oriented nano-ellipsoid (a) Subwavelength imaging with composite made of randomly oriented discs and composite made of aligned discs (b) Tensor of effective permittivity (c) Real part of permittivity tensor for the frequency that the imaging is realized (d) Imaginary part of permittivity tensor for the frequency that the imaging is realized	90
Figure 4.14	The success of composite slab made of aligned inclusions in subwavelength imaging for higher resolution	91
Figure 5.1	Subwavelength focusing of light by dielectric nanosphere $\epsilon_r = 2.56$ $a = 200 \text{ nm}$ at $\lambda = 248 \text{ nm}$	101
Figure 5.2	Magnified Virtual Image Formation (a) Virtual image forms by glass lens (b) Ray tracing technique to determine virtual image formation in geometrical optics	104
Figure 5.3	Experimental configuration of white-light microscope with $\lambda/8 - \lambda/14$ imaging resolution. Schematic	104

of the transmission mode microsphere superlens integrated with a classical optical microscope. The spheres collect the near-field object information and form virtual images that can be captured by the conventional lens

Figure 5.4	Analytical investigation of virtual image formation in the near-field with the system of two radiating dipole and dielectric microsphere. The dielectric microsphere operates as a superlens to create magnified virtual image of two dipoles	105
Figure 5.5	The test set up. The sphere is located at the far-field region of the dipole	116
Figure 5.6	The intensity of E-Field, inside and outside of a dielectric sphere (a) Full wave based algorithm in MATLAB for general case of dipole radiation in presence of sphere when dipole is set far away from the sphere as shown in figure 5.5 (b) COMSOL multiphysics simulation the same sphere shined by a plane wave	120
Figure 5.7	Virtual image formation investigation	121
Figure 5.8	Reciprocal configurations	122
Figure 5.9	Magnified virtual image formations in the near-field (a) Extrapolation of Poynting vector. Solid navy lines represent the Poynting vector found by equation (5.54), dashed green line is the boundary of microsphere, and dashed red lines are used to extrapolate the Poynting vector lines. The image plane is located 273 nm below the microsphere (b) energy vortex formation	124



Figure 5.10	Ray-tracing for a big particle with small $n$	125
Figure 5.11	Magnified virtual image formation in near field = 40 nm (a) Convergence of extrapolated intensity lines (b) Energy vortex	126
Figure 5.12	Magnified virtual image formation in the near-field $d = 64 \text{ nm}$ (a) Ultimate achievable resolution $\approx \lambda/10$ (b) Energy vortex	127

## List of Tables

Table 3.1	relative effective permittivity for silver-silica composite and relative permittivity for $\epsilon$ for bulk silver	49
Table 3.2	The filling factor, the frequency and the effective electric permittivity of the single layer composite lens	54
Table 3.3	The design parameters of the multilayer lens	59
Table 4.1	Optimized parameters for subwavelength imaging with single layer composite- dielectric lens	71
Table 4.2	Optimized parameters for subwavelength imaging with layered composite-dielectric lens	73
Table 4.3	Optimized parameters for subwavelength imaging with single layer of composite made of aligned inclusions	90

# Acronyms

NIM	Negative Index Material
TM	Transverse Magnetic
EBL	Electron-Beam Lithography
FDTD	Finite Difference Time Domain
TMM	Transfer Matrix Method
MG	Maxwell-Garnett
PDF	Probability Distribution Function
E-field	Electric Field
H-field	Magnetic Field
Far-field Super Lens	FSL
Nanoscale Solid Immersion Lens	nSIL
Near Field Optics	NFO
Sphere Cavity Resonance	SCR

# CHAPTER 1

## INTRODUCTION

### 1.1 Negative Index of Refraction and Super Resolution

It is well-known that the resolution of conventional optical imaging systems is restricted by the Abbe diffraction limit. The observation of the subwavelength details of an object is difficult due to the considerable attenuation of the scattered waves with high spatial frequency, in the nano-metric vicinity of the object. In 2000, John Pendry from the Imperial College of London made a groundbreaking prediction and, mathematically demonstrated that the negative index material (NIM) slab not only focuses propagating waves, but also turns the evanescent decay of the near-field to exponential amplification [1]. The electric component of the scattered field from an object can be given by [1],

$$E(r, t) = \sum_{\sigma, k_x, k_y} E_{\sigma}(k_x, k_y) \exp(j\omega t - (jk_z z + jk_x x + jk_y y)), \quad (1.1)$$

Here the  $z$  axis is considered to be the axis normal to the lens. According to the Maxwell's equations:

$$\begin{cases} k_z = \sqrt{\omega^2 \mu \epsilon - k_x^2 - k_y^2} & \text{propagating component } (k_x^2 + k_y^2 < \omega^2 \mu \epsilon) \\ k_z = -j\sqrt{\omega^2 \mu \epsilon - k_x^2 - k_y^2} & \text{evanescent component } (k_x^2 + k_y^2 > \omega^2 \mu \epsilon) \end{cases}, \quad (1.2)$$

Taking advantage of the negative phase property of the NIM slab, the spatial harmonics,  $k'_z$ , in the NIM slab will be of the following form

$$k'_z = -k_z. \quad (1.3)$$

Consequently the property of phase reversal of the NIM slab is observed, resulting in reconstruction of every spatial frequency component carried with the scattered light. Imaging with the help of the near-field is now possible for an electromagnetic lensing system and in the case of no material losses a perfect image could be reconstructed, Pendry dubbed this slab a ‘perfect lens’. Furthermore, Pendry suggested that a silver slab exposed with Transverse Magnetic (TM) polarization under UV light could act as a near-field perfect lens or superlens. This gave solid direction for a surface-Plasmon-mediated, sub100nm, super-resolution imaging system. Pendry dubbed the superlens as the ‘poor-mans perfect lens’. Figure 1.1 demonstrates the growth mechanism of an evanescent wave in a NIM slab where exponential decay becomes exponential amplification.

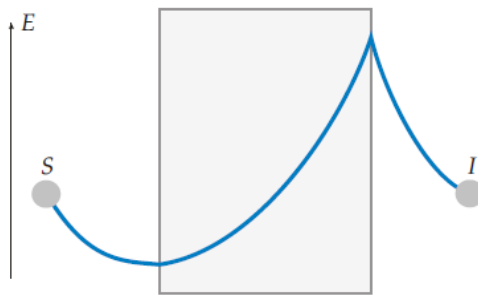


**Figure 1.1** The proposed amplification of evanescent waves in a perfect lens, reprinted with a permission of [2].

Pendry's paper added some much needed drive to the search for negative refraction, but progress from this point onwards would prove challenging. Pendry's general case was for a medium where  $\mu$  and  $\epsilon$  are exactly equal to  $-1$ , and specifically for a steady state environment. The effect of material losses was not studied in detail. Pendry stated that the concept was far from being a closed book, and he could not have been more correct. An intense debate broke out over whether a NIM was a realizable material. Initially, Hooft [3] and Williams [4] commented on Pendry's mathematical calculations and claimed there were errors in causality assumptions and believed the diffraction losses would cause some problems and even questioned whether a negative index material was a mathematical possibility. Pendry replied to these questions with [4,5] and concluded that their claims either did not apply to his summation or were wrong. However, Pendry stated that the simultaneous  $-1$  for  $\epsilon$  and  $\mu$  only occur at one frequency for any real material, due to the inevitability of strong dispersion with frequency. Consequently the flawless image of a real source will not be realizable since it will always radiate a bandwidth of frequencies. He also confessed to not being able to answer questions posed by Williams [4] relating to the diffraction losses in a subwavelength imaging system. Valanju *et al.* were the first group who questioned the physics of NIM materials and claimed that "causality and finite signal speed always prevent negative wave signal (not phase) refraction" [6]. Valanju *et al.* believed that they mathematically proved that the group velocity of a wave packet is always positively refracted and negative refraction only occurs for the phase velocity. In return, Pendry *et al.* [7] showed that Valanju *et al.* had

used a dual-frequency wave packet and failed to test a generalized wave packet and their claim was based on an incorrect definition of group velocity. In order to support their claim, Valanju *et al.* [8] mentioned that Pendry *et al.* unconsciously disproved their own case; they still believed that negative refraction violates causality. As support to the plausibility of negative refractive materials, Foteinopoulo *et al.* performed detailed numerical simulations to study the electromagnetic wave interactions at a free space-NIM interface and demonstrated that the causality was not violated [9]. Kolinko *et al.* also proved that negative refractive index material is passive and physically realizable via simulation [10]. They also investigated the imaging ability of a NIM slab and could resolve two sources which were  $\lambda/20$  apart. The debate over the perfect lens was continued by the most convincing paper by Garcia *et al.* who tried to prove that any source of loss would destroy any perfect imaging (specially, evanescent field amplification) [11]. Garcia *et al.* expressed his argument in [13] against Shelby *et al.* [12] where they attempted to prove negative refraction through the consistency of Snell's law for a negative refractive index. Garcia *et al.* argument was that the introduction of losses into Pendry's details of his original perfect lens paper destroyed any perfect lensing action. During 2003 there was a dramatic increase in publications who support Pendry's idea. At that time Pendry quoted, "It is time to move on and start making use of these amazing new materials." Perfect resolution might not be achievable completely due to inevitable metal's loss and material dispersion, but undoubtedly the developed and growing interest would result in materials that would perform similar functionality.

## 1.2 Negative Refraction in Optical Regime

Although NIMs were first developed for the microwave range, providing them for optical uses is important from application and theoretical perspective. Direct downward scaling of the microwave NIM structure is not a realistic method to achieve optical NIMs due to fabrication challenges and material limitations. The challenges in the optical regime are restricted not only to fabrication but also to experimental characterization. Experimental verification of negative refraction is achieved through the observation of the bending direction of the Poynting vector in the interface. Until now, most of the fabricated optical NIMs are of planar subwavelength thicknesses fabricated by optical or electron-beam lithography (EBL). Consequently the direct observation of negative bending beams of light is from a wedge shape made out of optical NIM is not feasible. The key to design optical NIM is to manage a spectral overlap of magnetic and electric resonance. A negative permittivity can be obtained using artificial materials consisting of a metallic structure which mimics Lorentz model through special design. After an early paper by Lagrakov and Sarychev about large paramagnetic responses by nanorods [13], and Podosky *et al.*'s work demonstrating the feasibility of diamagnetic responses by a pair of metal nano rods [14], the first optical metamaterial with negative index of refraction was experimentally demonstrated by a research group at Purdu University using a layer of paired metal nanorods (figure 1.2) [15]. An alternative current (AC) electric field parallel to both rods induces parallel currents in both rods, and the magnetic field oriented perpendicular to the plane of rods, causes anti-parallel currents in both rods causing a magnetic response of the



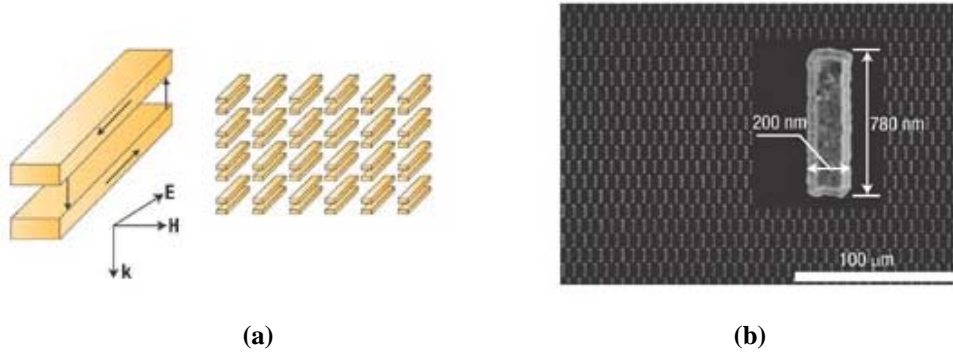


**Figure 1.2** Experimental verification of double negative materials in optical range (a) A schematic of the array of paired nanorods (b) Field-emission scanning electron microscope images of the fabricated array and a single pair of nanorods [15].

system. A common approach for the realization of optical metamaterial is to construct a magnetic resonant along with taking the advantage of a metallic structure which provides negative permittivity for a broad frequency range. Consequently the whole concept centers about generating an asymmetric current, which provides the magnetic resonance, in the optical range. This general guideline, results in a fishnet style structure, which currently is the most common form of negative index metamaterial at optical frequencies (Figure 1.3). Until now, extensive effort has been dedicated toward realizing the negative index of refraction in the optical range [16-20]. Although the negative index was achieved in certain optical frequencies the existence of unavoidable loss and material dispersion dramatically reduces for super resolution ( $\lambda/6$  or less) in the optical fr-

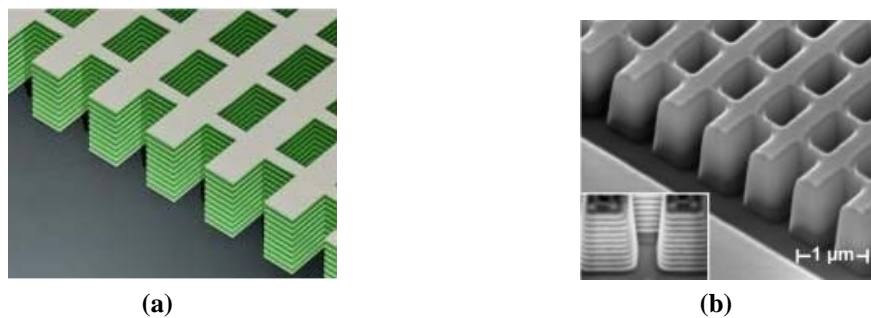


**Figure 1.3** Fishnet structure: (a) resonant magnetic structure with non-resonant electric grating, and (b) Electron microscope images of the fabricated material [18].

-equency. In addition to the loss and dispersion issues, a waveguide approach [21] and an estimate based on the Nyquist-Shannon sampling criteria, indicate that a resolution of 100 nm requires unit cell sizes of 20 nm or smaller. At this unit cell size, fabrication of the required negative magnetic response remains a challenge [22].

### **1.3 Estimation of the Unit Cell Size of Metamaterials for Subwavelength Imaging**

In order to investigate the requirements to be satisfied by metamaterial imaging systems, the ideal arrangement composed of the metamaterial slab with refractive index  $n = -1$  and thickness  $d$ , surrounded with air is considered. The source plane and the image plane are positioned at a distance  $d/2$  in front and behind of the slab, respectively. It is known, from system theory, that a system has ideal transmission if the transfer function has constant magnitude and linear phase. However, metamaterials are subwavelength periodic structures, with finite sized unit cells and unavoidable metal losses attributed to the building materials. Therefore, the transfer function cannot be ideal and the imaging system will have a spatial cutoff frequency corresponding to the highest spatial harmonic, which can be passed. The bandwidth of the transfer function characterizes the quality of the metamaterial imaging system. In the following, the transfer function of the ideal low pass filter is considered as the transfer function of the hypothetical metamaterial imaging system as it can be seen in figure 1.4 (a). The objective here is to investigate that for an object with subwavelength features how many spatial

harmonics required to pass by the lens, to form an image with the same subwavelength feature in the image plane.

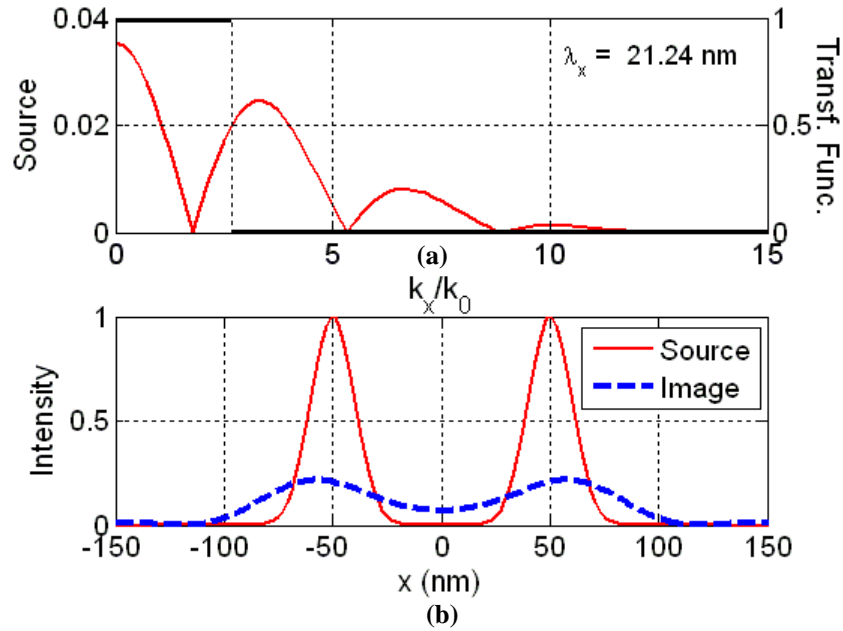


**Figure 1.4** The requirement of high spatial harmonics for subwavelength imaging (a) the Fourier transform of the source and the Transfer Function, (b) the intensity distribution of the source and image: the highest spatial harmonic which is passed has a wavelength of 21.24 nm.

The intensity distribution in the image plane is calculated by convolving the Fourier transform of the source field with the transfer function and then performing an inverse Fourier transform. The quality of the image, which is described by the absolute difference between the intensity distribution of the source and image, is investigated in function of the bandwidth of the transfer function. The source to be imaged is the double slot illuminated with monochromatic light of 357 nm wavelength. The intensity distribution in the source plane can be approximated with a double Gaussian function. The half width of this source is 20 nm and the peaks are positioned 100 nm apart. The magnitude of the source Fourier transform is plotted in red, in figure 1.4 (a), and the transfer function with cutoff at  $k_x/k_0 = 2.674$  is shown in black. The intensity

distribution in the image plane is plotted in figure 1.4 (b), where for reference; the intensity distribution of the source plane is also shown. Note that in the absence of the metamaterial, the two peaks are indistinguishable in the image plane and the parameters are configured in such a way that the peaks can be distinguished only when evanescent components are transmitted. Upon observing the image, the position of the two peaks can be distinguished with a proper threshold which can be determined by the noise level in the imaging system, however the magnitude and the half-width of the source cannot be accurately obtained. The evolution of the absolute difference between the source and image is a function of the cutoff frequency of the transfer function and is presented in figure 1.5.

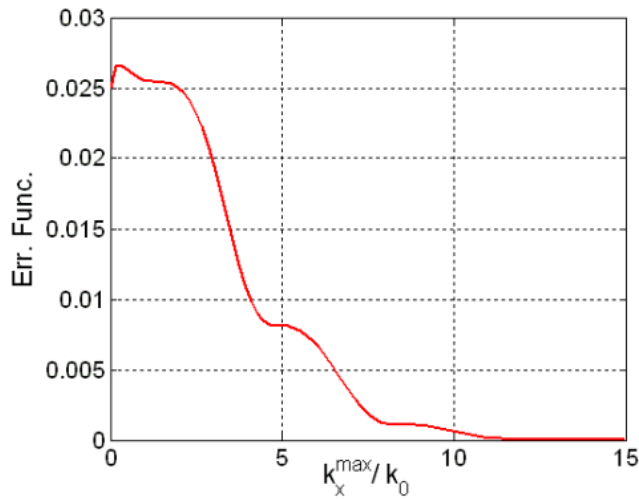


**Figure 1.5** The quality of the image as a function of the bandwidth of the transfer function. The error function is the sum of absolute difference of the intensity of the field in object plane and image plane, figure 1.4 (b), which is normalized to the number of samples in the space domain.

The more evanescent components passed by the imaging system, the better the quality of the image becomes. The Nyquist-Shannon sampling criterion indicates that the unit cell size of the metamaterial lens has to be smaller than half of the wavelength of the highest spatial harmonic transmitted by the system. In

the case of figure 1.4, the wavelength of the transmitted highest spatial harmonic is  $\lambda_x = 21.24\text{nm}$ . Therefore, the required metamaterial unit cell size should be 10 nm or less in order to obtain a resolution of 100 nm with a source wavelength of 357 nm.

With the development of the Finite Difference Time Domain (FDTD) method, extensive research has been performed to estimate the accuracy of the solution as a function of temporal and spatial discretization. The FDTD method requires four to ten times smaller unit cell sizes than the optical wavelength to propagate plane waves in a homogeneous medium with acceptable accuracy over a distance of a few wavelengths. At this unit cell size, it remains a challenge to fabricate the required negative magnetic response from resonant elements. Consequently, another alternative is to perform subwavelength imaging with TM polarized light which only requires negative permittivity [1].

## **1.4 Near Field Superlens**

As Pendry predicted in his early paper about super resolution [4], a silver lens can be the solution for TM polarization. Pendry suggested using a thin slab of silver as it naturally has a negative permittivity at ultraviolet (UV) wavelengths and additionally has relatively low loss compared with other metals, allowing imaging of the TM wave light components parallel to the lens. Silver achieves its surface plasmon (SP) resonance at a real relative permittivity of  $-1$  at  $\lambda = 338\text{nm}$  (with a loss term  $\epsilon' = 0.4$ ), and occurs when the SP oscillation is  $90^\circ$  out of phase with the electric field. Thus, the negative value of permittivity and hence the potential

focusing of the near-field through a thin layer of silver is mediated by strong SP oscillations. The growth of the evanescent waves is experimentally verified in [23]. The generation of a SP relies on the coupling between an electric field and longitudinal charge density oscillations at the interface between a metal and a dielectric. In order to transfer the amplified evanescent waves, the SP oscillations should be coupled from the first interface of “air-silver” to the second interface of “silver-air”. The efficiency of the coupling is proportional to the exponential of the thickness, and superlensing occurs till the slab’s loss dominates the amplification of evanescent waves. Figure 1.6 illustrates the experimental verification of imaging with a silver slab performed by Zhang *et al.* [24]. In Zhang’s experiment, near-field optical lithography was used to examine the imaging capability of a silver slab sandwiched between photoresist layers.

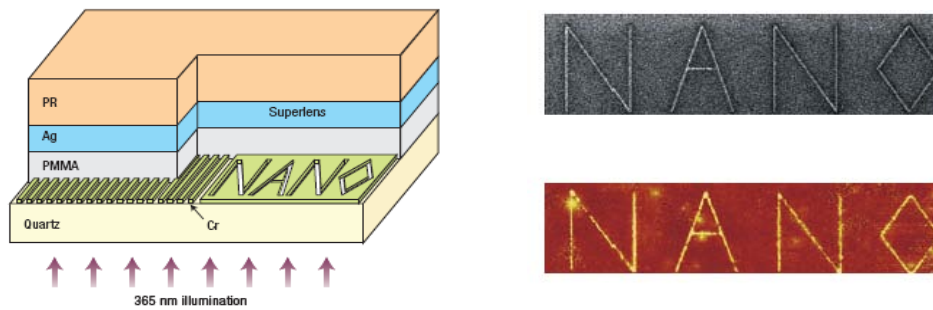


**Figure 1.6** Optical super lensing with silver slab operating near Ultra-violet wavelength [24]

The subwavelength imaging is realized at  $\lambda = 365$  nm for a grating with a 60-nm half pitch ( $\sim \lambda/6$ ).

## 1.5 Motivation

According to our observations that magnetism vanishes at higher frequencies for all natural materials and the refractive index is always positive, the research of

metamaterials has started with the goal of producing materials with a negative refractive index, i.e., simultaneous negative electric permittivity and magnetic permeability for imaging applications below the diffraction limit. However, the design of metamaterial lenses with a negative refractive index is not an easy task. Despite extensive research efforts, existing optical metamaterial based imaging systems work only for narrow frequency ranges of plane waves incident with a specific angle and polarization. Metals have a negative electric permittivity; therefore the main challenge of metamaterial research is to produce the required negative magnetic properties. The metamaterial structures proposed in the literature achieve the high frequency magnetism with subwavelength current loops or metallic structures, which can support anti-symmetric modes. The associated current flow produces a magnetic moment. A metamaterial with a customized optical response can be built as a superposition of resonant nano elements. The advances in nano-fabrication lead to possibilities to produce such subwavelength structures. The most common designs to produce artificial magnetism are variations of the split ring resonators and pairs of nano-rods. The single wires and cut-wire pairs can be arranged in so called “fishnet” geometries, leading to structures with consecutive negative electric permittivity and magnetic permeability at optical frequencies [16-20]. However, the resulting metamaterial based imaging system will have a cutoff frequency due to unavoidable losses and the finite size of the unit cell. As discussed in the next section, the required unit cell size can be estimated based on frequency domain analysis of image formation and the Nyquist-Shannon sampling criteria. The calculations indicate that 100 *nm*

resolution requires unit cell sizes smaller than 20 nm. At this unit cell size, it remains a challenge to fabricate the required negative magnetic response. For imaging applications, to overcome the difficulties of producing double negative metamaterial, it was shown that a metamaterial with negative permittivity, is suitable only for imaging transverse magnetic (TM) sources in the near field region. In the literature, this type of material is referred to as single negative metamaterial, and an experimental demonstration made using a 35 nm thick silver layer to obtain a resolution of approximately 65 nm [24]. Multilayer metal-dielectric systems were developed to increase the separation between the object and image plane [25].

However, metal based structures can only support subwavelength imaging in one frequency due to the monotone nature of dispersion curve. This situation can dramatically change when a composite metal-dielectric material is used as a superlens. The composite materials are engineered of naturally occurring materials made from two or more constituent substances with significantly different physical or chemical properties which remain separate and distinct at the macroscopic or microscopic scale within the finished structure. In contrast to metal slabs, metal-dielectric composite films are characterized by an effective permittivity  $\epsilon_{eff}$  that depends critically on the permittivities and filling factors of both the metal and dielectric components. The dependence of the effective dielectric permittivity on the light wavelength and on the metal filling factor is the key to realizing a tunable near-field superlens.



## 1.6 Thesis Outline

Chapter one provides a brief introduction to the application of negative index material (NIM) in subwavelength imaging and the challenge to fabricate such material.

Chapter two introduces a lattice of metallic nano particles embedded in a dielectric medium as an intriguing alternative of negative-epsilon slabs which overcomes the “solo-frequency” nature of near-field subwavelength imaging with metallic slabs. The material of the lens is a composite of spherical Ag nanoparticles embedded in a SiO<sub>2</sub> host material. The effective optical property of the metal dielectric composite is approximated from the direct solution of Poisson’s equation; the image formed by the lens is calculated by solving the Maxwell equations with the Transfer Matrix Method (TMM). The formula of the composite material, the optimum working frequency and the thicknesses of the layers are determined minimizing the absolute difference between the source and image. The details of the design procedure are presented, and optimized configurations obtained under different constrains are discussed. The main advantage of the composite lens is that it can eliminate the hotspots present in the images of a metallic superlens and the working frequency is tunable to the available industrial laser sources.

Chapter three presents a metal dielectric composite material with non-spherical metallic inclusions of different shapes, sizes and orientations that has higher degrees of freedom in imaging with available laser sources. The effects of

shape and alignment of nanoparticles are studied and an optimum single and multilayer lens system is designed with improved resolution and more robustness against metal's loss. In addition, as the composite material made with aligned inclusions has an anisotropic effective index of refraction, an analytical algorithm is developed to study the interaction of light with an arbitrary anisotropic layered structure. It is shown that subwavelength imaging in different wavelengths is heavily dependent on the shape of the nano-particles and one can perform imaging in the desired wavelength by changing the shape of the composite inclusions. It is also analytically demonstrated that the anisotropy of the composite material with aligned nanoparticles makes the imaging more robust to loss and enables one to perform subwavelength imaging for even higher resolutions due to different imaging mechanisms.

Chapter four pursues fundamental theoretical studies which extend the classic effective medium theory (Maxwell-Garnett (MG) here) to the optical range. In order to have a valid approximated optical property for the aggregate of nanoparticles, upper and lower limits are set for the geometry of nanoparticles and their PDF in the host medium by analytical calculation. The general assumptions and bounds of effective medium theory is discussed and the validity of MG theory is tested.

Although imaging with a metal dielectric composite overcomes several difficulties apparent with metallic slabs, such as formation of hot spots and imaging in only one frequency, the performance of the composite lens is still hampered by metal loss and sensitivity of Plasmon resonance to the frequency of

the incident field. Particularly the loss forces, the metal-based flat superlenses to perform only in near-field region.

Chapter five presents the analytical investigation of subwavelength far-field imaging in a white light source with dielectric particles. A complete analytical explanation of near-field virtual image formation by a dielectric microsphere is presented for the first time, and the phenomenon is explained by the exact solution of Maxwell's equation. The derived explicit solution and developed algorithm reconstructs Mie theory completely in the simplest form of the problem. It is shown that only evanescent waves, which carry high frequency spatial subwavelength information, are responsible for the formation of a near field image. It is also demonstrated analytically that while the evanescent waves improve the resolution of the real image, the imaging performance is due to nanoscope's subwavelength near field focusing size.

## 1.7 Reference

- [1] J. B. Pendry. "Negative refraction makes a perfect lens." *Phy. Rev. Lett.* 85.18: 3966, (2000).
- [2] D. O. Melville. "Planar Lensing Lithography: Enhancing the Optical Near Field." (2006).
- [3] G. W. Hooft, Comment on "Negative Refraction Makes a Perfect Lens". *Phys. Rev. Lett.* 87.24: 249701, (2001).
- [4] J. M. Williams. "Some problems with negative refraction." *Phys. Rev. Lett.* 87.physics/0105034: 249703, (2001).
- [5] J. B. Pendry. Comment on "Negative refraction makes a perfect lens" Reply. *Phys. Rev. Lett.*, 8724(24),( 2001).
- [6] P. M. Valanju, R. M. Walser, and A. P. Valanju. "Wave refraction in negative-index media: always positive and very inhomogeneous." *Phys. Rev. Lett.* 88.18: 187401 (2002).
- [7] J. B. Pendry, and D. R. Smith. "Comment on" Wave refraction in negative-index media: Always positive and very inhomogeneous"." *arXiv preprint cond-mat/0206563* (2002).
- [8] P.M. Valanju, R.M. Walser, and A.P. Valanju. Comment on "wave refraction in negative-index media: Always positive and very inhomogeneous" Reply. *Phys. Rev. Lett.*, (2003).
- [9] S. Foteinopoulou, E. N. Economou, and C. M. Soukoulis." Refraction in media with a negative refractive index. "*Phys. Rev. Lett.* 107402, (2003).
- [10] P. Kolinko and D. R. Smith."Numerical study of electromagnetic waves interacting with negative index materials." *Opt. Express*, :640–648,( 2003).
- [11] N. Garcia and M. Nieto-Vesperinas." Left-handed materials do not make a perfect lens." *Phys. Rev. Lett.*, :207403, (2002).
- [12] R. A. Shelby, D. R. Smith, and S. Schultz. "Experimental verification of a negative index of refraction." *Science*, 292(5514):77–79, (2001).
- [13] N. Garcia and M. Nieto-Vesperinas. "Is there an experimental verification of a negative index of refraction yet?" *Opt. Lett.*, 27(11):885–887,(2002).

- [14] A. N. Lagarkov, and A. K. Sarychev. "Electromagnetic properties of composites containing elongated conducting inclusions." *Phys. Rev. B* 53.10 (1996).
- [15] V. A. Podolskiy, A. K. Sarychev, V. M. Shalaev" Plasmon Modes in nano wires and Left-Handed Materials." *J. Nonlinear Opt Phys* 11:65-74.
- [16] A.V. Kildishev, "Negative refractive index in optics of metal-dielectric composites." *JOSA B* 23.3 : 423-433(2006).
- [17] J. Valentine. "Three-dimensional optical metamaterial with a negative refractive index." *nature* 455.7211: 376-379, (2008).
- [18] V. A. Podolskiy, A. K. Sarychev, and V. M. Shalaev. "Plasmon modes in metal nanowires and left-handed materials." *J. of Nonlinear Opt. Phys. & Mat.* 11.01 (2002).
- [19] G. Shvets, "Metamaterials add an extra dimension." *Nature Mat* 7.7 (2008).
- [20] N. Liu, "Stereometamaterials." *Nat. Photonics* 3.3 : 157-162 (2009).
- [21] R. S. Hegde, et al. "Shedding new light on super-resolution imaging: a spectral domain approach." *Fourth International Congress on Advanced Electromagnetic Materials in Microwaves and Optics*,( 2010).
- [22] Z. Szabó, Y. Kiasat and E.P. Li," Composite materials for subwavelength imaging," *MRS conference, Spring meeting*,(2011).
- [23] Z. Liu, and X. Zhang "Rapid growth of evanescent wave by a silver superlens." *App. phys. Let.* 83.25: 5184-5186 (2003).
- [24] N. Fang, and X. Zhang "Sub-diffraction-limited optical imaging with a silver superlens." *Science* 308.5721: 534-537, (2005).
- [25] B. Wood , J. B. Pendry, and D. P. Tsai. "Directed subwavelength imaging using a layered metal-dielectric system." *Phys. Rev. B* 74.11: 115116. (2006)
- [26] S. A. Ramakrishna , "Imaging the near field." *J. of Modern Opt.* 50.9 (2003).

## **CHAPTER 2**

# **THE VALIDATION OF MAXWELL-GARNETT EFFECTIVE MEDIUM THEORY**

### **2.1 Introduction**

The Maxwell-Garnett (MG) effective medium theory claims to assign a quantitative estimation for a macroscopic property, to a particular sample of heterogeneous material. This chapter is dedicated to determine the geometrical specifications i.e. the size of nanoparticles, the filling fraction of the inclusions in the composite, and the probability distribution function (PDF) of nanoparticles, that a heterogeneous material can be homogenized with classical MG theory accurately.

### **2.2 Assumptions of Effective Medium Model**

In the MG theory the optical properties of collection of nanoparticles are mainly determined by two contributions: the properties of the particles as well-isolated individuals and the collective properties of whole ensemble [1]. However, only in the case of well-separated particles in optically thin samples, the response of an N-particle system is equal to N-fold of the individual. Consequently, the

following conditions are required in order to be restricted to a simplified model system which the effective optical property can be predicted by MG theory accurately.

- The particle sizes are strictly limited to the quasistatic regime so that the scattering of light by particles become ineffective.
- The shape of particle can be approximated by spherical or nonspherical i.e. spheroidal, shapes with closed form solution when the particle is illuminated by light.
- Easily treatable geometries of the nano-scale assemblies can be selected.
- The predicted optical property remains in general bonds regardless of the geometry of the mixture and statistical distribution of each inclusion

### **2.3 The Size of the Nanoparticles**

For any individual particle, the size parameter ( $\gamma = \frac{2\pi r}{\lambda}$ ) should obey the Rayleigh limit thus, the scattering of light by the particles becomes ineffective. It is not straightforward to decide when this condition is satisfied, because the quantity, which has to be compared with the particles radius ( $r$ ), is the guided wavelength in the composite ( $\lambda$ ), which depends on the effective refractive index. However, it is possible to avoid the particle's scattering, if an upper bound is set to the maximum size of the nanoparticle. In order to investigate the effect of particle's scattering the high frequency effective medium model of spherical inclusions is introduced by Rupin in [2], which takes into account the scattering between the particles based on the Mie theory [3]. The scattering coefficients of the Mie

expansion in case of standalone spherical particle, when the magnetic permeability of the particle and of the surrounding medium is the same, can be expressed as,

$$a_n = \frac{m\psi'_n(x)\psi_l(mx) - \psi'_n(mx)\psi_l(x)}{m\xi'_n(x)\psi_n(mx) - \psi'_n(mx)\xi_n(x)} \quad (2.1)$$

$$b_n = \frac{\psi'_n(x)\psi_l(mx) - m\psi'_n(mx)\psi_l(x)}{\xi'_n(x)\psi_n(mx) - m\psi'_n(mx)\xi_n(x)} \quad (2.2)$$

$$m = \frac{n_i}{n_h} = \frac{\sqrt{\epsilon_i\mu_i}}{\sqrt{\epsilon_h\mu_h}}, \quad x = \sqrt{\epsilon_h\mu_h} \omega r / c_0, \quad (2.3.a)$$

$$\psi_n(x) = \sqrt{\frac{\pi x}{2}} j_{n+\frac{1}{2}}(x) \quad , \quad \xi_n(x) = \sqrt{\frac{\pi x}{2}} h_{n+\frac{1}{2}}^1(x) \quad (2.3.b)$$

where  $\Psi$  and  $\xi$  are the Riccati-Bessel and Riccati-Hankle functions respectively, the difference of Riccati-Bessel and Riccati-Hankle functions Bessel and Hankle functions is shown in equation (2.3.b). The coefficient  $m$  is the ratio of the inclusion and host refractive index,  $\epsilon_i$ ,  $\mu_i$ ,  $\epsilon_h$ , and  $\mu_h$  are the relative electric permittivity and magnetic permeability of the inclusion and host respectively,  $x$  is the size parameter in the host medium,  $\omega$  is the angular frequency of the incident light,  $r$  is the radius of the sphere and  $c_0$  is the speed of light in vacuum. The electric and magnetic dipole polarizabilities can be expressed with the first terms of the scattering coefficients as [2],

$$\alpha_e = i \frac{3r^3}{2x^3} a_1, \quad \alpha_m = i \frac{3r^3}{2x^3} b_1. \quad (2.4)$$

For standalone spheres these polarizabilities are exact for any size of the sphere and for any wavelength of the incident light. A high frequency extension



of the MG theory can be derived by introducing the polarizabilities (2.4) in the Clausius-Mossotti formula,

$$\frac{\varepsilon_{eff} - \varepsilon_h}{\varepsilon_{eff} + 2\varepsilon_h} = \frac{f}{r^3} \alpha_e. \quad (2.5)$$

Equation (2.5) leads to the following relation for the effective permittivity,

$$\varepsilon_{eff} = \frac{x^3 + 3ifa_1}{x^3 - 3/2ifa_1} \varepsilon_h. \quad (2.6)$$

The power series expansion of Riccati-Bessel functions and their derivatives for  $n=1$  and  $x \ll 1$ , Raleigh limit, can be simply expressed,

$$\psi_1(x) = \frac{x^2}{3} - \frac{x^4}{30}, \quad (2.7)$$

$$\psi'_1(x) = \frac{2x}{3} - \frac{2x^3}{15}, \quad (2.8)$$

$$\xi_1(x) = -\frac{i}{x} - \frac{ix}{2} + \frac{x^2}{3}, \quad (2.9)$$

$$\xi'_1(x) = \frac{i}{x^2} - \frac{i}{2} + \frac{2x}{3}. \quad (2.10)$$

The first electric and magnetic scattering coefficients then, can be expanded by above power series [3],

$$a_1 = -i \frac{2x^3}{3} \frac{m^2 - 1}{m^2 + 2} - \frac{i2x^5}{5} \frac{(m^2 - 2)(m^2 - 1)}{(m^2 + 2)^2} + \frac{4x^4}{9} \left( \frac{m^2 - 1}{m^2 + 2} \right)^2 + O(x^7), \quad (2.11)$$

$$b_1 = -\frac{ix^5}{45} (m^2 - 1) + O(x^7). \quad (2.12)$$

For quasi static limit which  $x \ll 1$ , the term  $x^3 \gg x^5$ , then  $a_1 \gg b_1$  and  $a_1$  is approximated by its first term,

$$\alpha_1 = -i \frac{2x^3 m^2 - 1}{3 m^2 + 2}. \quad (2.13)$$

Replacing equation (2.13) in equation (2.4) the electric polarizability is,

$$\alpha_e = \frac{m^2 - 1}{m^2 + 2}, \quad (2.14)$$

which is the well known Clausius-Mossotti relation and the effective permittivity of equation (2.6) should be the effective dielectric function derived by classical MG effective medium theory. For nanoparticles with  $2r > 50$  nm, the higher order multipole modes also contribute and the resonance's peak and width are affected also by quadropole and octopole absorption as well as scattering. As the size of nanoparticle increases, the higher harmonics become prominent as the light can no longer polarize the nano particle homogenously.

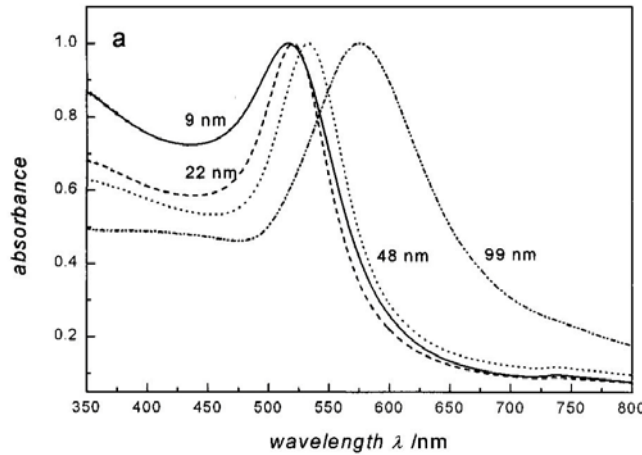


**Figure 2.1.** UV-visible absorption spectra of 9, 22, 48, and 99 nm gold nano particles in water. Reprinted with permission of [9].

The larger the particles become, the more the resonance peak is red shifted and broadened. This phenomena is investigated intensively both experimentally

[4-6] and theoretically [7, 8]. Figure 2.1(a) presents the red shift in the absorption peak of colloidal gold nano particles as the size of nanoparticles increases [9].

For the dipole approximation, there is no size dependence however experimentally a strong size dependence of the Plasmon bandwidth is observed [10]. To modify Mie theory for small particles, the dielectric function of nanoparticles itself is assumed to be size dependence due to the intrinsic size effect [10]. At optical frequencies, the electric permittivity of silver is determined not only by the motion of the free electrons in the lattice of metallic atoms; however the contribution of the bound electron vibration is also substantial. When the size of the metallic components is smaller than the mean free path of the conduction electrons ( $\approx 50$  nm), the bulk electric permittivity of metals has to be modified to take into account the scattering of the conduction electrons from the particle boundary, which leads to an additional loss mechanism [10]. The electric permittivity can be decomposed as,

$$\varepsilon_r = \varepsilon_r^f + \varepsilon_r^b, \quad (2.15)$$

where  $\varepsilon_r$  is the measured electric permittivity,  $\varepsilon_r^f$  is the free electron and  $\varepsilon_r^b$  is the bounded electron contribution. The contribution of the free electrons to the electric permittivity is modeled with the Drude model,

$$\varepsilon_r^f = 1 - \frac{\omega_p^2}{\omega^2 + i\gamma_e\omega}. \quad (2.16)$$

In this relation the plasma frequency  $\omega_p$  and the damping constant  $\gamma_e$  are determined from the measured bulk electric permittivity at a sufficiently low frequency, where the free electron motion is the major factor, which determines

the electromagnetic properties. In figure 2.2 the real and imaginary part of the measured bulk electric permittivity and its decomposition into components, which depends on free and bounded electron contributions, is shown. The size reduction effect on the electric permittivity is taken into account by modifying the damping constant in the Drude model [10],

$$\gamma_e = \gamma_e^{bulk} + \frac{v_f}{L_{eff}}. \quad (2.17)$$

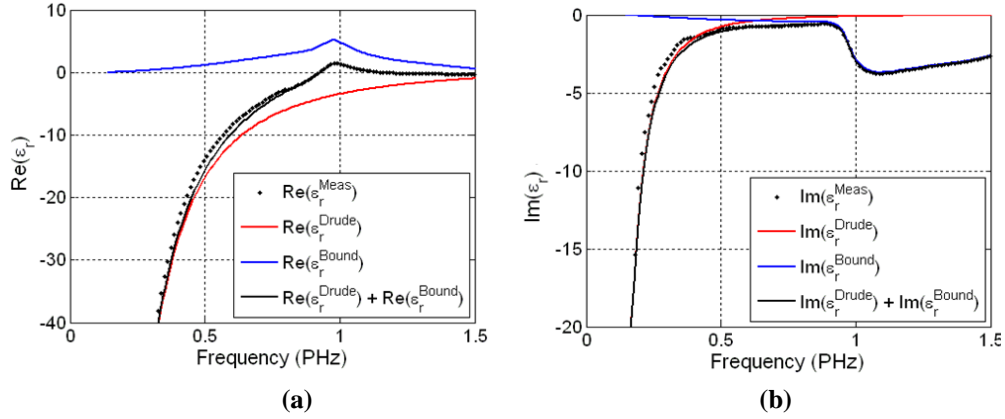


**Figure 2.2.** Decomposition of the electric permittivity of silver into free and bound electron contributions. In (a) the real part, while in (b) the imaginary part of the electric permittivity is shown.

here  $\gamma_e^{bulk}$  is the bulk value of the damping constant,  $v_f = 1.4 \cdot 10^6$  m/s is the Fermi velocity of electron in silver, and  $L_{eff}$  is the effective mean free path to take into account the effect of collisions with the boundary of the nanoparticle. For particles with arbitrary shape the effective mean-free path can be expressed with the billiard or Lambertian scattering model as  $L_{eff} = 4V/S$ , where  $V$  is the volume and  $S$  is the surface area of the nanoparticle [11]. Figure 2.3 presents the contribution of intrinsic size effect to the real part and imaginary part of dielectric function of nanoparticles with various radii.

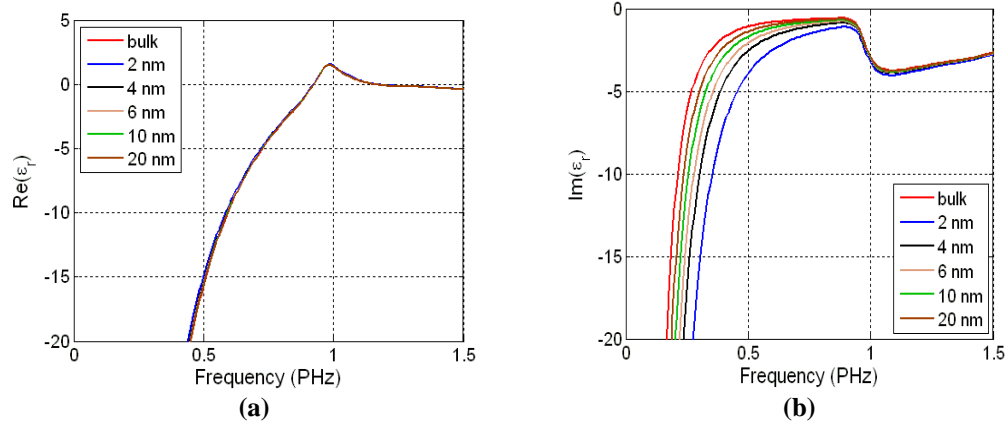


**Figure 2.3.** Dielectric function for nanoparticles with different radius (a) Real part (b) Imaginary part.

As it is presented in figure 2.3, while the real part of dielectric function is almost the same for nanoparticles with different radii, the imaginary part differs noticeably. Consequently one should expect that the width of the plasmon resonance peak is more affected than the place of the resonance. Figure 2.4 demonstrates the effective permittivity for metal-dielectric composites which is approximated with MG theory while the intrinsic size effect for small particles is taken into account. The filling fractions for all samples are 0.5 and the inclusions for each composite have the same size. As it is expected the widths of resonances are more affected than the location of resonances by the intrinsic size effect.

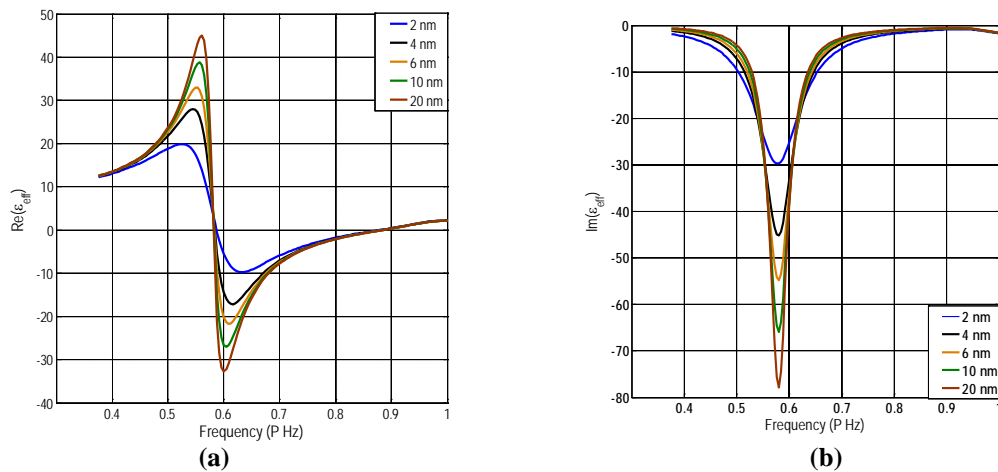


**Figure 2.4.** The effective permittivity of metal dielectric composites made of silver nanospheres with different radius (a) Real part (b) Imaginary part

Within the dipole approximation, by increment in the radius of nanoparticle, the resonance peak is slightly blue shifted and the width of the resonance is noticeably narrowed. In addition to intrinsic size effect, for nanoparticles smaller than 2 nm the quantum effect should be taken into account as well [12]. Consequently to avoid the quantum effects the lower bound for nanoparticles is set to  $r_{min} = 2 \text{ nm}$ . In order to satisfy the Raleigh limit, which makes the scattered field by the nanoparticles ineffective, an upper bound should be determined for the maximum radius that a nanoparticle can take. The effect of size of nanoparticle on the scattering coefficients of different excited harmonics is studied in figure2.5. Figure 2.5 demonstrates the scattering coefficients ( $a_1$ - $a_6$ ) which are normalized to  $a_1$  for a silver nanoparticle embedded in SiO2 host.

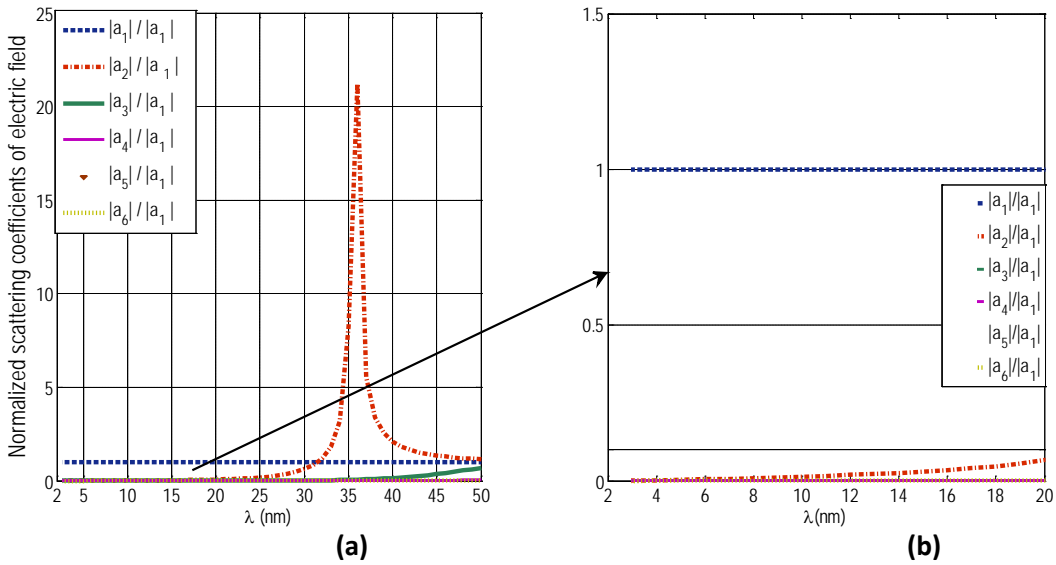


**Figure 2.5** normalized scattering coefficients for different sizes of silver nanoparticle embedded in SiO2 (a) the contribution of higher order modes for nano particles (b) the particle radius that the second harmonic contribution becomes prominent.

The working frequency is chosen to be in UV range ( $\lambda = 248 \text{ nm}$ ) where the wavelength is more sensitive to the particle size. The radius of the

particle is varied from  $2nm$  to  $50 nm$  and the intrinsic size correction is considered for the dielectric function of silver nano particles. As it is shown in figure 2.5 (b), the second harmonic which represents the dynamic dipole starts to grow for nano particle with radius  $r = 10 nm$  and becomes prominent for  $r = 20 nm$  onward. Consequently the upper limit is set  $r_{max} = 10 nm$  to assure the quasi static limit.

## 2.4 Geometry of Nanoparticles Assembly

Maxwell-Garnett theory was generally derived by considering the dipolar character for scatterers and neglecting the particles' spatial distribution in the host medium. The assumption in homogenization is that the effective medium has the same behavior when illuminated by electromagnetic wave, as the heterogeneous mixture does. Consequently forward-scattering and backward-scattering amplitudes of a cell of composite medium immersed inside the effective homogenous background, figure 2.6, should be zero [13-16]. In figure 2.6 the white dotted line represents the boundary of the sample under calculation; the forward and backward scattering is calculated for this sample,

$$\sum_i S_i(\theta = 0) = \sum S_i(\theta = \pi) = 0, \quad (2.18)$$

where  $i$  represents harmonics of scattered field. A rigorous proof of (2.18) has been given by Stroud and Pan [14] from Mie theory, and the forward-scattering and backward-scattering amplitudes are given by,

$$\sum_i S_i(\theta = 0) = \frac{1}{2} \sum_{n=1}^{\infty} (2n+1)(a_n + b_n), \quad (2.19)$$

$$\sum_i S_i(\theta = \pi) = \frac{1}{2} \sum_{n=1}^{\infty} (2n+1)((-1)^{n+1}a_n + (-1)^n b_n). \quad (2.20)$$

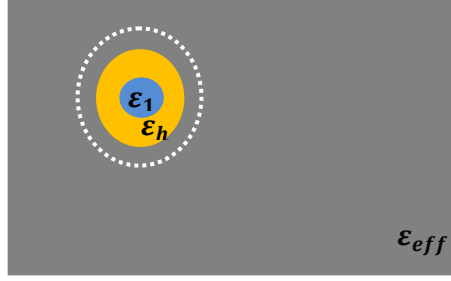


**Figure 2.6** A cell of composite medium immersed inside the effective homogenous background.

As it is discussed in previous sections for nanoparticles with size much smaller than the wavelength, the first harmonic is the dominating term; hence equations (2.19) and (2.20) are simplified to,

$$\sum_i S_i (\theta = 0) = \frac{3}{2}(a_1 + b_1), \quad (2.21)$$

$$\sum_i S_i (\theta = \pi) = \frac{3}{2}(a_1 - b_1). \quad (2.22)$$

This technique is sometimes called scattering matrix method. The scattering coefficients for a spherical core-mantle grain shown in figure 2.6, is written as,

$$a_1 = \frac{2i (\varepsilon_h - \varepsilon_{eff})(\varepsilon_1 + 2\varepsilon_h) + f(\varepsilon_{eff} + 2\varepsilon_h)(\varepsilon_1 - \varepsilon_h)}{3 (\varepsilon_h + 2\varepsilon_{eff})(\varepsilon_1 + 2\varepsilon_h) + 2f(\varepsilon_h - \varepsilon_{eff})(\varepsilon_1 - \varepsilon_h)} x^3, \quad b_1 = 0, \quad (2.23)$$

where  $x$  is the size parameter introduced in equation (2.1),  $\varepsilon_{eff}$ ,  $\varepsilon_1$  and  $\varepsilon_h$  are the effective permittivity, the permittivity of the inclusion and host respectively and  $f$  is the filling fraction of the inclusion. The magnetic scattering coefficient  $b_1$  is 0 based on the assumption that the effective optical property of the mixture remains nonmagnetic,  $\mu_{eff} = 1$ . The expression for effective permittivity of the medium is derived by replacing equation (2.23) in equation (2.21) or (2.22)



$$\varepsilon_{eff} = \varepsilon_h \frac{1+2f \frac{\varepsilon_1 - \varepsilon_h}{\varepsilon_1 + 2\varepsilon_h}}{1-f \frac{\varepsilon_1 - \varepsilon_h}{\varepsilon_1 + 2\varepsilon_h}}. \quad (2.24)$$

Equation (2.24) is the exactly effective permittivity, derived by classical MG theory. More sophisticated models based on multiple scattering have been proposed [18, 19]; for most of these expressions, the MG is found to be the limiting case as the size parameter  $x$  tends to zero, which is the long wavelength limit.

The main limitation of MG theory is that it does not discriminate between two random mediums with the same density of scatterers. Neglecting N-particle distribution functions is justified in the single scattering regime, when mean field inside the material only depends on the particle density. This is the reason why it is often claimed that a weak particle interaction is a condition for the validity of MG theory [20]. In addition, the accuracy of MG theory is suspected for high concentration of scatterers. However Mallet *et al.* [20] point out a rigorous derivation of MG expression that accounts for the density fluctuation of the particles and for the presence of multiple scattering. Their mathematical approach is quite similar to Draine *et al.*[21]; in [21] Draine *et al.* applied discrete dipole approximation (DDA) technique to find the best prescription for the dipole polarization in a polarizable lattice such that, the lattice mimics a continuum with effective permittivity  $\varepsilon(\omega)$ . Mallet *et al.* [20] analytically explained that if the single scattering is the dominant mechanism, the effective permittivity predicted by MG theory is quite accurate regardless of the statistical distribution of the particles, as long as the distribution is uniform. On the other hand, if multiple

scattering is important, the effective permittivity depends strongly on the n-point PDF of the aggregate. Yet, if the particle positions can be considered uncorrelated, the effective permittivity reduces to the MG expression.

Consequently, even for high concentration of nano particles ( $f = 52\%$  for the full lattice), the MG theory predicts accurate effective permittivity for the metal-dielectric system investigated in this dissertation. As it is shown in the previous section, an upper bound is set for the nanoparticles' radius to remain in the quasistatic working frame and the only additional condition needed to be satisfied is the uniform distribution of the particles in the host medium. In case the particles' sizes are different the radius of the largest particle should not exceed the upper limit.

## 2.5 General Bounds for Effective Medium Theory

As finding an exact solution for the field behavior in a complex medium such as a metal-dielectric composite is impossible, it is beneficial to at least set some bounds, consistent with the physical nature of the problem, for the approximated effective optical property. Consider a two phase mixture where permittivities of the phases are  $\varepsilon_i$  and  $\varepsilon_e$ . Searching for absolutely loosest bound, in other words, bounds that cannot be exceeded regardless of which volume fraction and geometries the particles take, intuitively it can be said that the permittivity of the mixture has to fall in between two component's permittivities [22]:

$$\min(\varepsilon_i, \varepsilon_e) < \varepsilon_{eff} < \max(\varepsilon_i, \varepsilon_e). \quad (2.25)$$

A good analogy is to consider the conductivity of a mixture of a conductor and a resistor. If a good conductor is mixed with a material that has smaller conductivity, a better conduction is not expected eventually. However, a stricter bound can be written for the effective permittivity of the final mixture. This bound can be found by considering how conductivity or permittivity can be decreased or increased effectively. The increment in the conductivity is made by creating “easy path” to the current flow or flux; which means that the boundary between the inclusion and host should be parallel to the flow. Likewise, in order to minimize the current flow, the flow should be blocked as effectively as possible by locating the boundaries perpendicular to it,

$$\varepsilon_{eff,max} = f\varepsilon_i + (1 - f)\varepsilon_e, \quad (2.26)$$

$$\varepsilon_{eff,min} = \frac{\varepsilon_i\varepsilon_e}{f\varepsilon_e + (1-f)\varepsilon_i}. \quad (2.27)$$

Here  $f$  is the filling fraction of material with permittivity of  $\varepsilon_i$ . The two bounds in equation (2.26) and (2.27) are called Wiener bounds. The Wiener bounds can also be extended to complex value of permittivities [23, 24]. The mixtures corresponding to Wiener bounds are anisotropic. If the mixtures are isotropic stricter bound can be proposed. The analysis by Hashin and Shtrikman [25] establishes variation theorems which are then used to derive limits for the magnetic permeability of a mixture. By the duality between electrostatic and magneto-static problems, the results are equally valid for the effective permittivity of a mixture,

$$\varepsilon_{eff,max} = \varepsilon_e + 3f\varepsilon_e \frac{\varepsilon_i - \varepsilon_e}{\varepsilon_i + 2\varepsilon_e - f(\varepsilon_i - \varepsilon_e)}, \quad (2.28)$$

$$\varepsilon_{eff,min} = \varepsilon_i + 3(1 - f)\varepsilon_i \frac{\varepsilon_e - \varepsilon_i}{\varepsilon_e + 2\varepsilon_i - (1-f)(\varepsilon_e - \varepsilon_i)}. \quad (2.29)$$

This bound is developed based on the electrostatic energy within the material. This function is volume integral of the field and polarization density. Depending on which of the components is dielectrically denser the values of this function gives the upper and lower limit. Although remaining inside the bounds introduced by equations (2.26) – (2.29) does not verify the validity of any effective medium theory, exceeding these bounds can disqualify the effective property predicted by an effective medium theory.

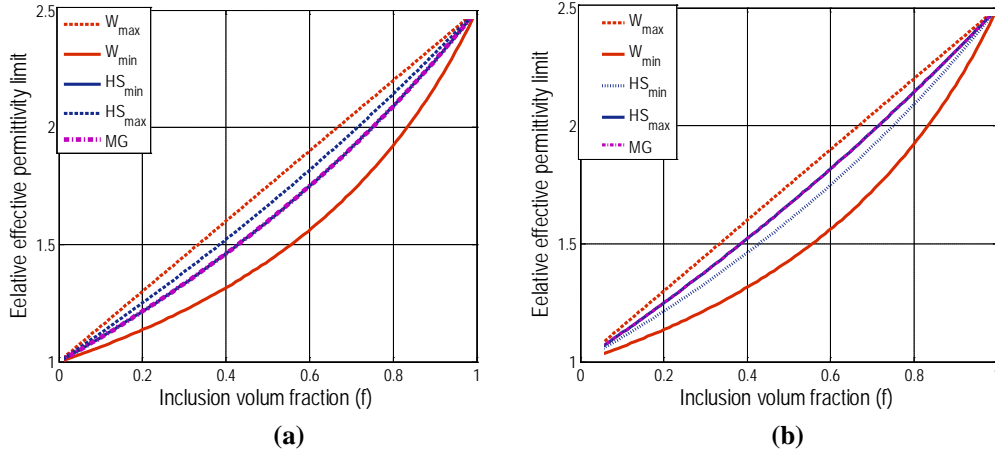


**Figure 2.7** Wiener bounds (W) and Hashin-Shtrikman (HS) bounds and MG theory for the effective permittivity of a mixture with  $\varepsilon_i = 2.5$  and  $\varepsilon_e = 1$  (a) The spherical inclusions  $\varepsilon_i$  in the environment  $\varepsilon_e$  (b) The spherical inclusions  $\varepsilon_e$  in the environment  $\varepsilon_i$

Figure 2.7 presents the Wiener bounds and Hashin-Shtrikman bounds for a mixture of  $\varepsilon_i = 2.5$  and  $\varepsilon_e = 1$ , and the effective permittivity of the same mixture approximated with MG theory. It can be seen that the Hashin-Shtrikman (HS) bounds are equal to MG mixing rules for isotropic spherical inclusions; the MG for spherical inclusions  $\varepsilon_i$  in the environment  $\varepsilon_e$  is equal to the lower HS bound

and the MG for spherical inclusions  $\varepsilon_e$  in the environment  $\varepsilon_i$  is equal to the higher HS bound. In addition according to the figure 2.7 it is evident that HS bounds are quite stricter bounds than Wiener bounds. The Hashin-Shtrikman effective medium model is developed based on calculating the strain energy stored in the material when subjected to gross uniform strains or stresses. In order to evaluate this strain energy it is necessary to find the stress or displacement fields in the composite body, which appears to be an impossible task. Consequently, attempts to find expressions for effective elastic moduli, or other physical constants, have invariably been based on simplifying assumptions, concerning geometrical form and physical behavior of phase regions. A simplifying approach is to use variational principles in order to bound the strain energy and thus also the effective elastic moduli regions. In Hashin-Shtrikman model the strain energy is bounded by minimum complementary energy principle which reveals why the model is more restrict in comparison to the other models.

## **2.6 Conclusion**

In this chapter, appropriate geometrical specifications are allocated to the size, filling fraction, and probability distribution function (PDF) of metallic inclusions to suggest a well-defined structure for the metal-dielectric composite, which its effective optical property can be approximated by MG theory accurately. The effect of the size of nanoparticle is studied through Mie scattering theory; it is shown that the high frequency extension of MG, Mie Maxwell-Garnett (MGG), is reduced to the classical MG in the quasi static work frame. The dielectric function of silver nanoparticles with radius smaller than silver's mean free path length is corrected in order to take into account the intrinsic size effect. It is

shown that while the position of resonance peak of effective permittivity is not affected by the intrinsic size effect, the width of the resonance is decreased as the radius increases. In order to avoid the quantum effect and inter-particle mutual interaction the lower bound ( $r_{min} = 2 \text{ nm}$ ) and upper bound ( $r_{max} = 10 \text{ nm}$ ) are set for the radius of the nanoparticles. In addition it is shown by scattering matrix method that as long as the inclusions are not overlapping and their radius size is restricted in long wavelength regime the effective permittivity is reduced to the expression derived by MG theory. This investigation provides estimation for the maximum filling fraction that MG theory is still accurate. It is concluded that if the single scattering is the dominant mechanism, the effective permittivity predicted by MG theory is quite accurate regardless of the statistical distribution of the particles, as long as the distribution is uniform. Consequently for the uniform distribution of silver nanoparticles in the dielectric host the filling fraction for accurate result can be up to 52% which is the filling fraction for the full lattice.

## Reference

- [1] S. K. Ghosh, and P. Tarasankar. "Interparticle coupling effect on the surface plasmon resonance of gold nanoparticles: from theory to applications." *Chem. Rev.* 107.11: 4797-4862, (2007).
- [2] R. Ruppin, "Evaluation of extended Maxwell-Garnett theories." *Optics communications* 182.4 : 273-279, (2000).
- [3] C. F. Bohren, and D. R. Huffman. "Absorption and scattering of light by small particles". *Wiley*. (2008).
- [4] E. A. Coronado, G. C. Schatz. "Surface plasmon broadening for arbitrary shape nanoparticles: A geometrical probability approach", *J. of chem. Phys.*, Volume 119, August (2003).
- [5] J. J. Mock, M. Barbic, D.R. Smith, D. A. Schultz, and S. Schultz. "Shape effects in plasmon resonance of individual colloidal silver nanoparticles." *J. of Chem. Phys.*:6755–6759, (2002).
- [6] S. Link, C. Burda, B. Nikoobakht, and M. A. El-Sayed. "How long does it take to melt a gold nanorod? A femtosecond pump-probe absorption spectroscopic study." *Chem. Phys. Lett.*, 12–18, 1999.
- [7] H. L. Kwok. "Electronic materials." *Boston: PWS Publishing Company*, (1997).
- [8] B. Palant. "Optical properties of gold clusters in the size range 2–4 nm." *Phys. Rev. B* 57.3, (1998).
- [9] S. Link, and M. A. El-Sayed. "Size and temperature dependence of the plasmon absorption of colloidal gold nanoparticles." *J. of Phys. Chem. B*, 103.21: 4212-4217, (1999).
- [10] Kreibig, Uwe, and Michael Vollmer. "Optical properties of metal clusters." (1995).
- [11] K. L. Kelly, "The optical properties of metal nanoparticles: the influence of size, shape, and dielectric environment." *J. of Phys. Chem. B*, 107.3,: 668-677 (2003).
- [12] E. D. Palik. "Handbook of Optical Constants of Solids" *Access Online Elsevier*, Vol. 3, (1998).

- [13] N. Alexander, and C. W. Bates. "Optical properties of inhomogeneous composite materials." *Solid state communications* 51.5 :331-333, (1984).
- [14] D. Stroud, and F. P. Pan. "Self-consistent approach to electromagnetic wave propagation in composite media: Application to model granular metals." *Phys. rev. B* 17.4 :1602, (1978).
- [15] C. G. Granqvist. "Radiative heating and cooling with spectrally selective surfaces." *Applied Optics* 20.15 :2606-2615. (1981).
- [16] P. Chýlek, and V. Srivastava. "Dielectric constant of a composite inhomogeneous medium." *Phys. Rev. B* 27.8 (1983).
- [17] M. Lax, *Phys. Rev.* 85, 621 (1952).
- [18] L. Tsang, J. A. Kong, and T. Habashy. "Multiple scattering of acoustic waves by random distribution of discrete spherical scatterers with the quasicrystalline and Percus–Yevick approximation." *J. Acoust. Soc. Am* 71 (1982): 552.
- [19] V. A. Davis , and L. Schwartz. "Electromagnetic propagation in close-packed disordered suspensions." *Phys. Rev.B* 31.8 (1985).
- [20] P. Mallet, C. A. Guérin., and A. Sentenac. "Maxwell-Garnett mixing rule in the presence of multiple scattering: Derivation and accuracy." *Phys Rev B* 72.1: 014205, (2005).
- [21] B. T. Draine, and J. Goodman. "Beyond Clausius-Mossotti-Wave propagation on a polarizable point lattice and the discrete dipole approximation." *ApJ*, 405: 685-697 (1993).
- [22] A. H. Sihvola." Electromagnetic mixing formulae and applications. " *Iet*, (1999).
- [23] V. D. Bruggeman, "Berechnung verschiedener physikalischer Konstanten von heterogenen Substanzen. I. Dielektrizitätskonstanten und Leitfähigkeiten der Mischkörper aus isotropen Substanzen." *Ann.n der Phy.k* 416.7 : 636-664 ,(1935).
- [24] G. Grimvall. "Thermophysical properties of materials." *Access Online via Elsevier*, (1999).
- [25] Z. Hashin, , and S. Shtrikman. "A variational approach to the theory of the elastic behavior of multiphase materials." *J. of the Mech. and Phys.* 11.2 : 127-140 ,(1963).



# CHAPTER 3

## TUNABLE SUBWAVELENGTH IMAGING WITH METAL-DIELECTRIC COMPOSITES

### 3.1 Effective Medium Theory

Maxwell-Garnett (MG) effective theory [1] and Bruggeman effective medium approximation [2] are two of the most widely used and well known effective medium approaches. Each of these two methods is based upon slightly different assumption regarding the composite topology and material properties of each constituent in mixture. Depending on the relative concentration of the inclusions and process of fabrication, metal-dielectric composite may have different macroscopic structure. Figure 3.1 demonstrates the macroscopic structure of (a) Maxwell-Garnett and (b) Bruggeman prototypes.



**Figure 3.1** Macroscopic structure of (a) Maxwell-Garnett (b) Bruggeman [5].

The effective permittivity in most of effective medium approximations is calculated based on the Clausius–Mossotti formula [3,4], also known as Lorentz-Lorenz equation. Lorentz pointed out that the local field experienced by molecule is not macroscopically averaged field  $E$  but instead  $E_L$ , which is called local field. Assuming an incident electric field of  $E$  is imposed to a material, the local field which is experienced by the molecule can be expressed as follow,

$$E_L = E + E_d + E_s + E_{near}. \quad (3.1)$$

As is shown in figure 3.2,  $E$  is the incident electric field,  $E_d$  is the depolarization field due to the polarization charges lying at the external surface of the medium. The relationship between  $E_d$  and the macroscopic polarization  $P$  is  $E_d = -P/\epsilon_0$ .  $E_s$  is the electric field on the spherical cavity, appropriately named Lorentz sphere, surrounding the molecule.

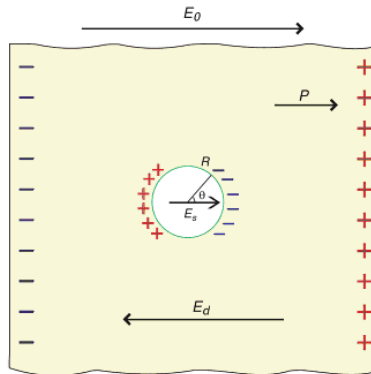


**Figure 3.2** Lorentz sphere concept for calculating local field [5].

The radius of the sphere  $R$  is macroscopically small in order to accommodate the discrete nature of the medium very close to the molecule while microscopically large enough, so that the matrix lying outside may be treated as continues medium.  $E_{near}$  is depending on the lattice structure of the medium and

how molecules are arranged in the media.  $E_{near}$  is zero owing to the symmetry of cubic lattice here. Consequently,

$$E_L = E + \frac{P}{3\epsilon_0}, \quad (3.2)$$

which is known as Lorentz relation: the field acting at an atom site in a cubic lattice is the macroscopic field  $E$  plus  $\frac{P}{3\epsilon_0}$  from polarization of other atoms in the system. If  $\alpha$  denote the polarizability of one molecule, then the polarization  $P$  is expressed as:

$$P = N\alpha E_L = N\alpha \left( E + \frac{P}{3\epsilon_0} \right). \quad (3.3)$$

Hence the relationship between the polarisability of a molecule in a material and the macroscopic permittivity of it can be written as:

$$\alpha = \frac{3\epsilon_0}{N} \frac{\epsilon - 1}{\epsilon + 2}, \quad (3.4)$$

which is called Clausius–Mossotti relation. Assume that a metal-dielectric composite is formed by embedding metallic spheres with relative permittivity of  $\epsilon_1$  in dielectric host with relative permittivity of  $\epsilon_h$ . The Clausius–Mossotti relation is applied to find the effective permittivity of the composite by the following order,

$$\frac{N\alpha}{3f\epsilon_0\epsilon_h} = \frac{\epsilon_{eff} - \epsilon_h}{\epsilon_{eff} + 2\epsilon_h}, \quad (3.5)$$

where for the metal-dielectric composite  $\alpha$  is written as:

$$\alpha = \frac{3\epsilon_0\epsilon_h}{N} \frac{\epsilon_1 - \epsilon_h}{\epsilon_1 + 2\epsilon_h}, \quad (3.6)$$

where ‘f’ is the feeling fraction of the metallic spheres. Substituting  $\alpha$  from (3.6) to equation (3.5) the effective permittivity of the composite,  $\epsilon_{eff}$ , is obtained as,

$$\epsilon_{eff} = \epsilon_h \frac{1+2f \frac{\epsilon_1 - \epsilon_h}{\epsilon_1 + 2\epsilon_h}}{1-f \frac{\epsilon_1 - \epsilon_h}{\epsilon_1 + 2\epsilon_h}}. \quad (3.7)$$

Equation (3.2) is known as the Maxwell-Garnett mixing rule. Figure 3.3 demonstrates the real part and the imaginary part of the effective permittivity for a silver-silica composite for different filling fraction of the metal in the optical range.

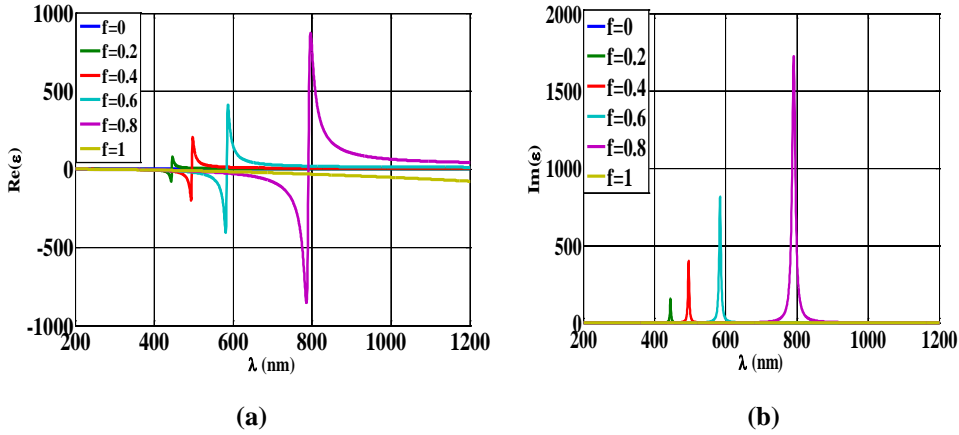


**Figure 3.3** the effective complex permittivity of silver nanoparticles embedded in silica host for different filling fractions of silver (a) Real part (b) Imaginary part

As it is shown the value of the  $\epsilon_{eff}$  is varying according to the filling fractions, operational wavelength and permittivity of the constituents, which makes the composites suitable to engineer tunable superlens. Figure 3.4 shows the range of operation wavelengths (UV-visible) that composite material can provide negative permittivity and lower amount of loss in comparison with silver simultaneously. Although the effective permittivity in MG can reach the permittivities of the two constituents when the filling fraction approaches the two extreme values of  $f = 0$  and  $f = 1$ , equation (3.7) shows that MG treats the inclusions in an unsymmetrical manner.

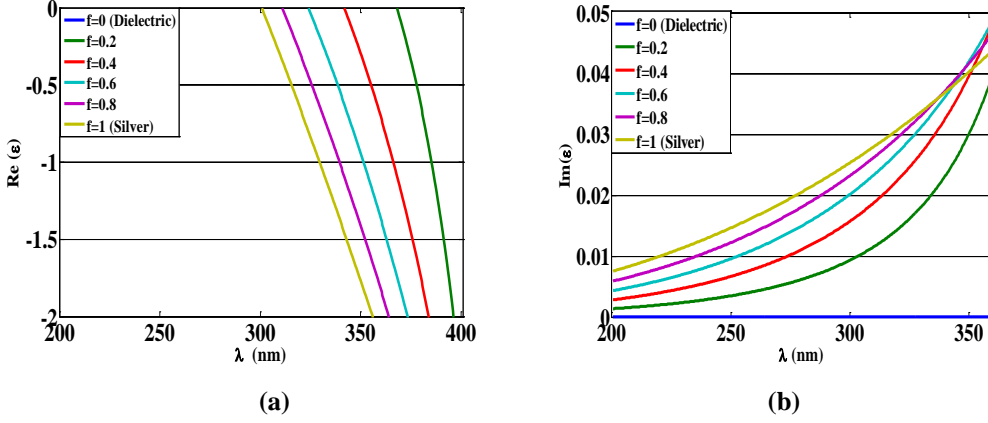


**Figure 3.4** Effective permittivity of silver silica composite approximated by MG theory (a) Negative permittivity for sub-wavelength in different wavelength is realized by composite super lens (b) the amount of composite's loss is smaller in comparison with bulk silver

Therefore, before evaluating the effective parameters of a two-phase or multi-phase composite using MG, one constituent has to be considered the “host” and the others “inclusion.” this asymmetry is particularly strong when the difference in the permittivities of the two materials is large. Using the Clausius–Mossotti relation and assuming that both phases of the composite (metal and dielectric) are embedded in the media with effective permittivity of  $\epsilon_{eff}$ , another expression for effective permittivity is derived which is known as Bruggeman mixing rule,

$$\epsilon_{eff} = \frac{1}{4} \{ (3f_1 - 1)\epsilon_1 + (3f_2 - 1)\epsilon_2 \mp \sqrt{[(3f_1 - 1)\epsilon_1 + (3f_2 - 1)\epsilon_2]^2 + 8\epsilon_1\epsilon_2} \}. \quad (3.8)$$

The sign in the equation above is chosen in a way that the imaginary part shows consistency with causality. Figure 3.5 shows the real part and imaginary part of the effective permittivity for a silver-silica composite for different filling fraction of the metal in the optical range.

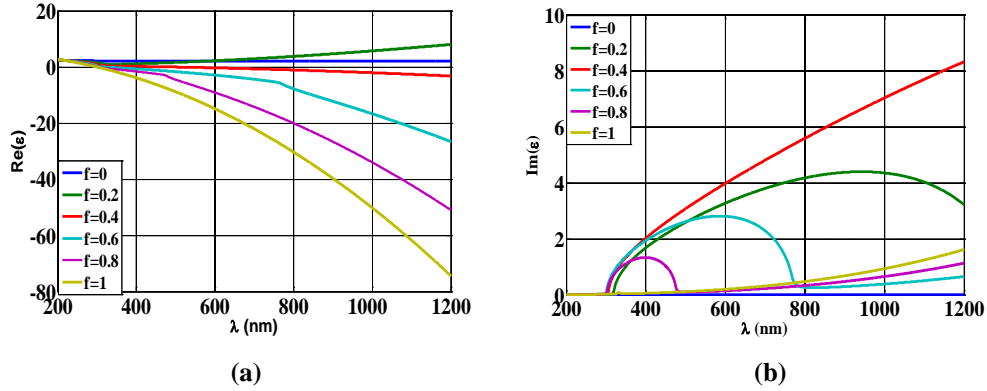


**Figure 3.5** Effective permittivity of silver silica composite approximated by Bruggeman theory  
(a) Real part (b) Imaginary part.

Unlike the MG, the two components here are symmetrical with respect to the exchange of roles of  $\epsilon_1$  and  $\epsilon_2$ . In other words in Bruggeman both phases are considered to be embedded in the effective medium, and there is no requirement to give preference to one phase over the other.

In order to have an accurate value for the effective parameters of a composite material, a suitable mixing rule according to the filling fractions and the arrangement of metallic nanoparticles in the dielectric host should be chosen. The composite is made of silver nanoparticles embedded in silica slab. An upper limit of 0.5 is set for filling fraction, to avoid percolation, consequently for nanoparticles with size much smaller than the wavelength the nanoparticles are not connected and their effect on the adjacent particles is via their far-field radiation. For the given configuration, the Maxwell-Garnett theory is applicable to approximate the effective permittivity of the metal dielectric composite. To evaluate the imaging performance of composite super lens, the refraction of light for a metal-dielectric composite slab is studied and its ability to transfer the transverse spatial harmonics, propagating and evanescent is investigated.

### 3.2 Optics of a Single Homogenous Isotropic Layer

The transmission and reflection of electromagnetic radiation at a thin dielectric layer between two semi-finite media is a well-known problem. The general solution for this problem starts from writing set of Maxwell equations for each media and imposing boundary conditions on each interface to find the transmission and reflection coefficients. If a TM polarized plane wave is an incident wave in the first media according to figure 3.6, the reflected and transmitted wave are TM polarized as well.

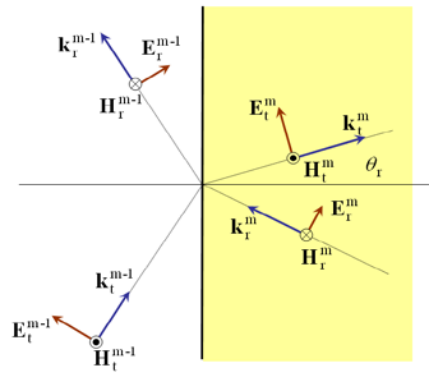


**Figure 3.6** Reflection and transmission of TM wave at the semi-finite isotropic-isotropic interface.

The plane of incidence is considered to be x-y plane. If the polarization of magnetic field (H-field) for the TM wave is in y direction, the electric field (E-field) polarization vector and propagation vector are lying in x-z plane. The configuration in figure 3.7 is formed if the second medium in figure 3.6 is bounded. The light interaction with such geometry involves the incidence and reflection of light in the first semi-finite medium, the transmission and reflection

of light in the bounded medium and the transmission of light into the second semi-finite medium, figure 3-7. The fields in three mediums can be written as follow,

$$H_y = \begin{cases} A \exp(-i\widehat{k}_1 \cdot \hat{r} + i\omega t) + B \exp(-i\widehat{k}'_1 \cdot \hat{r} + i\omega t) & z < 0 \\ C \exp(-i\widehat{k}_2 \cdot \hat{r} + i\omega t) + D \exp(-i\widehat{k}'_2 \cdot \hat{r} + i\omega t) & 0 < z < d \\ F \exp(-i\widehat{k}_3 \cdot \hat{r} + i\omega t) & z > d \end{cases} \quad (3.9)$$

where for each media,

$$\widehat{k}_i = k_{xi}\hat{x} + k_{zi}\hat{z}. \quad (3.10)$$

A, C, and F are coefficients for forward propagating waves, +z direction, B and D are reflected waves propagating backwards, -z direction, and d is the thickness of the slab, Figure 3.7.

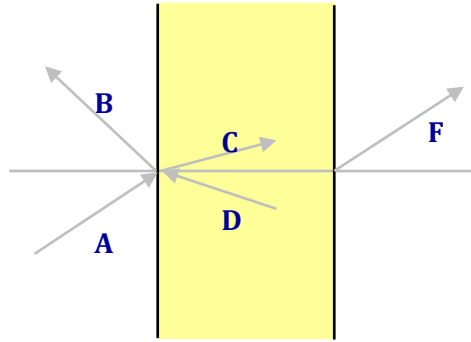


**Figure 3.7** Forward and backward propagating TM waves

Based on the wave equation, for an isotropic medium with  $\epsilon_i$  and  $\mu_i$ :

$$k_i^2 = k_{xi}^2 + k_{zi}^2 = \omega \sqrt{\epsilon_i \mu_i}. \quad (3.11)$$

Since  $k_x$  is reserved in interfaces,

$$k_{xi} = k_x \quad (3.12)$$



where  $k_x$  is the tangential component of the K vector of the incident wave which is known. The transfer function is found by the calculation of  $F/A$  ratio in figure 3.7. The electric field in each medium is,

$$E_x = \begin{cases} \frac{-k_{z1A}}{\varepsilon_1} \exp(-i\widehat{k}_1 \cdot \hat{r} + i\omega t) + \frac{k_{z1B}}{\varepsilon_1} \exp(-i\widehat{k}'_1 \cdot \hat{r} + i\omega t) & z < 0 \\ \frac{-k_{z2C}}{\varepsilon_2} \exp(-i\widehat{k}_2 \cdot \hat{r} + i\omega t) + \frac{k_{z2D}}{\varepsilon_2} \exp(-i\widehat{k}'_2 \cdot \hat{r} + i\omega t) & 0 < z < d \\ \frac{-k_{z3F}}{\varepsilon_3} \exp(-i\widehat{k}_3 \cdot \hat{r} + i\omega t) & z > d \end{cases} \quad (2.13)$$

The relation between the amplitude of the incident field, A, and the amplitude of the transmitted field in the exit medium, F is found by the continuity of the tangential components of E-field and H-field and the phase shift that the plane wave is experiencing while propagating in each medium,

$$\frac{F}{A} = T(k_x) = \frac{4\xi_1\xi_2}{(\xi_1 + 1)(\xi_2 + 1)e^{ik_{z2}d_2} + (\xi_1 - 1)(\xi_2 - 1)e^{-ik_{z2}d_2}} \quad , \quad (3.14)$$

$$\xi_1 = \frac{\varepsilon_{r2}k_{z1}}{\varepsilon_{r1}k_{z2}} \quad , \quad \xi_2 = \frac{\varepsilon_{r3}k_{z2}}{\varepsilon_{r2}k_{z3}} \quad . \quad (3.15)$$

$T(k_x)$  is the transfer function for the TM polarized wave. Here  $k_{z1}, k_{z2}, k_{z3}$  and  $\varepsilon_{r1}, \varepsilon_{r2}, \varepsilon_{r3}$  are the normal components of the wave vector and the complex relative permittivity of first, second and third medium respectively, Figure3.7. The expression for the TE polarized wave is the same as equation (3.14) while  $\varepsilon_i$  is replaced by  $\mu_i$ .

As it is presented in equation (3.14), the transfer function only depends on normal component of propagation vector and intrinsic property of the media. As the transfer function for TM polarized wave, is not a function of permeability, the

negative permittivity is sufficient for subwavelength imaging. In order to test the accuracy of derived expression for the transfer function, a silver slab is simulated with CST full-wave simulator and the result of the simulation, S21, is compared with analytic expression, (3.14). Figure 3.8 is the schematic of silver slab in CST and demonstrates the good agreement of analysis and simulation. The CST result is provided for limited number of k values (propagating) as there is no source in frequency domain analysis which can generate evanescent waves.

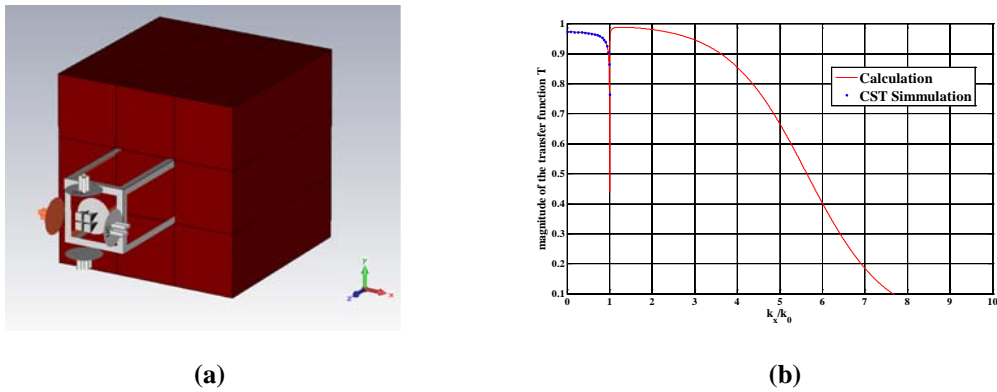


**Figure 3.8** Transfer function of silver slab CST simulation versus analytical calculation (a) Schematic of silver slab in CST (b) Agreement of analysis and simulation.

### 3.3 Tunable Composite Superlens

The advancement of metamaterial research led to the extension of the theory of transmission and reflection of single and multilayer isotropic thin films to single negative ( $\epsilon < 0, \mu > 0$ ) and double negative ( $\epsilon < 0, \mu < 0$ ) materials. The subwavelength feature of an object is considered by setting two Gaussian pulses 100 nm away in the object plane. The objective is to design a lens capable of carrying enough spatial harmonics such that that the two Gaussian peaks are

distinguishable in the image plane, figure 3.9. The Fourier transform of the electromagnetic field distribution  $g(x, y)$  of in the source plane is:

$$G(f_x, f_y) = \int g(x, y) e^{-i2\pi(f_x x + f_y y)} dx dy, \quad (3.16)$$

where  $k_x = 2\pi f_x$  and  $k_y = 2\pi f_y$  are the components of the wave vector in the longitudinal direction, satisfying the relation  $k_x^2 + k_y^2 + k_z^2 = (\omega/c_0)^2$ .  $k_z$  is the wave number in the transverse direction  $z$ ,  $\omega$  is the angular frequency and  $c$  is the speed of light in the medium which fills up the space in front of the lens. The algorithm in the present form is not taking any assumption how the source is generated, consequently there is no account for the interaction of the source and the metamaterial lens. The transfer function of the imaging system, in case of the double Gaussian source, which is independent of the spatial dimension  $y$  can be written as,

$$T(k_x) = T_1(k_x)T_2(k_x)T_3(k_x), \quad (3.17)$$

where  $T_1(k_x) = e^{-k_x d_0}$  is the transfer function of the homogeneous medium with electric permittivity  $\epsilon_{r0}$ , magnetic permeability  $\mu_{r0}$  and thickness  $d_0$ , filling the space from the source plane to the lens;  $T_2(k_x) = e^{-k_x d_2}$  is the transfer function of the homogeneous medium  $\epsilon_{r2}$ ,  $\mu_{r2}$  and thickness  $d_2$  filling the space from the lens to the image plane, and  $T_3(k_x)$  is the expression provided in equation (3.14).

The field distribution in the image plane can be calculated by inverse Fourier transforming the convolution of the source Fourier transform multiplied by the transfer function as, In order to test the tunable character of subwavelength imaging with lens made of metal dielectric composite, table 3.1 provides the

filling fractions and different working frequencies which composite slabs succeed subwavelength imaging.

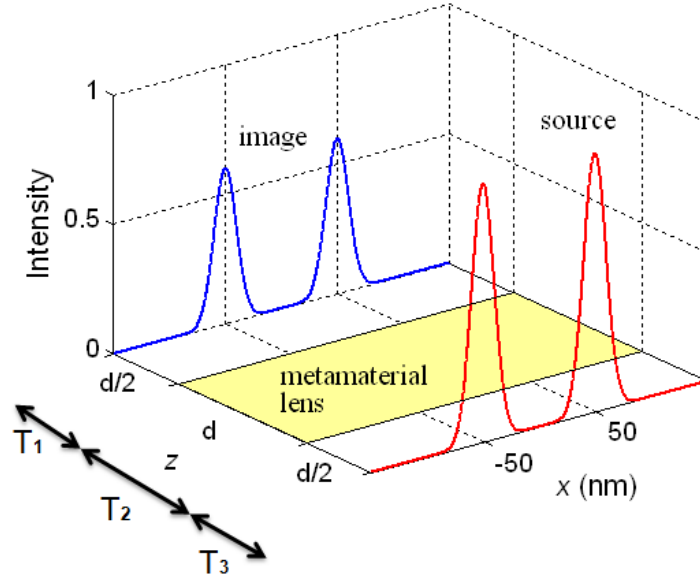


Figure 3.9 Imaging system set up.

$$g(x, y, z_2) = \int G(f_x, f_y) T(k_x) e^{i2\pi(f_x x + f_y y)} dk_x dk_y. \quad (3.18)$$

It also provides the complex values for the dielectric function silver slabs at the same frequency.

Table 3.1 relative effective permittivity for silver-silica composite and relative permittivity for  $\epsilon$  for bulk silver

	Ag-Sio2	Composite	Silver	
	$\epsilon_{reff}'$	$\epsilon''_{reff}$	$\epsilon_r'$	$\epsilon''_r$
$\lambda = 397 \text{ nm}$				
$f=0.1$	-1	0.172	-3.71	0.059
$\lambda = 385 \text{ nm}$				
$f=0.2$	-1	0.092	-3.2	0.054
$\lambda = 375 \text{ nm}$				
$f=0.3$	-1	0.067	-2.78	0.05

Figures 3.10 to 3.12 compare the imaging ability of the Ag-SiO<sub>2</sub> composite and bulk Ag for given wavelengths in table 3.1. As it is shown the composite superlens is capable of subwavelength imaging at different wavelengths while the silver slab fails to carry enough spatial harmonics for the image with subwavelength feature in the image plane.

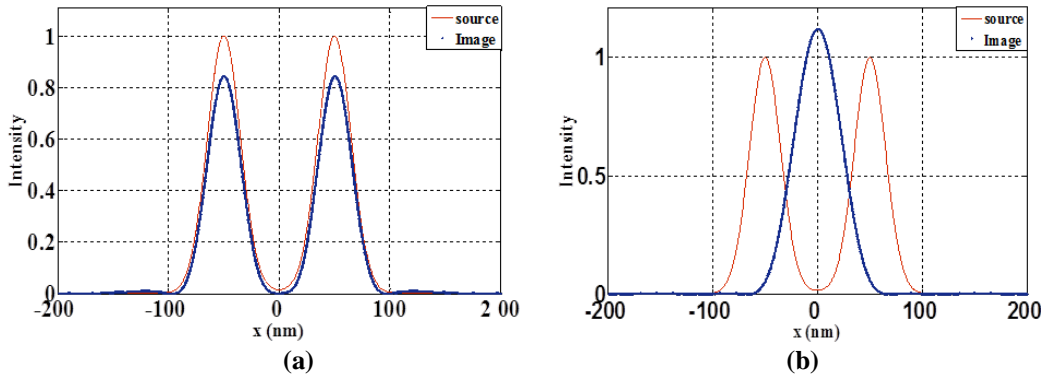


**Figure 3.10**  $\lambda=397$  nm, Slab thickness = 20 nm, (a) Composite ( $\epsilon = -1 - i 0.172$ ) (b) Silver ( $\epsilon = -3.71 - i 0.059$ )

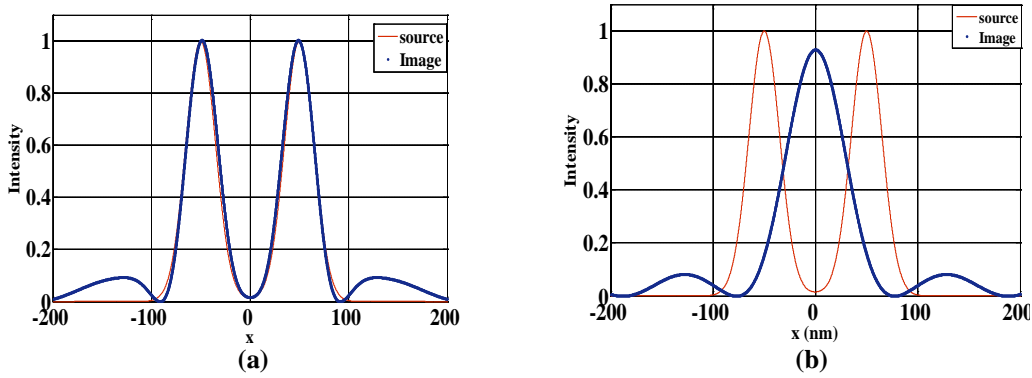


**Figure 3.11**  $\lambda=385$  nm, Slab thickness = 30 nm, (a) Composite ( $\epsilon = -1 - i 0.092$ ) (b) Silver ( $\epsilon = -3.51 - i 0.054$ ).

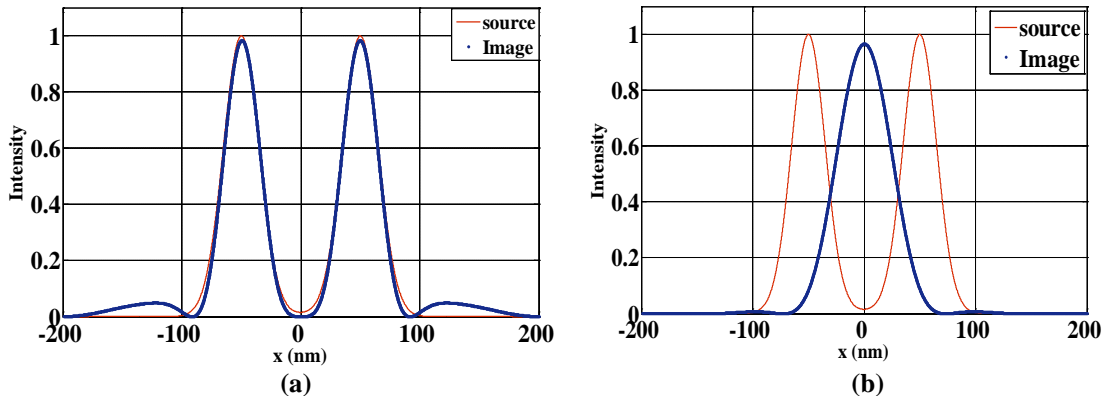


**Figure 3.12**  $\lambda=375$  nm, Slab thickness = 30 nm, (a) Composite ( $\epsilon = -1 - i 0.067$ ) (b) Silver ( $\epsilon = -2.78 - i 0.05$ ).

### 3.4 Optimized Single Layer Tunable Composite Superlens

Although the subwavelength imaging with composite slabs is achieved for different frequencies, the provided values in the table 3.1 are not optimized yet. In addition the intrinsic size effect which corrects the dielectric function of the silver nanoparticles is not considered. The primary parameters of the design procedure are the filling factor of the nanoparticles, the working frequency and the thickness of the lens, which are determine with optimization procedure. Constrains are enforced on the design parameters to obtain implementable composite parameters and to remain in the frame of the developed mixing rules. In the following composite lens made of silver nanoparticles with a radius of 2 nm immersed in SiO<sub>2</sub> host is considered. Two composite material based imaging configurations are investigated. In the first configuration the thickness of the lens is 20 nm and it is surrounded with air. The source-lens and lens-image distances are 10 nm. In the second configuration the thickness of the lens is 30 nm and the surrounding material is SiO<sub>2</sub>. The source-lens and lens-image distances are 15 nm. To understand the nature of the optimization problem in order to successfully design the metamaterial based imaging device the error surface of the objective function which is defined as the normalized absolute difference between the source and image, is mapped.

$$\Omega = \frac{1}{N_x} \sum_{j=1}^{N_x} |g(x_j, z_2) - g(x_j, 0)|, \quad (3.19)$$

where  $N_x$  is the number of points in the x direction. Figures 3.13 (a) and (b) present the error surfaces in function of the frequency and filling factor for the air-

composite-air configuration and for the SiO<sub>2</sub>-composite-SiO<sub>2</sub> case. The error surface demonstrates the optimized filling fraction and frequency, that the best imaging quality can be achieved. For instance in figure 3.13(a), the best imaging quality can be achieved for  $f \sim 0.5$  at the frequency of 0.84 PHz. The maps of the objective function are extremely complex with several hills and valleys and large flat regions, therefore gradient based optimizations fails to find useful parameters unless the optimization procedure is not started from the close proximity of the parameter regions where imaging is possible. Nevertheless the differential evolution based optimization [8] can be successfully applied for such objective functions. For the current problem a population size of 200-300 and maximum iterations of 100-200 are sufficient to converge to the proximity of the global minimum. The procedure requires to set searching interval for the variables of the optimization. The optimum frequency is searched in the interval [0.4-1] PHz. The lower limit of the filling factor is set to 0 but the upper limit is set successively to 0.2, 0.3, 0.4 and 0.5 for different instances of the optimization. The differential evolution algorithm converges to the upper limit of the filling factor. The marked points of figure 3.13 (a) and (b) are the results of the optimization procedure obtained for the different constrains of the filling factor. The blue color indicates the regions where subwavelength imaging is possible,

which is a thin curved valley in the space of the related frequencies and filling factors. The regions with high filling factors are out-side of the range where the Maxwell-Garnett type mixing rules can produce accurate results and they are plotted only as reference, to join the case of the dense Ag thin film with filling factor  $\zeta = 1$ . In figure 3.13 (c) the transfer function of the 20nm thick composite lens (red) surrounded with air, filling factor  $\zeta = 0.5$  and working frequency  $f = 0.843$  PHz are presented, which corresponds to point 4 in figure 3.13 (a). Figure 3.13 (e) presents the source, the image calculated with the Maxwell-Garnett and with the Mie scattering based effective medium theory. The size of the inclusions is deep subwavelength; therefore the high frequency mixing rule produces similar results as the Maxwell-Garnett theory, which approximates the metallic inclusions with static electric dipoles. For reference the transfer function and the image without the lens which corresponds to a 40 nm thick air region, is presented as well. The flat piece of the transfer function of the air corresponds to the frequency region bellow cutoff where propagating waves are resent. In the absence of the lens the propagating waves can reach the imaging plane without any distortion, therefore for propagating components the magnitude of the transfer function equals one. The lens is not impedance matched consequently for the propagating components reflections occurs and the magnitude of the transfer function is less



than one. In the absence of the lens the evanescent components are exponentially attenuated. The optimized lens can amplify several evanescent components and achieves higher resolution in the image plane. In figure 3.13 (d) and (f) the transfer function and the image produced by the 30 nm thick composite lens surrounded with SiO<sub>2</sub>, filling factor  $\zeta = 0.5$  and working frequency  $f = 0.79$  PHz are presented, which corresponds to point 4 in figure 3.13 (b). The intensity distributions in the image plane in function of the filling factor are collected in figure 3.14 (a) and 8(b). Increasing the upper limit of the filling factor in the optimization procedure the resolution of the image is improving and the optimum working frequency is shifting to higher values. The parameters of the lens corresponding to points 1-4 of figure 3.13 (a) and (b) and the corresponding effective electric permittivity calculated by taking into account the intrinsic size effect are summarized in Table 3.2.

**Table 3.2** The filling factor, the frequency and the effective electric permittivity of the single layer composite lens

Lens surrounded with air d = 20 nm			Lens surrounded with SiO <sub>2</sub> d = 30 nm			
$\xi$	f (PHz)	$\epsilon_{eff}$	$\xi$	f (PHz)	$\epsilon_{eff}$	
1	0.2	0.8036	0.19 - 1.54 i	0.2	0.7744	-0.28 - 2.42i
2	0.3	0.8179	-0.29 - 1.47i	0.3	0.7791	-1.18 - 2.35i
3	0.4	0.8310	-0.55 - 1.37i	0.4	0.7842	-1.72 - 2.14i
4	0.5	0.8431	-0.78 - 1.31i	0.5	0.7906	-2.01 - 1.91i

The simulations show that with an increase in the filling factor the effective elect-

electric permittivity converges to values where the losses are minimum and the lens is impedance matched to the surrounding medium as much as it is possible.

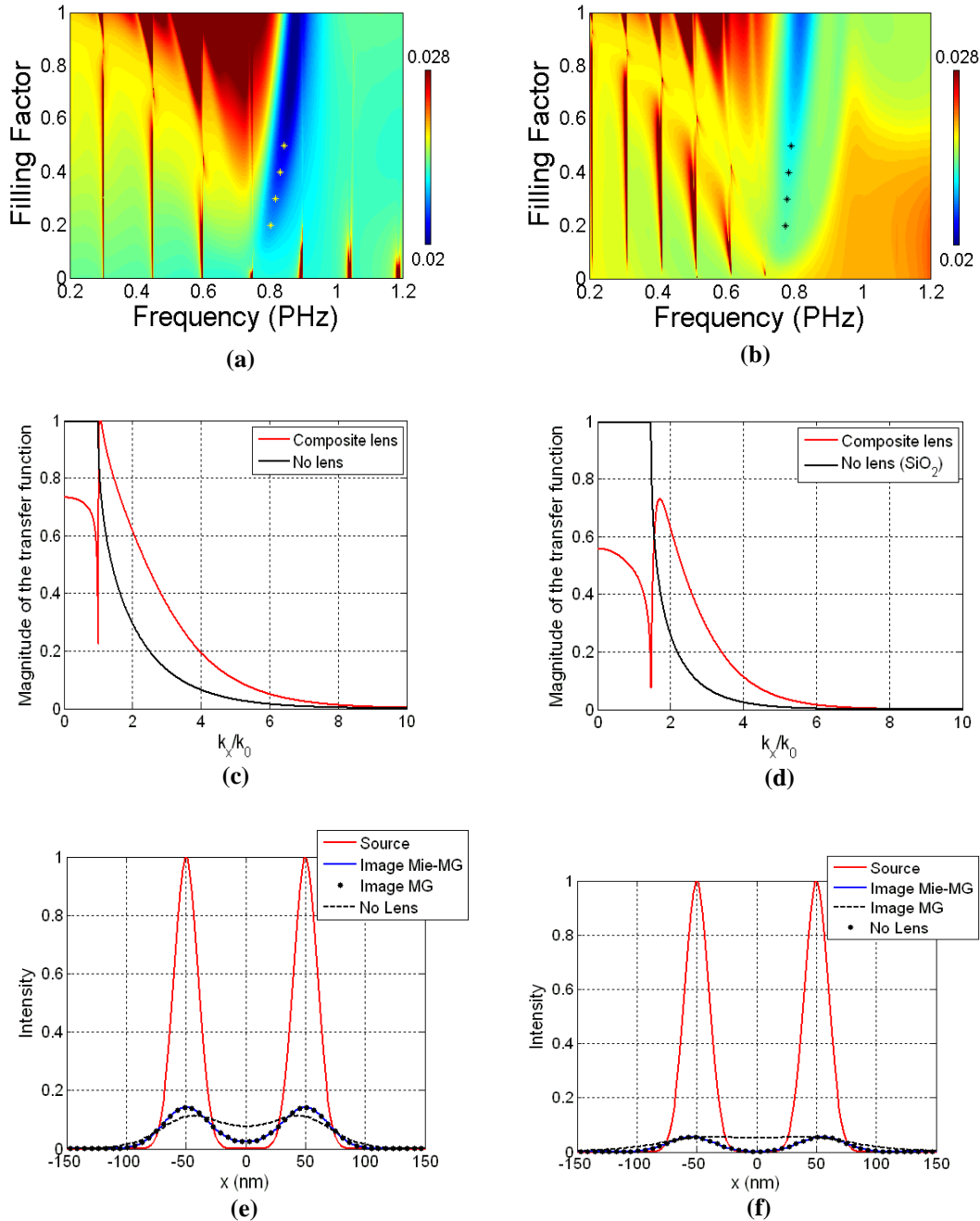


**Figure 3.13** Design of the imaging device with the single layer composite lens. The first column refers to the lens with thickness of 20 nm and surrounded with air, while in the second column the thickness of the lens is 30 nm and it is surrounded with SiO<sub>2</sub>. The error surfaces, which are searched by the optimization procedure are presented in (a) and (b). The markers indicate optimized results obtained with constrains on the filling factor. The transfer functions of the composite lenses are presented in (c) and (d). The intensity distributions in the source and image planes are plotted in (e) and (f). For reference the transfer function and the image without the lens are presented as well.

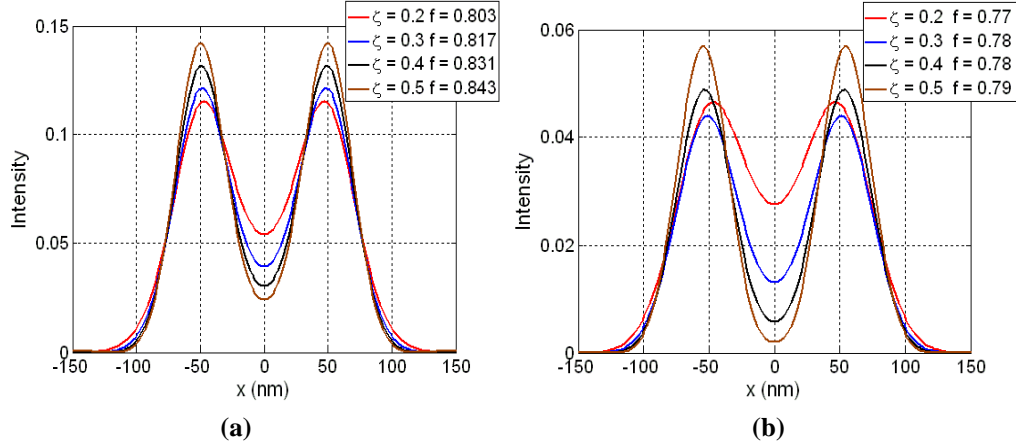


**Figure 3.14** The intensity distributions in the image plane corresponding to points 1-4 of figure 3.13 (a) and (b). Intensity in the image plane formed by (a) air-composite-air (b) SiO<sub>2</sub>-composite-SiO<sub>2</sub>

### 3.5 Imaging with Multilayer Composite Superlens

In subwavelength imaging systems with isotropic metal layer based superlenses, the evanescent waves grow exponentially until a particular film thickness thereafter; the material loss becomes more prominent [6,7]. Hence, the multilayer lens is greatly advantageous to establish a feasible spacing between the sample and its image. For multilayer lenses the steps of the computational methodology are similar, except the calculation of the transfer function which is performed with the Transfer Matrix Method (TMM). The method is based on (i) defining a boundary condition matrix [D] which is developed based on continuity of tangential components of E-field and H-field on the interfaces and (ii) phase shift matrix [P] which focuses on the phase shift the plane waves experience while travelling inside a layer. The transfer matrix for  $m_{th}$  layer then is defined as  $M_m = [DPD^{-1}]$ ,

$$M_m = \begin{bmatrix} \cos(k_z^m d_m) & i \frac{\omega \varepsilon_r^m}{k_m^z} \sin(k_z^m d_m) \\ i \frac{k_m^z}{\omega \varepsilon_r^m} \sin(k_z^m d_m) & \cos(k_z^m d_m) \end{bmatrix}, \quad (3.20)$$

where  $d_m$  is the thickness,  $\varepsilon_r^m$  is the electric permittivity and  $k_z^m$  is the wave number of the layer with index  $m$ . Starting from the image plane, the matrices  $M_m$  are multiplied consecutively:

$$M = \prod_{m=n+1}^0 M_m = \begin{bmatrix} M_{11} & M_{12} \\ M_{13} & M_{14} \end{bmatrix}. \quad (3.21)$$

The transfer function is given by the following expression,

$$T(k_x) = \frac{2}{M_{11} + \frac{\omega \varepsilon_r^0}{k_z^0} M_{21} + \frac{k_z^{n+1}}{\omega \varepsilon_r^{n+1}} (M_{12} + \frac{\omega \varepsilon_r^0}{k_z^0} M_{22})}, \quad (3.22)$$

where  $k_z^0$  is the wave number and  $\varepsilon_r^0$  is the electric permittivity in front, while  $k_z^{n+1}$  is the wave number and  $\varepsilon_r^{n+1}$  is the electric permittivity behind the multilayer lens, figure 3.15. In the presented methodology, the interactions between the inclusions of different layers are disregarded, and the electromagnetic material parameter of each layer is considered independent by the composition of any other layer.

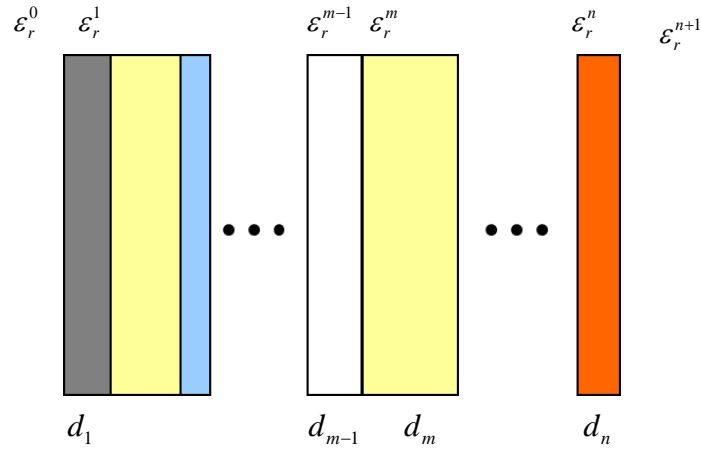
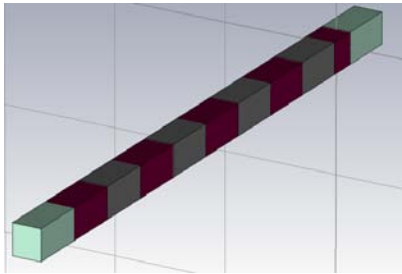


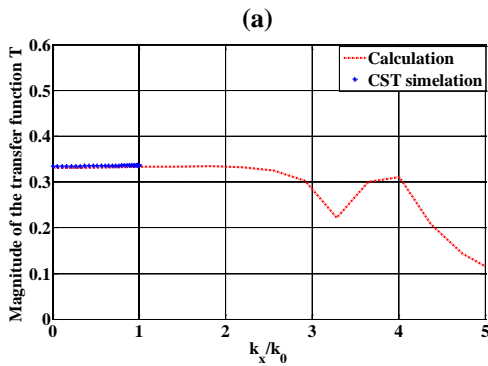
**Figure 3.15** The configuration of the multilayer lens.

In order to test the accuracy of the derived expression for the transfer function, a silver-PMMA multilayer structure is simulated with CST full-wave simulator and the result of the simulation, S21, is compared with analytic expression in equation (3.22).

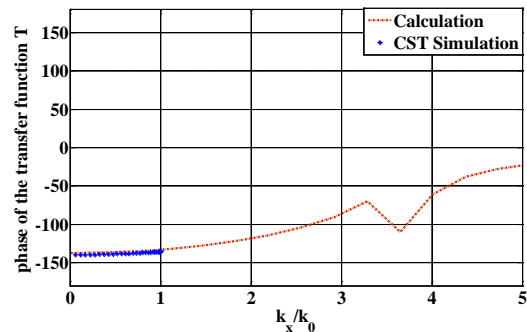


$\epsilon_r$	Silver : $-2.7 - 0.23i$					PMMA : $2.3013 - .0014 i$				
Dimension(nm)	10	5	10	10	10	10	10	10	10	10

(b)



(b)



(d)

**Figure 3.16** Transfer function of silver-PMMA layered structure CST simulation versus analytical calculation (a) &(b) Schematic of silver slab in CST (c) Magnitude of transfer function (d) Phase of the transfer function.

The developed effective medium theory allows the calculation of the effective electric permittivity of spherical multilayer metal-dielectric inclusions. The developed procedure is applied to design multi-layer lenses made of metallic composite and SiO<sub>2</sub> layers. The metallic composite is made of silver nanoparticles with a radius of 2 nm immersed in SiO<sub>2</sub> host. The medium in front and behind of the multilayer lens is air. The parameters of the optimization are the

filling factor, the frequency and the thicknesses of individual layers. The searching intervals of the frequency and filling factor are set in a similar way as the bounds of the single layer lens. The number of composite layers is two or three and their thickness are optimized independently.

The first and the last layer of the lens are always made of composite material. In the optimization procedure the maximum value of the thickness of all individual layers, including the air regions in front and behind of the lens is set to 50 nm. The minimum thickness of the air regions is 5 nm, of the composite layers is 10 nm and of the SiO<sub>2</sub> separation layers is 5 nm or 10 nm respectively. The optimization returns the upper bound for the filling factor and the lower bound for the thicknesses. The design parameters of the multilayer lens are collected in Table 3.3 The third column presents the geometry parameters, where the thicknesses of the air regions are indicated with italic and the thickness of the composite layers with bold numbers. The absolute error between the intensity distribution in the source and image planes are presented in the fourth column. For reference the effective electric permittivity of the designed composite material are included in the table.

**Table 3.3** The design parameters of the multilayer lens

$\xi$	f (PHz)	Thicknesses (nm)	Error ( $\times 10^{-2}$ )	$\epsilon_{eff}$	
1	0.4	0.8171	5 <b>10</b> 10 <b>10</b> 5	1.98	-0.85 - 1.54 <i>i</i>
2	0.5	0.8272	5 <b>10</b> 10 <b>10</b> 5	1.92	-1.06 - 1.43 <i>i</i>
3	0.4	0.8235	5 <b>10</b> 5 <b>10</b> 5	1.89	-0.72 - 1.46 <i>i</i>
4	0.5	0.8348	5 <b>10</b> 5 <b>10</b> 5	1.81	-0.89 - 1.36 <i>i</i>
5	0.4	0.8227	5 <b>10</b> 5 <b>10</b> 5 <b>10</b> 5	2.16	-0.73 - 1.47 <i>i</i>
6	0.5	0.8336	5 <b>10</b> 5 <b>10</b> 5 <b>10</b> 5	2.11	-0.92 - q.37 <i>i</i>

The imaging capabilities of the designed multilayer lenses with the parameters listed in Table 3.3 are presented in figure 3.17. The curves 1-4 refer to the lens with arrangement of composite-SiO<sub>2</sub>-composite, while curves 5 and 6 to the lens with composite-SiO<sub>2</sub>-composite-SiO<sub>2</sub>-composite arrangement. The transfer functions are presented in figure 3.17(a), and the intensity distributions of the image plane are plotted in figure 3.17 (b).

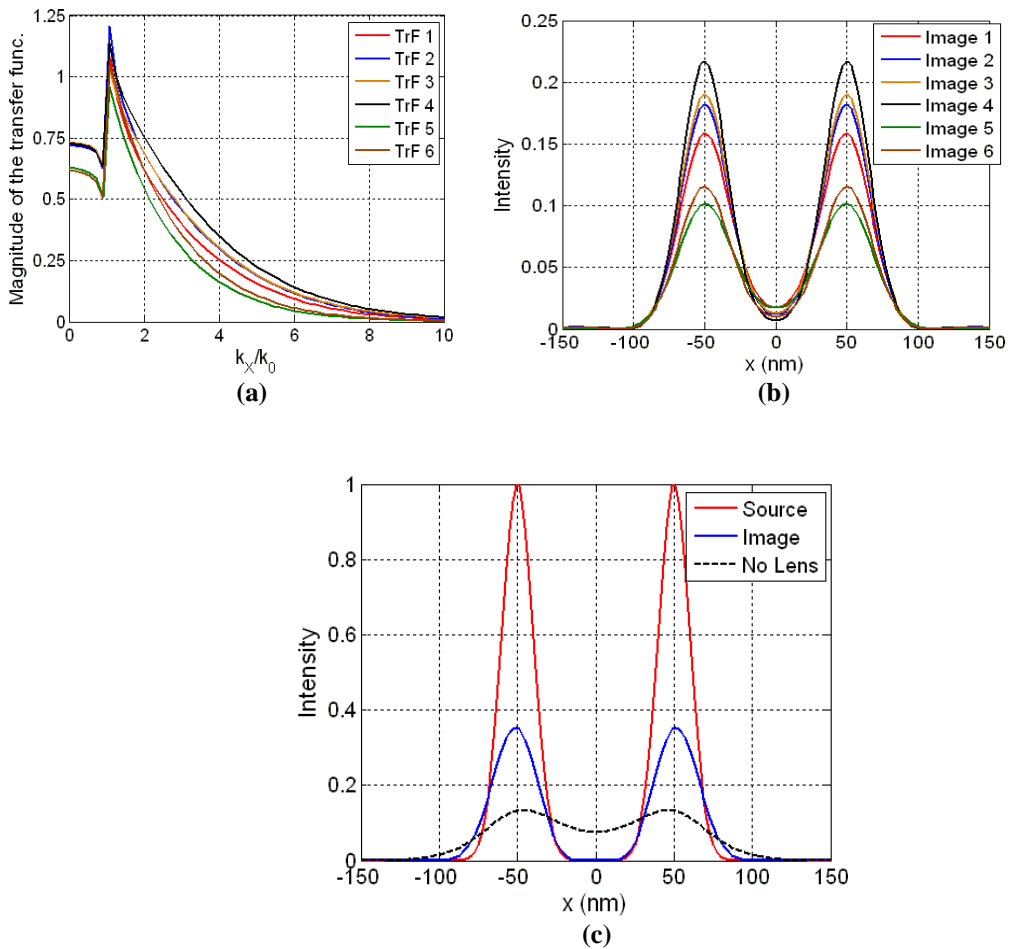


**Figure 3.17** Imaging with the multilayer lens. In (a) the transfer functions, and in (b) the images corresponding to the parameters presented in Table 3.2 are shown. The intensity distribution of the source and of the image for the lens, with parameters presented in the fourth row of the table 3.2, along with the reference image without the lens are shown in (c)

Similar to the single layer lens, the figures show increase of the resolution in function of the filling factor. The resolution is increased as well by decreasing the SiO<sub>2</sub> separation layer between the metallic composite films, therefore the highest resolution can be achieved with the layers 10 nm composite, 5 nm SiO<sub>2</sub>-10 composite as it is plotted in 3.17(a). The separation between the source and image plane can be increased by adding more layers to the composite lens, which does not alters the shape of the transfer function considerably, only the magnitudes are reduced according to the additional losses.

### **3.6 Conclusion**

The methodology to design single and multilayer flat metamaterial lenses has been presented. The composite layers of Ag inclusions immersed in SiO<sub>2</sub> host are proposed as lens and implementable geometrical dimensions and composition has been determined with optimization. These results support the use of a waveguides with metallic composite layer- dielectric layer- metallic composite layer arrangement for tunable optical imaging application with high subwavelength spatial resolution. In addition metallic composites with deep wavelength inclusions may also eliminate the hotspots present in the images of metallic superlens.



## Reference

- [1] J. C. Garnett, Maxwell. "Colours in metal glasses, in metallic films, and in metallic solutions. II." *Phil. Trans. R. Soc. L. Series A*: 237-288, (1906).
- [2] D. A. G. Bruggeman," Calculation of various physics constants in heterogeneous substances. Dielectricity constants and conductivity of mixed bodies from isotropic substances," *Ann. Phys. (Leipzig)* 24, 636–664 (1935).
- [3] IO. F. Mossotti," Mem.di mathem. e fisica in Modena," 24 11, 49 (1850).
- [4] R. Clausius." Die mechanische U'grmetheorie,"(1879).
- [5] W. Cai, and V. M. Šalaev," Optical metamaterials: fundamentals and applications," *Springer*, (2010).
- [6] B. Wood, J. B. Pendry, and D. P. Tsai, "Directed subwavelength imaging using a layered metal-dielectric system," *Phys. Rev. B* 74.11: 115116 (2006).
- [7] S. A. Ramakrishna, "Imaging the near field," *J. of Modern Opt.* 50.9 : 1419-1430, (2003).
- [8] K. V. Price, M. S. Rainer and A. L. Jouni "Differential evolution a practical approach to global optimization," (2005).

## **CHAPTER 4**

# **SUBWAVELENGTH IMAGING WITH METAL-DIELECTRIC COMPOSITES MADE OF NON-SPHERICAL NANOPARTICLES**

### **4.1 Introduction**

The tunable imaging with isotropic metal-dielectric composite is discussed in previous section. In metal-dielectric composite the only controlling factor which offers the tunability is the filling fraction of the metal or in another word the radius and numbers of the spheres. In this chapter, the composite thin film is made of deep subwavelength non-spherical metallic nano-particles embedded in a dielectric host. The optical properties of the composite depend on the shape, size, and orientation of the nano-particles, which provide sufficient degrees of freedom to optimize the superlens according to the wavelength of the available laser source. In addition to the higher degree of freedom, the aligned metallic nano ellipsoid in dielectric host can be effectively approximated as an anisotropic slab. The anisotropic slab with specific design is capable of subwavelength imaging for higher resolutions and is more robust to the loss due its specific mechanism of imaging.

In this chapter the application of effective medium theory to homogenize the composite with embedded randomly oriented/ aligned non-spherical metallic nano-particles is discussed. To evaluate the imaging performance of composites with randomly oriented ellipsoid nano-particles, the optical transfer function is calculated based on the transfer matrix method for an isotropic layered structure. To evaluate the imaging performance of composites with aligned nano-ellipsoid a novel algorithm is developed [1]. This algorithm offers a simple and completely analytical solution for the light interaction with generally anisotropic layered media. Finally, to achieve the highest possible resolution of the lensing system, the geometrical parameters and the orientation of the nano-particles, the filling fraction and the thickness of the individual layers are determined with differential evolution optimization algorithm.

## 4.2 Effective Medium Theory for Composites with Non-Spherical Nanoparticles

To homogenize composites with ellipsoidal inclusions, the key is to find the depolarization factor of ellipsoids. Fortunately, ellipsoid inclusions are among few shapes with available analytical solution for their depolarization.

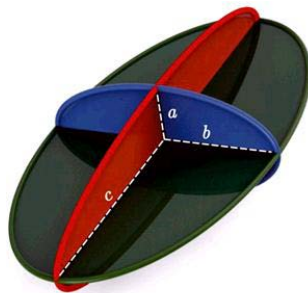


**Figure 4.1** The geometry of an ellipsoid. The semi-axes  $a_x$ ,  $a_y$  and  $a_z$  fix the Cartesian coordinate system.

According to figure 4.1, the depolarization factor  $N_x$  (the factor in  $a_x$  direction) is [2],

$$N_x = \frac{a_x a_y a_z}{2} \int_0^\infty \frac{ds}{(s+a_x^2) \sqrt{(s+a_x^2)(s+a_y^2)(s+a_z^2)}}. \quad (4.1)$$

For the other polarization factor  $N_y$  ( $N_z$ ), interchange  $a_y$  and  $a_x$  ( $a_z$  and  $a_x$ ) in the above integral. The three depolarizations for any ellipsoid should satisfy

$$N_x + N_y + N_z = 1. \quad (4.2)$$

Hence, for the sphere ( $N_x = N_y = N_z$ ), the depolarization factor is 1/3. If the co-ordinate is chosen such that  $a_x > a_y > a_z$ , then the polarization factors will be [2],

$$N_x = \frac{a_x a_y a_z}{(a_x^2 - a_y^2) \sqrt{(a_x^2 - a_z^2)}} [F(\varphi, k) - E(\varphi, k)], \quad (4.3)$$

$$N_z = \frac{a_y}{(a_y^2 - a_z^2)} \left[ a_y - \frac{a_x a_z}{\sqrt{(a_x^2 - a_z^2)}} E(\varphi, k) \right], \quad (4.4)$$

$$N_y = 1 - N_x - N_z. \quad (4.5)$$

$F(\varphi, k)$  and  $E(\varphi, k)$  are the incomplete elliptic integrals,

$$F(\varphi, k) = \int_0^\varphi \frac{d\theta}{\sqrt{1 - k^2 \sin^2 \theta}}, \quad (4.6)$$

$$E(\varphi, k) = \int_0^\varphi \sqrt{1 - k^2 \sin^2 \theta} d\theta, \quad (4.7)$$

where  $k$  is the elliptic modulus and  $\varphi$  is the amplitude.

### 4.3 Polarisability Components of an Ellipsoid

The broken geometry of the ellipsoid results in the dipole moment induction which depends on the direction of incident electric field. Hence the dipole

moment has a different direction than the field. In fact, the incident field and the dipole moment can be in the same direction only if the field's direction is aligned to the principal axis of the ellipsoid [2]. For instance, if an ellipsoid is shined with a uniform electric field polarized in the x direction ( $E_i$ ), the internal field ( $E_e$ ) is also uniform and x-directed with the ratio of

$$E_i = \frac{\varepsilon_e}{\varepsilon_e + N_x(\varepsilon_i - \varepsilon_e)} E_e. \quad (4.8)$$

Consequently, the polarisability component of the ellipsoid in x-direction field is,

$$\alpha_x = \frac{4\pi a_x a_y a_z}{3} (\varepsilon_i - \varepsilon_e) \frac{\varepsilon_e}{\varepsilon_e + N_x(\varepsilon_i - \varepsilon_e)}. \quad (4.9)$$

Following the same routine for the field in y and z direction the polarisability tensor is,

$$\bar{\alpha} = \begin{bmatrix} \alpha_x & 0 & 0 \\ 0 & \alpha_y & 0 \\ 0 & 0 & \alpha_z \end{bmatrix}. \quad (4.10)$$

In equation (4.10)  $N_y$  and  $N_z$  are found by replacing  $\alpha_x$  with  $\alpha_y$  and  $\alpha_z$  in equation (4.9), respectively. In the homogenization process, the polarisability tensor can be considered as an operator which acts on the external field to produce the dipole moment vector, as following,

$$P = \bar{\alpha} \cdot E_e. \quad (4.11)$$

#### **4.4 Effective Permittivity of Composites Made of Randomly Oriented Inclusions**

The classical way to determine the effective permittivity of a mixture is to follow the constitutive relation for a dielectric material [2] which is simple relation

between electric flux density  $D$  and electric field  $E$ . The effective permittivity connects the averaged value of  $D$  to averaged value of  $E$ ,

$$\langle D \rangle = \epsilon_{eff} \langle E \rangle = \epsilon_e \langle E \rangle + \langle P \rangle. \quad (4.12)$$

As the induced dipole moment in the ellipsoidal nano particles depends on the polarization of incident field two scenarios for effective permittivity of a composite with ellipsoidal inclusion may be considered: I. a composite with aligned ellipsoidal inclusions II. a composite with randomly oriented ellipsoidal inclusions.

#### 4.4.1 Randomly Oriented Inclusions

For randomly oriented inclusions (figure 4.2), macroscopically there is no longer any preferred direction as the dipolar moments in different directions cancel out each other due to the randomness in the orientation of nano-particles. Consequently the effective permittivity is no longer anisotropic and the mixture is isotropic.

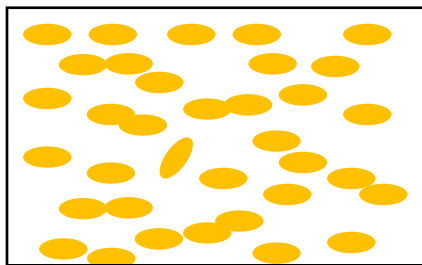


**Figure 4.2** A composite randomly oriented nano-ellipsoid particles.

The polarisability of each component participates equally to the macroscopic polarization density ( $\alpha$ ). The effective permittivity of the mixture is [2]:

$$\epsilon_{eff} = \epsilon_e \left( 1 + \frac{\frac{f}{3} \sum_{j=x,y,z} \frac{\epsilon_i - \epsilon_e}{\epsilon_e + N_j (\epsilon_i - \epsilon_e)}}{1 - \frac{f}{3} \sum_{j=x,y,z} \frac{\epsilon_i - \epsilon_e}{\epsilon_e + N_j (\epsilon_i - \epsilon_e)}} \right), \quad (4.13)$$

Figure 4.3 demonstrates the optical property of a mixture with randomly oriented ellipsoidal nano particles with different shapes. The composites are made of silver inclusions embedded in SiO<sub>2</sub> host.

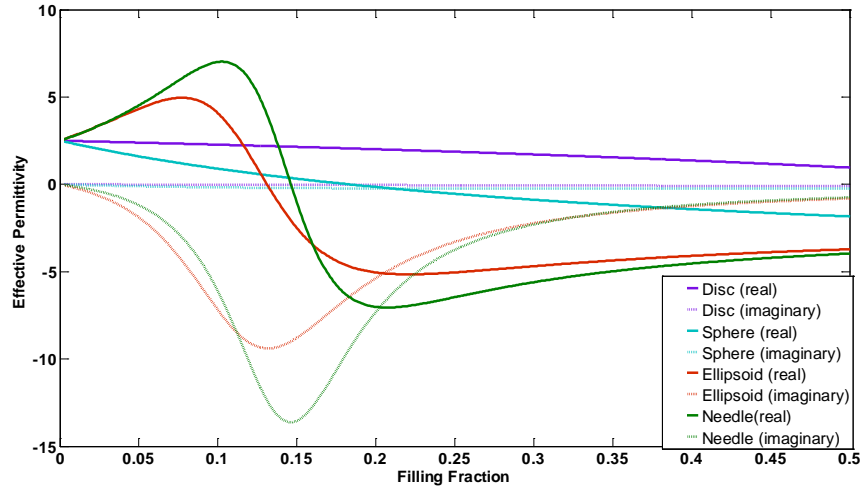


**Figure 4.3** the optical property of mixture with randomly oriented ellipsoids

#### 4.5 Imaging with Randomly Oriented Non-Spherical Nanoparticles

As the optical property of a mixture with randomly oriented inclusions is isotropic, the same optical transfer function developed in chapter is used to evaluate the subwavelength imaging performance. This transfer function is calculated based on the transfer matrix method which provides the exact solution of Maxwell equations for waves propagating in isotropic multilayer structures. Figure 4.4 shows the optical imaging system. The composite thin film is made of deep subwavelength metallic non-spherical nanoparticles, which can support dipolar plasmonic modes, embedded in a dielectric host. The optical properties of

the composite depend on the shape, size, and filling fraction of nanoparticles, which provide sufficient degree of freedom to optimize the superlens according to the wavelength of the available laser sources. To achieve the highest possible resolution of the lensing system, the geometrical, the filling fraction and the thickness of the individual layers are determined with differential evolution optimization algorithm [3].

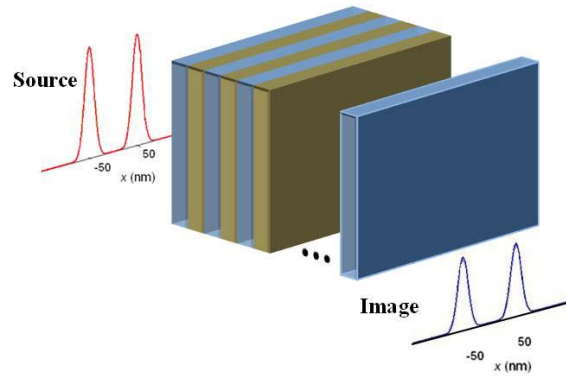


**Figure 4.4** The image formation of the imaging system made of composite thin film layers separated with dielectric slabs.

Similar to the previous chapter the objective function is defined as the normalized absolute difference between the source and image:

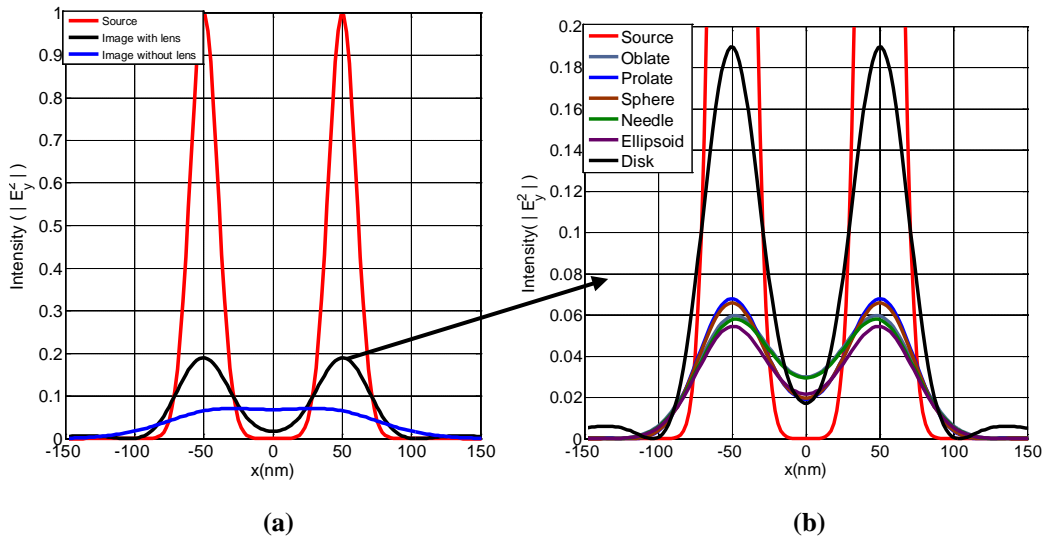
$$\Omega = \frac{1}{N_x} \sum_{j=1}^{N_x} |g(x_j, z_2) - g(x_j, 0)|. \quad (4.14)$$

#### 4.5.1 Subwavelength Imaging with Single Layer Composite Lens

Figure 4.5 presents the subwavelength imaging with mixtures with randomly oriented ellipsoids nanoparticles and special cases of ellipsoid shapes such as needles, oblates, and prolates, disks, and needles. The geometrical information, filling fraction of plasmonic nanostructure in each layer, number and thickness of



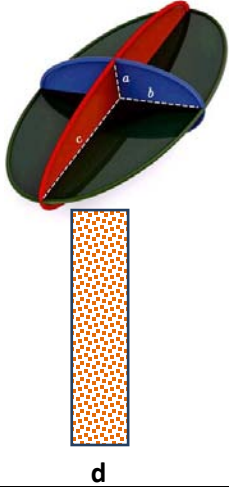
the layer and effective optical property of each mixture is provided in table 4.1. As it is shown in figure 4.5 (b), a composite slab with nano-disk metallic inclusions provides the best result for subwavelength imaging, and the image has the highest peak which results in better signal to noise ratio in a realistic noisy system.



**Figure 4.5** Subwavelength imaging (a) with and without lens (b) imaging with single layer composite-dielectric lens for composite made of inclusions with different ellipsoidal shape

In addition, as the optimized working wavelength is the highest (475nm) for this composite, table 4.1 shows that the achieved resolution is the best among all composite slabs with different inclusion's shape. As it is shown in table 4.1 the real part of effective permittivity of composite with nano-disk inclusions is the closest match to the air and the imaginary part is the lowest among all which reveals the reason behind the better performance of this particular composite.

**Table 4.1** Optimized parameters for subwavelength imaging with single layer composite-dielectric lens

Shape	Sphere	Prolate	Oblate	Ellipsoid	Needle	Disc	Geometry
Filling Fraction	0.5	0.5	0.5	0.5	0.5	0.5	
Wavelength(nm)	352	356	361	368	412	475	
<b>c</b> (nm)	5	5	5	5	5	5	
<b>b</b> (nm)	5	4	5	4	$\ll c$	5	
<b>a</b> (nm)	5	4	4	3	$\ll c$	$\ll c$	
<b>d</b> (nm)	30	30	30	30	30	30	
Resolution	$\lambda/3.52$	$\lambda/3.56$	$\lambda/3.61$	$\lambda/3.68$	$\lambda/4.12$	$\lambda/4.75$	
$Re(\epsilon_{eff})$	-0.95	-0.92	-0.6	-0.62	-0.767	-1	
$Im(\epsilon_{eff})$	-0.94	-0.96	-1.1	-1.1	-1	-0.47	

#### 4.5.2 Subwavelength Imaging with Layered Composite-dielectric Lens

In subwavelength imaging systems with isotropic metal layer based superlenses, the evanescent waves grow exponentially until a particular film thickness thereafter; the material loss becomes more prominent. Hence, the multilayer lens is greatly advantageous to establish a feasible spacing between the sample and its image. Figure 4.6 demonstrates the subwavelength imaging with layered composite-dielectric structure. The working frequency, thickness of layers and filling fractions are optimized by differential evolution algorithm. The respective information is given in table 4.2. As optical property of composites are approximated with Maxwell-Garnett effective medium theory the upper bound of filling fraction in the optimization process is set to 5, to avoid percolation. The nano particles are chosen to have 5 nm for their biggest diameter. The lower


bound of layers thickness is chosen to be 10 nm and the upper bound to be 25 nm. From the provided data in table 4.2 it is concluded that the optimizer always tends to the highest filling fraction and lowest slab thickness for the lowest cost function. In order to compare the performance of single layer and multilayer lens the same thickness of the lens in single layer is divided into three slabs and spaced by dielectric medium (air here) to form a 5 layer arrangement as is shown in table 4.2.

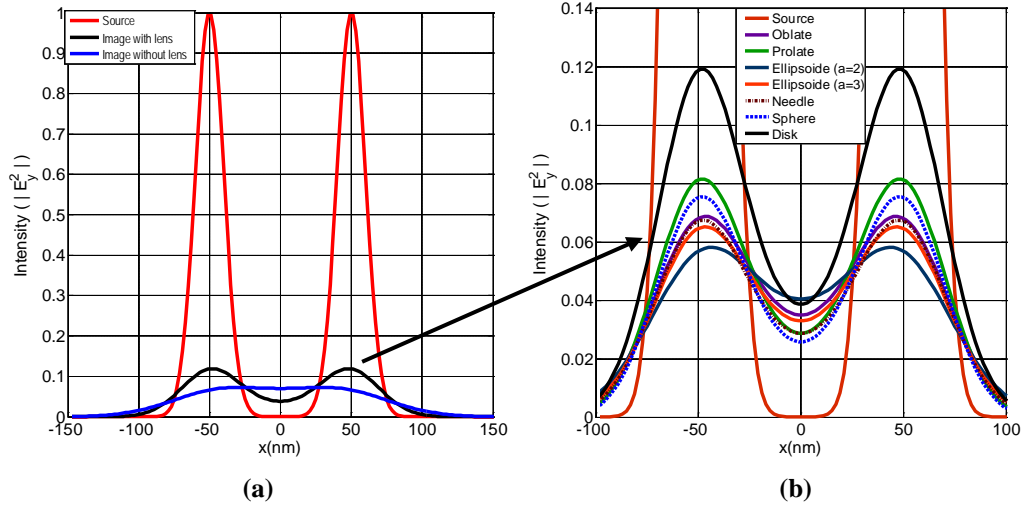
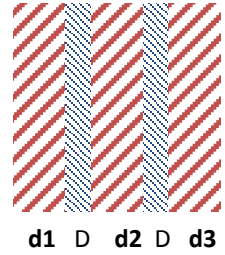


**Figure 4.6** (a) Subwavelength imaging with and without multilayer composite-dielectric lens (b) imaging with multilayer composite-dielectric lens for composite with inclusions of different ellipsoidal shape

$D$  is the thickness of the dielectric slabs which is set to be  $(d_1+d_2+d_3)/4$  and the same spacing is considered for the distance between source plan and image plane and the lens. It is observed that the layered structure is more robust to loss and can provide higher intensity of Gaussian pulses in the image plane by comparing figure 4.5(b) and figure 4.6(b) as it is expected. This conclusion is correct except to composite with disk-shape inclusions.

**Table 4.2** Optimized parameters for subwavelength imaging with layered composite-dielectric lens

Shape	Sphere	Prolate	Oblate	Ellipsoid	Needle	Disc	Geometry
Filling Fraction	.5	.5	.5	.5	.5	.5	
Wavelength(nm)	346	352.4	352.8	361	375	428	
c (nm)	5	5	5	5	5	5	
b (nm)	5	4	5	4	<< c	5	
a (nm)	5	4	4	3	<< c	<< c	
d1 (nm)	10	10	10	10	10	10	
d2 (nm)	10	10	10	10	10	10	
d3 (nm)	10	10	10	10	10	10	
Resolution	$\lambda/3.4$	$\lambda/3.52$	$\lambda/3.52$	$\lambda/3.6$	$\lambda/3.75$	$\lambda/4.28$	
$\epsilon_{eff}$	-1.11 -i0.9	-1-i0.99	-.66 -i1.15	-0.64 -i1.18	-0.76 -1.1	-0.7 -i0.48	



#### 4.6 The Effect of the Shape

Numerous experiments have been performed that measure the frequency variation of metallic nanoparticles based on changes in shape [3-7]. As the position of resonance wavelength depends on the shape of the particle, for non-spherical particles, multiple resonances will appear under unpolarized light, due to the difference in the size of allowed surface modes in different directions. For gold and silver nano ellipsoids, increasing the eccentricity causes red shifting of the largest peaks. This fact provides a degree of freedom to control the desired wavelength of imaging, with the shape of metallic nanoparticles. Figure 4.7 demonstrates the shift in the resonance peak of composite as the shape of the inclusion changes. The provided result in table 4.3, figure 4.5, table 4.4 and figure

4.6 agree well with the above discussion. As eccentricity increases from the sphere to the disk the optimum wavelength for imaging increases or red shifted.

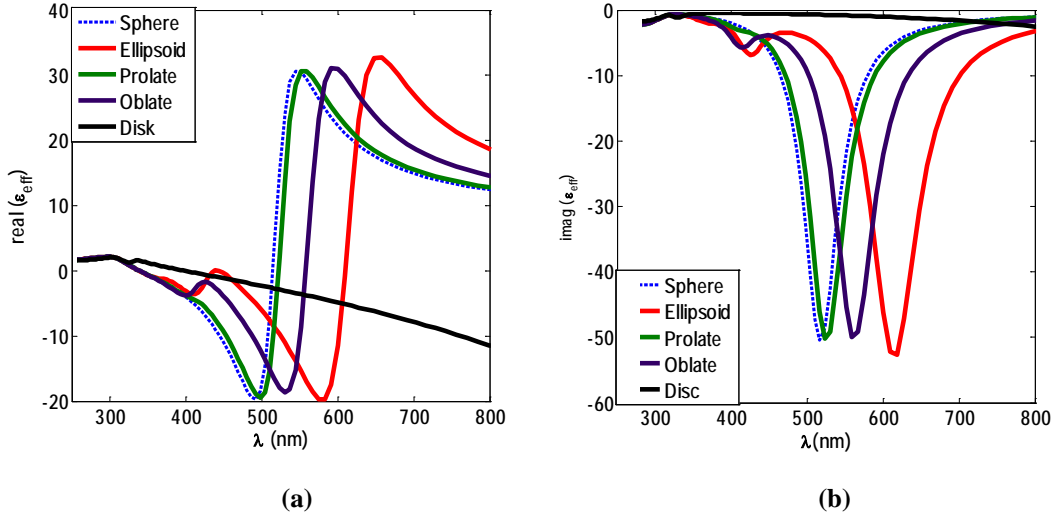


**Figure 4.7** The effect of the shape of inclusions on the effective permittivity (a) real part, (b) imaginary part of metal-dielectric composite. The metallic inclusions are Ag embedded in SiO<sub>2</sub> as a host medium. The filling fraction for all composites is 0.5

Figure 4.7 also provides the evidence for the superiority of imaging with nano-disc. As the resonant frequency of composite with nano-discs inclusions happens in higher wavelength, the matching condition is satisfied with smaller amount of loss which result in image with higher peak in the image plane.

#### 4.7 Effective Permittivity of Composites Made of Aligned Inclusions

Figure 4.8 shows a composite with aligned ellipsoid inclusions. Based on the polarisability tensor in equation (4.10) and equation (4.11) for effective permittivity, it is evident that the effective permittivity of the mixture is anisotropic and has different permittivity components in the different principal directions.

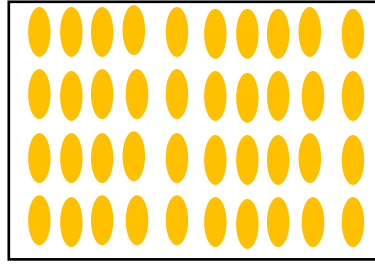


**Figure 4.8** A composite with aligned nano-ellipsoid particles

The Maxwell Garnett formula for the principal directions of the effective permittivity of this mixture is [2],

$$\varepsilon_{eff,j} = \varepsilon_e + f\varepsilon_e \frac{\varepsilon_i - \varepsilon_e}{\varepsilon_e + (1-f)N_j(\varepsilon_i - \varepsilon_e)} \quad j = x, y, z. \quad (4.15)$$

The effective permittivity tensor is then,

$$\overline{\overline{\varepsilon}}_{eff} = \begin{bmatrix} \varepsilon_{effx} & 0 & 0 \\ 0 & \varepsilon_{effy} & 0 \\ 0 & 0 & \varepsilon_{effz} \end{bmatrix}. \quad (4.16)$$

Figure 4.9 demonstrates the optical property of a mixture with aligned ellipsoidal nano particles.

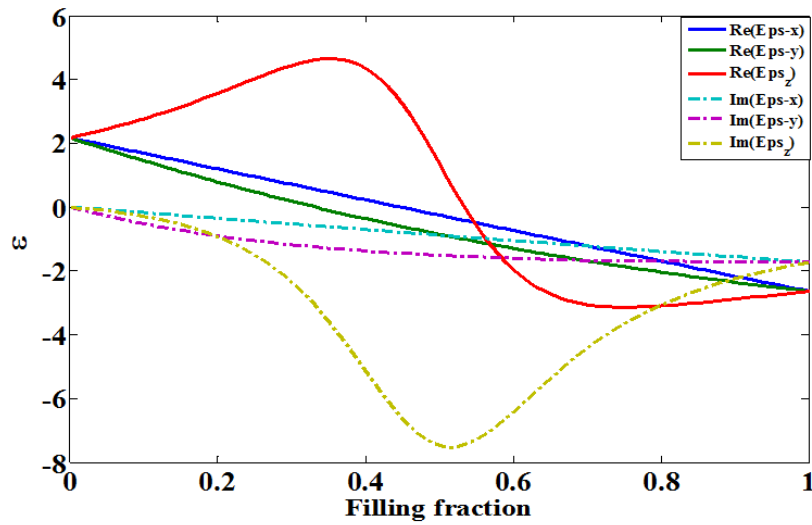


**Figure 4.9** the optical property of mixture with aligned ellipsoids

## **4.8 The Importance of Systematic Solution for Wave Propagation in Layered Anisotropic Medium**

The state of the art technology of the nano-fabrication facilitates the science and engineering society to implement intriguing applications with multilayer anisotropic structures. Novel layered anisotropic structures are applied in material science [8], electroanalytical chemistry [9, 10], biological interfaces and tissue engineering [11,12], physics and optics [8]. In nanostructuring of bulk silicon, by the variation of etching current in time, a layered structure with three-dimensional variation of the refractive index is fabricated. This structure offers variety of novel, polarization sensitive and silicon based optical devices such as efficient optical retarders, dichroic Bragg reflectors, dichroic micro-cavities, and Si-based polarizer [8]. In electrochemistry by anisotropic etching of silicon in alkaline solutions, complex micro electrical mechanical systems devices can be fabricated for various applications such as sensor, actuator or micro-fluidics systems [9]. In recent advances in tissue engineering, an anisotropic collagen gel scaffold with a hierarchical structure is developed to mimic the complicated anisotropic structure of native tissue [11].

To characterize the microscopic structural changes in these thin films, investigate their structure and their morphology and to delineate atomic and molecular level details of them, various characterization techniques are being used. In particular, Small X-ray scattering measurement [11], x-ray reflectivity [13], Raman spectroscopy [14], fluorescent spectroscopy [15], optical

ellipsometric spectroscopy [16], and infrared reflection spectroscopy [17] have proven to be the most useful techniques because of the high information content present in these spectroscopies, the relatively nondestructive sampling, high sensitivity for monolayer detectability, and the feasibility of in situ analysis in the presence of gases and liquids[18]. The functionality of these techniques depends on the propagation of the light in thin films. Usually the electric field component of the light interacts with the sample. This interaction is governed by the dielectric functions of the material and the sample geometry. The properties and the performance of the sample are then obtained by the information gained from the reflected and/or transmitted field. Consequently, a clear and relatively simple analytical approach that can derive the required information from the reflected or transmitted spectra is required.

Although the analytical investigation for electromagnetic wave propagation in anisotropic layered media has been a subject of interest for many years [14-25], the presented solutions are either not systematic enough for the treatment of general multilayer birefringent media [14-18], or in the case of general solutions, the solution becomes singular for isotropic layers [19, 21]. The general solution offered in [20] is involved with power series expansions and no explicit expressions are provided for the interaction of the wave with the incident and exit medium. In [23], the wave propagation is treated in more detail, but only for a single uniaxial layer. None of the papers [14-25] provides explicit expressions for the polarization of the electric and magnetic fields in each layer. The explicit expressions for the polarization of the electric field, magnetic field,



and the wave vector [21] in each layer, provides accurate information about the behavior of the electromagnetic wave propagating through layered structure for different applications [14-18, 20-22] and how the layered structure eventually transmits and reflects the incident wave [19-21]. Moreover, the polarization-dependent optical investigations have become standard methods to explore the properties of anisotropic solids and liquids [17-19], and hence it is important to derive analytical expressions for the polarizations in each layer for characterization purposes.

In the next section, based on the full-wave solution of the Maxwell equations, the explicit expressions of the electromagnetic field components in a multilayer with arbitrary oriented optical axis are presented. The Maxwell equations are solved in the k-space to find the explicit expressions of the partial fields. As it is convenient to reduce the number of electromagnetic field variables to a minimum, the six components of the E-field and H-field in each medium are expressed in terms of only one component. Based on the analytical expressions of vector field's polarizations, the boundary condition and propagation matrices are introduced for each layer, as the building blocks of the transfer matrix method. The methodology is suitable to calculate the transfer matrix of a layer with arbitrary thickness and anisotropy, for any angle of incidence under plane wave illumination. The reflection and transmission coefficients for the multilayer system, is derived from the relations between the amplitudes of the incident, reflected, and transmitted waves. It is shown that similar boundary condition matrix relates the transfer function of the layered structure to the amplitudes of

the waves in the incident and exit media. The method is suitable for propagating wave and evanescent wave calculations as well. In addition, it is shown that the derived anisotropic relation can be reduced to the isotropic case without any singularity in contrast to the method presented in [12, 14].

#### 4.8.1 Explicit Expressions for E-Field and H-Field Polarizations

In order to make the procedure transparent, the derivation of the polarizations of vector fields from Maxwell equations is provided here. For a non-magnetic medium with arbitrary anisotropy, the polarizations of fields depend on the permittivity tensor  $\bar{\bar{\epsilon}}$  and the wave vector  $\mathbf{k}$  in each medium. As the tangential component of the wave vector,  $k_x$  here, is known since it persists through the interface, the normal component,  $k_z$ , is found by combining basic curl relations in Maxwell equation for a generally anisotropic medium,

$$\nabla \times H = j\omega D, \quad (4.17)$$

$$\nabla \times E = -j\omega\mu H. \quad (4.18)$$

The combination of Equation (4.17) and (4.18) results in the wave equation in  $\mathbf{k}$  space. The nontrivial solution of the wave equation in an anisotropic medium is a quadratic wave equation that yields four roots. These four roots are the  $z$  components of the wave vectors in the anisotropic layer. The four explicit expressions for  $k_z$  are given in [14]. Two solutions have a real positive part and constitute the forward-traveling plane waves with respect to  $+z$ , while the other two solutions with negative real-parts are the back-propagating waves. In order to find the explicit expressions for the **E**-field and **H**-field polarization, equations

(4.17) and (4.18) are used. From equation (4.17),

$$(4.19) \quad \begin{cases} -\frac{\partial H_y}{\partial z} = j\omega D_x \\ \frac{\partial H_x}{\partial z} - \frac{\partial H_z}{\partial x} = j\omega D_y \\ \frac{\partial H_y}{\partial x} = j\omega D_z \end{cases} .$$

The coordinate system is chosen such that  $k_y = 0$ . From the first and the third relations in equation (4.19),

$$k_z(i)H_y = \omega(\varepsilon_{xx} E_x + \varepsilon_{xy} E_y + \varepsilon_{xz} E_z), \quad (4.20)$$

$$k_x H_y = -\omega(\varepsilon_{zx} E_x + \varepsilon_{zy} E_y + \varepsilon_{zz} E_z) \quad (4.21)$$

Here  $\varepsilon_{ij}$  ( $i, j \in \{x, y, z\}$ ) is the component of the permittivity tensor connecting  $D_i$  to  $E_j$  where D and E are the electric displacement and electric field, respectively. The combination of Equations (4.20), (4.21), and (4.19) results in the explicit expressions for the E-field polarization vector:

$$\vec{E} = \begin{bmatrix} 1 \\ \frac{-\alpha}{\gamma} - \frac{\beta\lambda}{\xi\gamma} \\ \frac{\lambda}{\xi} \end{bmatrix} E_x, \quad (4.22)$$

where  $\alpha, \beta, \gamma, \xi,$  and  $\lambda$  are defined as

$$\beta_l = \frac{\varepsilon_{xz}}{k_z(i)} + \frac{\varepsilon_{zz}}{k_x}, \quad (4.23)$$

$$\alpha_l = \frac{\varepsilon_{xx}}{k_z(i)} + \frac{\varepsilon_{zx}}{k_x}, \quad (4.24)$$

$$\gamma_l = \frac{\varepsilon_{xy}}{k_z(i)} + \frac{\varepsilon_{zy}}{k_x}, \quad (4.25)$$

$$\lambda_l = k_x \varepsilon_{xx} + k_z(i) \varepsilon_{xz} - (\varepsilon_{xy} - \varepsilon_{yz}) \frac{\alpha_l}{\gamma_l}, \quad (4.26)$$

$$\xi_l = k_x \varepsilon_{zx} + k_z(i) \varepsilon_{zz} + (\varepsilon_{xy} - \varepsilon_{yz}) \frac{\beta_l}{\gamma_l}, \quad (4.27)$$

The polarization vector for the H-field is determined by:

$$\vec{H} = \frac{\nabla \times E}{-j\omega\mu} = \begin{bmatrix} \frac{-k_z(i)}{\omega\mu} \left( \frac{-\alpha}{\gamma} - \frac{\beta\lambda}{\xi\gamma} \right) \\ \frac{1}{\mu\omega} (k_z(i) - k_x \frac{\lambda}{\xi}) \\ \frac{k_x}{\omega\mu} \left( \frac{-\alpha}{\gamma} - \frac{\beta\lambda}{\xi\gamma} \right) \end{bmatrix} E_x. \quad (4.28)$$

As is expected for an arbitrarily anisotropic material, the fields' components are coupled to each other and no decomposition to TE/TM polarization with respect to the direction of propagation is possible. In fact a plane wave in the arbitrarily anisotropic medium can be decomposed into two orthogonal waves, called *a-wave* and *b-wave* which are generalizations of the TE and TM waves in isotropic and uniaxially anisotropic media. The vectors, **a** and **b**, each with six components, are defined by the optical property of the medium [20].

#### 4.8.2 General Transfer Matrix

Assume an incident light wave coming from the incident ( $-\infty < z < 0$ ) medium with a complex relative permittivity of  $\varepsilon_i$ , at an angle of incidence of  $\theta_i$ ,  $A_{i,TE}$ ,  $A_{i,TM}$ ,  $B_{r,TE}$ , and  $B_{r,TM}$  are the complex amplitudes of the TE and TM modes of the incident and reflected waves, respectively. After interaction with a layered structure, the wave enters the exit medium,  $z_n < z < \infty$  and is characterized with the

complex transmission amplitude of  $A_{t,TE}$  and  $A_{t,TM}$  for transmitted TE and TM polarization respectively. The propagation occurs along the  $z$  direction and the layers' interfaces are in the  $x$ - $z$  plane. The origin is set at the plane which constitutes the interface of the incident ambient and the first layer. The wave vector of the incident field is chosen, without loss of generality, to have  $x$  and  $z$  components.

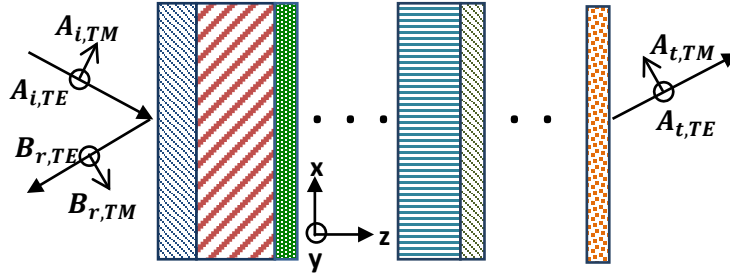


**Figure 4.10** Incidence, reflectance and transmittance of a plane wave

The incident wave, transmitted wave, and reflected wave, are related to each other by the transfer matrix of the layered system introduced as TF, in equation (4.31),

$$\begin{bmatrix} A_{i,TM} \\ B_{r,TM} \\ A_{i,TE} \\ B_{r,TE} \end{bmatrix} = TF \begin{bmatrix} A_{t,TM} \\ 0 \\ A_{t,TE} \\ 0 \end{bmatrix}. \quad (4.29)$$

If  $BC_0$  relates the incident and the reflected amplitudes to the tangential components of the E-field and H-field in the incident medium and  $BC_N$  connects the transmitted amplitude to the tangential components of the E-field and H-field in the exit medium, then  $T_l$  represents the transfer function of each layer, as follows,

$$TF = BC_0^{-1} (\prod_{i=1}^N T_l(d_l, \bar{\epsilon}_l)) BC_N. \quad (4.30)$$

### 4.8.3. The Transfer Function Development

The flowchart of the algorithm showing the development of the transfer matrix explicitly for the  $l_{th}$  layer, is presented in figure 4.11. The ordered product of the layers' transfer function from the first interface, at  $z=0$ , to the last interface at,  $z = z_n$ , in figure 4.10, results in the transfer function of the layered structure. In the absence of the current density and charge density in the interface regions, the tangential components of electric- and magnetic-field are continuous across the interfaces.  $BC_{l-1}$ ,  $BC_l$ , and  $BC_{l+1}$  in figure 4.11 represent the boundary condition matrixes which realize the continuity of the tangential components of the E-field and H-field in the  $l-1$ ,  $l$ , and  $l+1$  layers respectively.

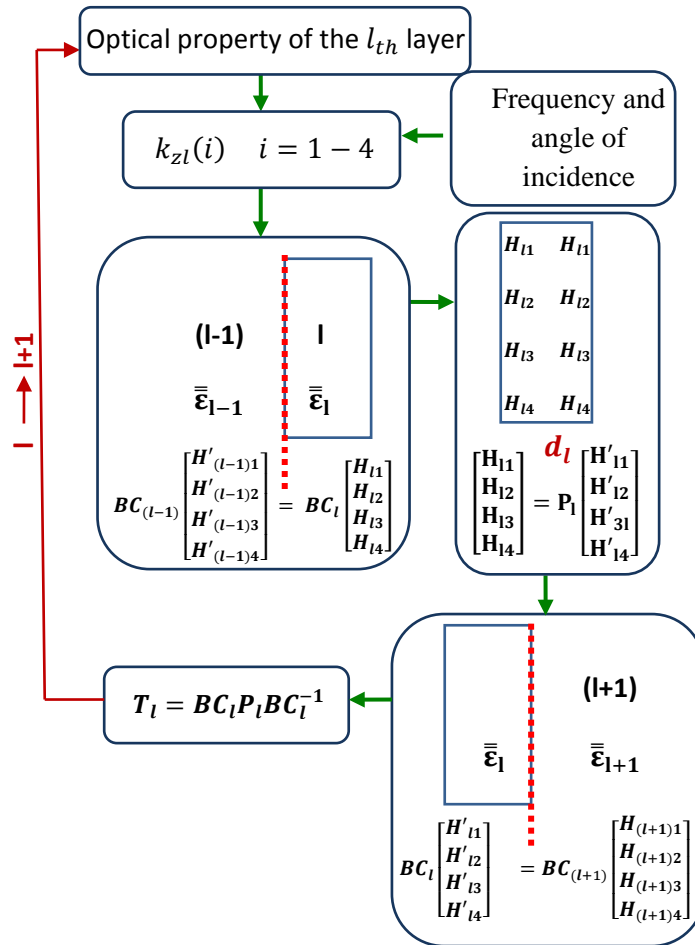


Figure 4.11. Transfer matrix development flowchart for the  $l_{th}$  layer

To form the BC matrix, four tangential components of the E-field and H-field in each medium are required. However, since the polarization vectors of the electric field and magnetic field are found analytically in section II, the number of variables can be minimized to one. Here, the y component of the H-field,  $H_y$ , is chosen, but others may be selected where convenient. As there are four different wave vectors, with the same  $k_x$  value but different  $k_z$  values, there are four partial fields which constitute each tangential component. The BC matrix presents the association of tangential components to the amplitude of the partial fields that constitute  $H_y$ , as shown in the following,

$$\begin{bmatrix} \sum H_{yl} \\ \sum E_{xl} \\ \sum E_{yl} \\ \sum H_{xl} \end{bmatrix} = BC_l \begin{bmatrix} H_{l1} \\ H_{l2} \\ H_{l3} \\ H_{l4} \end{bmatrix}. \quad (4.31)$$

In equation (4.31)  $H_{l1} - H_{l4}$  are the amplitudes of the four partial fields that form the  $H_y$ . The explicit expressions for the BC matrix are provided as follows:

$$BC_l = \begin{bmatrix} A_{1,l} & A_{2,l} & A_{3,l} & A_{4,l} \\ 1 & 1 & 1 & 1 \\ B_{1,l} & B_{2,l} & B_{3,l} & B_{4,l} \\ C_{1,l} & C_{2,l} & C_{3,l} & C_{4,l} \end{bmatrix}, \quad (4.32)$$

$$A_{i,l} = \frac{k_z(i)}{\omega[\varepsilon_{xx} + \varepsilon_{xy} \left[ \frac{\beta_l \lambda_l}{\gamma_l \xi_l} - \frac{\alpha_l}{\gamma_l} \right] - \frac{\lambda_l}{\xi_l} \varepsilon_{xz}]}, \quad (4.33)$$

$$B_{i,l} = \left( \frac{\beta_l \lambda_l}{\gamma_l \xi_l} - \frac{\alpha_l}{\gamma_l} \right) A_{i,l}, \quad (4.34)$$

$$C_{i,l} = \frac{-k_z(i)}{\omega\mu} B_{i,l}. \quad (4.35)$$

The forward and backward propagation of the partial fields, inside the  $l_{th}$  layer, from the  $l_{th}$  interface, denoted by  $[H_{l1} H_{l2} H_{l3} H_{l4}]^T$  to, the  $(l+1)_{th}$  denoted by  $[H'_{l1} H'_{l2} H'_{l3} H'_{l4}]^T$ , is shown analytically as follows equation (4.36) and (4.37). where,  $d_l$  is the thickness of the layer and  $k_{z,l,i}$  is the z component of the wave vector in section II. In this paper,  $e^{-ik_{zi}}$  is the chosen as the sign convention for propagation in the +z direction,

$$\begin{bmatrix} H_{l1} \\ H_{l2} \\ H_{l3} \\ H_{l4} \end{bmatrix} = P_l \begin{bmatrix} H'_{l1} \\ H'_{l2} \\ H'_{l3} \\ H'_{l4} \end{bmatrix}, \quad (4.36)$$

$$P_l = \begin{bmatrix} e^{ik_{z,l,1}d_l} & 0 & 0 & 0 \\ 0 & e^{ik_{z,l,2}d_l} & 0 & 0 \\ 0 & 0 & e^{ik_{z,l,3}d_l} & 0 \\ 0 & 0 & 0 & e^{ik_{z,l,4}d_l} \end{bmatrix}. \quad (4.37)$$

According to figure 4.10, the transfer function  $T_l$  relates the tangential components of the E-field and H-field of the  $(l-1)_{th}$  layer to the  $(l+1)_{th}$  layer:

$$\begin{bmatrix} \sum H_{yl-1} \\ \sum E_{xl-1} \\ \sum E_{yl-1} \\ \sum H_{xl-1} \end{bmatrix} = T_l \begin{bmatrix} \sum H_{yl+1} \\ \sum E_{xl+1} \\ \sum E_{yl+1} \\ \sum H_{xl+1} \end{bmatrix}. \quad (4.38)$$

Furthermore, equations (4.36), (4.37), and (4.38), form the transfer function for the  $l_{th}$  layer in a layered system, based on the flowchart in figure 4.10, as follows

$$T_l = BC_l P_l B C_l^{-1}. \quad (4.39)$$

The ordered product of the layers' transfer functions from the first interface, at



$z=0$ , to the last interface, at  $z = z_n$ , relates the tangential field's components at  $z=0$  and  $z=z_n$ ,

$$T = \prod_{l=1}^N T_l. \quad (4.40)$$

The TF term in equation (4.30) is the relation between the amplitudes of the incident, reflected, and transmitted waves. In most of the cases the incident and exit media are isotropic and  $BC_l$  in equation (4.32) may be simplified to,

$$BC_0 = \begin{bmatrix} 1 & 1 & 0 & 0 \\ \frac{k_{z0}}{\omega\varepsilon_0} & -\frac{k_{z0}}{\omega\varepsilon_0} & 0 & 0 \\ 0 & 0 & 1 & 1 \\ 0 & 0 & \frac{k_{z0}}{\omega\mu_0} & -\frac{k_{z0}}{\omega\mu_0} \end{bmatrix}, \quad (4.41)$$

$$BC_N = \begin{bmatrix} 1 & 1 & 0 & 0 \\ \frac{k_{zN}}{\omega\varepsilon_N} & -\frac{k_{zN}}{\omega\varepsilon_N} & 0 & 0 \\ 0 & 0 & 1 & 1 \\ 0 & 0 & \frac{k_{zN}}{\omega\mu_N} & -\frac{k_{zN}}{\omega\mu_N} \end{bmatrix}. \quad (4.42)$$

Here  $k_{z0}$  and  $k_{zN}$  are the  $z$  components of the  $k$ - vector in the isotropic incident and exit media, respectively, which become imaginary for the incident evanescent waves. In a lossless medium,  $k_{z0}$  and  $k_{zN}$  are real for propagating waves and imaginary for evanescent waves.

#### 4.9 Imaging with Aligned Non-Spherical Nanoparticles

The prominent importance between the optical property of composite with randomly align non-spherical inclusions and composite with oriented non-spherical inclusion is anisotropy. An anisotropic slab with specific permittivity tensor is able to transmit the high spatial frequencies without major loss due to its

hyperbolic dispersion curve [22]. Assume an anisotropic slab with the following permittivity,

$$\bar{\bar{\epsilon}} = \begin{bmatrix} \epsilon_{xx} & 0 & 0 \\ 0 & \epsilon_{yy} & 0 \\ 0 & 0 & \epsilon_{zz} \end{bmatrix}. \quad (4.43)$$

The normal component of the propagation vector in the slab with above permittivity is,

$$k_{z,1} = -k_{z,2} = \sqrt{k_0^2 \epsilon_{xx} - \frac{\epsilon_{xx}}{\epsilon_{zz}} k_x^2}, \quad (4.44a)$$

$$k_{z,3} = -k_{z,4} = \sqrt{k_0^2 \epsilon_{yy} - k_x^2}. \quad (4.44b)$$

If the sign on real part of  $\epsilon_{xx}$  and  $\epsilon_{zz}$  are opposite, equation (4.44a) represents a hyperbola in the k space which means that for the values  $k_x$  of higher than  $k_0$ ,  $k_{z,1}$  stays real and the subwavelength details of the object which are carried by the high spatial frequencies,  $k_x$ , are preserved through the anisotropic layer and carried to the image plane, consequently the image at the image plane has subwavelength precision. It should be noted that the mechanism for subwavelength imaging with isotropic composite slab and anisotropic composite slab is different. Imaging with isotropic composite slab the evanescent waves are amplified consequently the overall thickness of composite layers and dielectric layers should be equal (Veselago ratio). This ratio is not required in with anisotropic slab since the evanescent waves are preserved not amplified. Consequently the dielectric spacing can be chosen as thin as possible to minimize the attenuation of the evanescent waves which result in higher resolution compared to only isotropic multilayer designs. The metal dielectric composite with aligned nanoparticle inclusions is

intriguing as the permittivity tensor can be engineered for optimum imaging by several controlling factors such as: shape and filling fraction of inclusions, dielectric constant of the host medium, and the frequency of the incident field.

In order to study the effect of inclusions' alignment, the dimensions of nanoparticles and slab thickness are set to the same values in table 4.1, which are the optimum values found for imaging with composites made of randomly oriented inclusions. The differential evolution algorithm then finds the optimum value for the filling fraction and frequency of incident light for the best possible image. In figure 4.12 imaging with isotropic composite and anisotropic composite which is formed by randomly oriented prolate and aligned prolate respectively is compared.

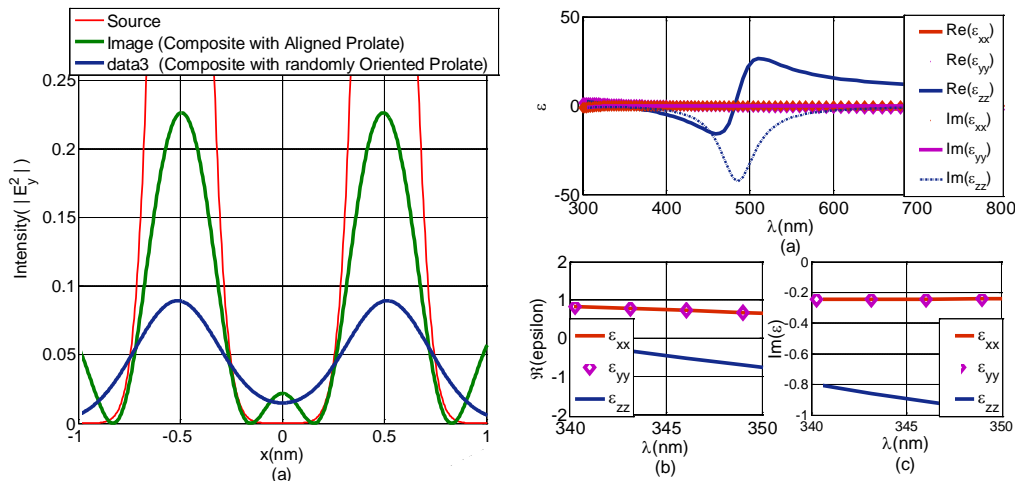


**Figure 4.12** (a) Subwavelength imaging with composite made of randomly oriented prolates and composite made of aligned prolates (b)Tensor of effective permittivity (c) Real part of permittivity tensor for the frequency that the imaging is realized (d) Imaginary part of permittivity tensor for the frequency that the imaging is realized

Interestingly it is observed that the anisotropic slab offers higher field intensity in the image plane and consequently better signal to noise ratio, owing to its different imaging mechanism. Figure 4.12 (b) presents the elements of effective permittivity

tensor and figure 4.12 (c) demonstrates the suitable frequencies where the sign of real parts of epsilon for two principal axes become opposite to the third one and the slab supports the hyperbolic dispersion.

The difference in the mechanism of imaging for isotropic and anisotropic slab lies in difference between their dispersion relations. The isotropic medium with permittivity  $\epsilon_{iso} = \epsilon_1 - i\epsilon_2$  owns the following dispersion,

$$k_{ziso} = \sqrt{k_0^2 \epsilon_1 - k_x^2 - ik_0^2 \epsilon_2}. \quad (4.45)$$

In addition to the waves with high tangential components, material loss also hampers imaging with high resolution. Regarding equation (4.44a) for the dispersion relation of anisotropic medium where  $\epsilon_{xx} = \epsilon_1 - i\epsilon_2$  and  $\epsilon_{zz} = -\epsilon_1 - i\epsilon_2$ ,

$$k_{zaniiso} = \sqrt{k_0^2 \epsilon_1 - \frac{\epsilon_2^2 - \epsilon_1^2}{\epsilon_2^2 + \epsilon_1^2} k_x^2 - i(k_0^2 \epsilon_2 + 2 \frac{\epsilon_1 \epsilon_2}{\epsilon_1^2 + \epsilon_2^2})} = \sqrt{A + iB}, \quad (46.a)$$

$$\sqrt{A + iB} = R e^{-i\theta}, \quad R = \sqrt{A^2 + B^2} \text{ \& } \theta = \tan^{-1}(B/A). \quad (46.b)$$

Depending on values for  $\epsilon_1$  and  $\epsilon_2$  the effective loss in equation (46.b) can be less than the loss in equation (4.45) which results in the higher tolerance of anisotropic slab for loss than isotropic slab. Imaging with aligned nano-disk inclusions shown in figure 4.13 agrees well with the higher tolerance of anisotropic slabs against the loss. Consequently the composite with aligned appropriated non-spherical inclusions is an intriguing option when signal to noise ratio in near field subwavelength imaging is a critical issue.

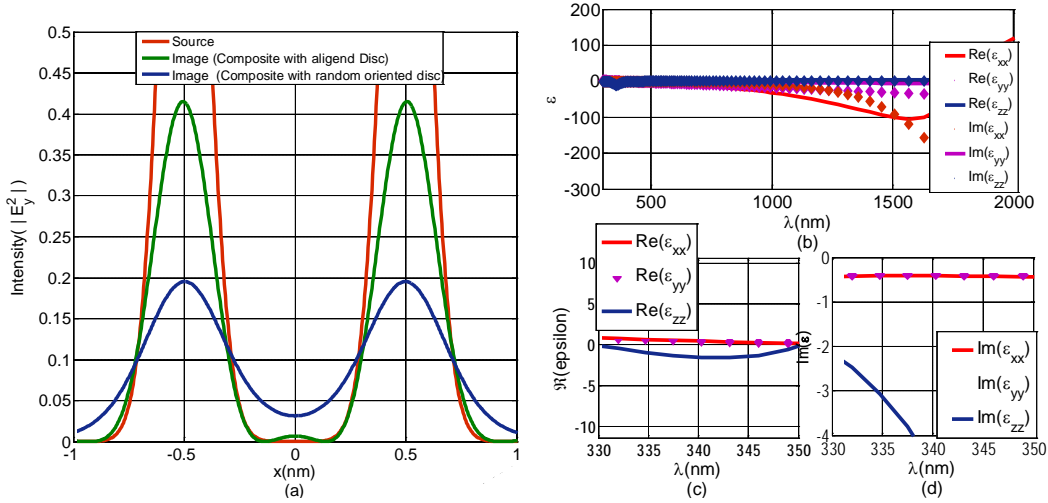


**Figure 4.13** (a) Subwavelength imaging with composite made of randomly oriented discs and composite made of aligned discs (b)Tensor of effective permittivity (c) Real part of permittivity tensor for the frequency that the imaging is realized (d) Imaginary part of permittivity tensor for the frequency that the imaging is realized

Table 4.3 summarizes the optimum filling fraction, frequency, and effective permittivity of anisotropic slabs in figure 4.12 and 4.13.

**Table 4.3** Optimized parameters for subwavelength imaging with single layer of composite made of aligned inclusions

Shape	Prolate	Ellipsoidal Disc	Geometry
Filling Fraction	.5	.5	<p><b>d</b></p>
Wavelength(nm)	349	334	
$\epsilon_{xxeff}$	$0.67 - i0.24$	$0.69 - i0.40$	
$\epsilon_{yyeff}$	$0.67 - i0.24$	$0.69 - i0.38$	
$\epsilon_{zzeff}$	$-0.7 - i0.9$	$-0.91 - i3$	
d (nm)	30	30	

In addition, the anisotropic slab offers higher cut-off spatial frequency than isotropic slab .The cut-off frequency is regarded to the frequency where  $k_z$

becomes imaginary and the propagating waves turn into evanescent waves. In other words, cut-off frequency is where the tangential component of the propagation vector exceeds the propagation constant of the medium which is  $k_0\sqrt{\epsilon_1}/2\pi$  for isotropic slab and  $\frac{\epsilon_2^2+\epsilon_1^2}{\epsilon_2^2-\epsilon_1^2}k_0\sqrt{\epsilon_1}/2\pi$  for anisotropic slab. As  $\frac{\epsilon_2^2-\epsilon_1^2}{\epsilon_2^2+\epsilon_1^2}$  factor in equation (4.46a) is always smaller than one, it scales down the tangential component of propagation vector; hence the cut-off happens for higher value of  $k_x$  which results in propagation of waves with bigger tangential components. Consequently it is expected that anisotropic slab would be capable to do subwavelength imaging for higher resolutions. This is demonstrated in figure 4.14 by reducing the spacing between two Gaussian pulses in the object plane by 40 nm, and compare the performance of composite made of aligned inclusions and composite made of randomly oriented inclusions.

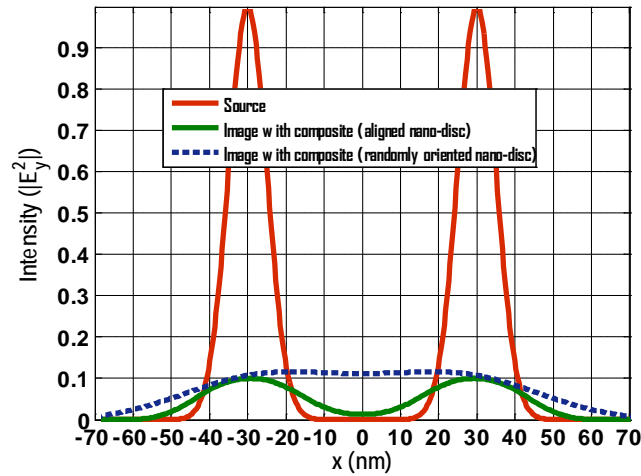


**Figure 4.14** The success of composite slab made of aligned inclusions in subwavelength imaging for higher resolution.

As it is presented in figure 4.14, while the composite with aligned nano-disc succeeds to transfer enough  $k$ -vectors with tangential components larger than  $k_0$ ,

the composite slab with randomly oriented nano-disc fails to form two distinguishable peaks in the image plane. The filling fraction, incident field's frequency are effective permittivities are taken from table 4.1 and 4.3.

#### **4.10 Conclusion**

In this chapter subwavelength imaging with single layer and multilayer composite slabs which are made of non-spherical plasmonic inclusions embedded in dielectric host medium is investigated. The shape, size, and orientation of nano particles offer high degree of freedom to realize subwavelength imaging according to the available laser sources. For composite made of randomly oriented non-spherical inclusions it is shown that the by increasing the eccentricity of nanoparticles the resonance peak of effective index of refraction is red shifted ;hence the different shapes of nanoparticle is beneficial to design an optical system which is compatible with available resources. An optimum values for filling fraction, incident field's frequency, and thickness are found for single layer and multi layer lensing system, provided in table 4.1 and 4.2, and subwavelength imaging for two Gaussian pulses spaced 100 nm is realized over the optical range with composite slabs made of inclusions with different non-spherical shapes such as general ellipsoids, oblates, prolates, disks and needles. As effective refraction index of a composite with aligned nano ellipsoid is anisotropic, a fully analytical algorithm is developed to investigate light interaction with arbitrary anisotropic layered structure. This algorithm is suitable to investigate the near-field/far-field electromagnetic wave interaction at any angle of incidence for numerous intriguing applications. It is shown that the

composite slab with aligned non-spherical inclusions is not only capable to realize the subwavelength imaging at different wavelengths but also it is more robust to the material loss due to its different mechanism of imaging. Consequently for two composite slabs with the same thickness, one formed from randomly oriented inclusions (isotropic) and the other formed by aligned inclusions (anisotropic) of same shape and same size, it is shown that the image formed in the image plane by anisotropic slab has higher intensity in comparison with image formed by isotropic slab, hence anisotropic slabs offer better signal to noise ratio in the image plane. Owing to its specific dispersion curve, it is also analytically shown that this anisotropic slab can preserve waves with higher tangential component of wave vector which result in higher resolution; it is demonstrated while composite with randomly oriented inclusions (isotropic) fails to resolve two Gaussian pulses spaced 60 nm, the composite with the same thickness made of aligned inclusion of same shape and size, successfully resolves the pulses in the image plane.



## References

- [1] Y. Kiasat, Z. Szabo, X.Chen, and E. P. Li," Light interaction with multilayer arbitrary layered anisotropic structure: an explicit analytical solution and application for sub\_wavelength imaging", Accepted in *J.Opt.Soc.Am B*, (2014).
- [2] A. H. Sihvola,". Electromagnetic mixing formulae and applications," No. 47. Iet, (1999).
- [3] E. A. Coronado, and G. C. Schatz. "Surface plasmon broadening for arbitrary shape nanoparticles: A geometrical probability approach." *J. of Chem. Phys.* 119 : 3926. (2003)
- [4] J. J. Mock, "Shape effects in plasmon resonance of individual colloidal silver nanoparticles." *J. of Chem.Phys.* 116 :6755,(2002).
- [5] Link, S., et al. "How long does it take to melt a gold nanorod?: A femtosecond pump-probe absorption spectroscopic study." *Chemical Physics Letters* 315.1: 12-18, (1999).
- [6] S. Link , and M. A. El-Sayed. "Spectroscopic determination of the melting energy of a gold nanorod." *J. of Chem. Phys.* 114 :2362,(2001).
- [7] R. Jin, "Photoinduced conversion of silver nanospheres to nanoprisms." *Science* 294.5548 1901-1903,(2001).
- [8] J. Diener, D. I. Kovalev, N. Kuenzner, , E. Gross, G. Polisski, F. Koch, M. Fujii, "Spatially nanostructured silicon for optical applications," *In Proceeding of Sixth International Conference on Material Science and Material Properties for Infrared Optoelectronics*, 12-22 ( 2003).
- [9] Q. D. Nguyen, "Electrochemistry in anisotropic etching of silicon in alkaline solutions: a kinetic wave analysis," UT publication (2007).
- [10] H. W. Park, T. Kim, J. Huh, M. Kang, J. E. Lee, H. Yoon, "Anisotropic Growth Control of Polyaniline Nanostructures and Their Morphology-Dependent Electrochemical Characteristics," *ACS Nano*,6,7624-7633 (2012).
- [11] Y. Hanazaki, J. Masumoto, S. Sato, K. Furusawa, A. Fukui, ,N. Sasaki, "Multiscale analysis of changes in an anisotropic collagen gel structure by culturing osteoblasts," *ACS Applied Materials & Interfaces* (2013).

- [12] K. D. Costa, E. J. Lee, J. W. Holmes, "Creating alignment and anisotropy in engineered heart tissue: role of boundary conditions in a model three-dimensional culture system," *Tissue Eng.* 567-77 (2003).
- [13] A. N. Parikh, D. L. Allara, "Quantitative determination of molecular structure in multilayered thin films of biaxial and lower symmetry from photon spectroscopies. I. Reflection infrared vibration spectroscopy," *J. of chem. phys.*, 96 (1992)
- [14] J. Schesser, G. Eichmann, "Propagation of plane waves in biaxially anisotropic layered media," *J. Opt. Soc. Am* 62, 786-791 (1972).
- [15] J. J. Stamnes, G. C. Sherman, "Reflection and refraction of an arbitrary wave at a plane interface separating two uniaxial crystals," *J. Opt. Soc. Am.* 67, 683-695, (1977).
- [16] J. Stamnes, G. S. Sithambaranathan, "Reflection and refraction of an arbitrary electromagnetic wave at a plane interface separating anisotropic and a biaxial medium," *J. Opt. Soc. Am. A* 22, 3119-3129 (2001).
- [17] R. A. Farrell, D. Rouseff, R. L. McCally, "Propagation of polarized light through two- and three-layer anisotropic stacks," *J. Opt. Soc. Am. A*, 22, 1981-1992 (2005).
- [19] P. Yeh, "Electromagnetic propagation in birefringent layered media," *J. Opt. Soc. Am.* 69, 742-755 (1979).
- [19] D. W. Berreman, "Optics in Stratified and Anisotropic Media:  $4 \times 4$ -Matrix Formulation," *J. Opt. Soc. Am.* 62, 502-510 (1972)
- [20] M. Schubert, "Polarization-dependent optical parameters of arbitrarily anisotropic homogeneous layered systems," *Phys. Rev. B* 53, 4265-4274 (1996)
- [21] N. Ouchani, D. Bria, B. Djafari-Rouhani, A. Nougouei, "Transverse-electric/transverse-magnetic polarization converter using finite biaxial photonic crystal," *J. Opt. Soc. Am* 24, 2710-2718 (2007).
- [22] M. Sluijter, D.K. de Boer, J.J. Braat, "General polarized ray-tracing method for inhomogeneous uniaxially anisotropic media," *J. Opt. Soc. Am. A* 25, 1260-1273 (2008).
- [23] P. Ginzburg, F. J. Fortuño, G. A. Wurtz, W. Dickson, "Manipulating polarization of light with ultrathin epsilon-near-zero metamaterials," *Optics Express*, Vol. 21, 14907-14917 (2013).

- [24] D. Mounier, P. Picart, P. Babilotte, P. Ruello, "Jones matrix formalism for the theory of picosecond shear acoustic pulse detection, *Optics Express*, Vol. 18, 6767-6778, (2010)
- [25] D. Sun, J. Rioux, J. E. Sipe, Y. Zou, M. T. Mihnev, C. Berger, T. B. Norris, "Evidence for interlayer electronic coupling in multilayer epitaxial graphene from polarization-dependent coherently controlled photocurrent generation," *Phys.Rev.* 16, Vol. B85 (2012).
- [26] I. V. Lindell, F. Olyslager, "Generalized decomposition of electromagnetic media," *Ant. and propag. IEE*, 46 (1998).
- [27] E. Langereis, S. B. S. Heil, H. C. M. Knoop, W. Keuning, M. C. M. Van de Sanden, W. M. M. Kessels, "In situ spectroscopic ellipsometry as a versatile tool for studying atomic layer deposition," *J. of Phys. D*, Vol 42, 073001 (2009).
- [28] A. Salandrino, N. Engheta, "Far-field subdiffraction optical microscopy using metamaterial crystals: Theory and simulations," *Phys.Rev. B* 7, Vol.74, 075103 (2006)
- [29] H. Liu, K. J. Webb, "Sub-wavelength imaging opportunities with planar uniaxial anisotropic lenses", *Optics Letters*, Vol. 33, Issue 21, 2568-2570 (2008).
- [30] Liu, Huikan, and Kevin J. Webb. " Subwavelength imaging opportunities with planar uniaxial anisotropic lenses." *Optics letters* 33.21 (2008): 2568-2570.
- [31] Fang, Nicholas, et al. "Sub-diffraction-limited optical imaging with a silver superlens." *Science* 308.5721: 534-537 (2005).
- [32] Price, Kenneth V., Rainer M. Storn, and Jouni A. Lampinen. " Differential evolution a practical approach to global optimization." (2005).

## CHAPTER 5

# THE MECHANISM OF MAGNIFIED VIRTUAL IMAGE FORMATION IN NEAR FIELD WITH MICROSCOPE NANOSCOPE

### 5.1 Introduction

The subwavelength imaging technique that has been discussed so far is confined to near-field imaging due to the flat structure and smooth surface of the lens. Far-field super lens (FSL) used a silver slab to enhance the evanescent waves and used an attached line grating to convert the evanescent waves into the propagating waves. However, such a FSL did not magnify objects. In order to produce a magnifying superlens Smolyaninov *et al.* [1] suggested the use of two-dimensional surface plasmon Polariton (SPP) confined by a concentric polymer grating placed on a gold surface. It generates 3x magnifications and a resolution of 70 nm at 495-nm wavelength ( $\lambda / 7$  far-field resolution). Hyperlens is another type of magnifying superlens. The hyperlens used an anisotropic medium with a hyperbolic dispersion that generates a magnification effect through the cylindrical curved multilayer stacks [2]. Due to the SPP energy loss and sophisticated nano-

fabrication process, the resolutions of existing SPP-superlens and hyperlens are limited within  $\lambda/7$  to  $\lambda/3$ . Moreover, both magnification and resolution of these lenses are orientation-dependant, which implies that the final images are not isotropic within the imaging plane. The other practical limit is that the SPP-superlenses must be excited with a specific laser source and configuration (wavelength, polarization, incident angle). The latter shortcoming is alleviated by the introduction of metal-dielectric composite discussed in previous chapters; however it is hard to achieve SPP-superlens function with a standard white light source.

Subwavelength dielectric structures offer an attractive low-loss alternative to plasmonic material for the development of resonant optics functionalities. It is shown that a single microsphere illuminated by a tightly focused Gaussian beam is capable of subwavelength light confinement and significantly enhances the fluorescence emission from a single molecule. In that case, strong confinement of light, on the order of  $6(\lambda/n)^3$ , with a non-resonant dielectric structure was clearly demonstrated [3]. The nanoscale solid immersion lenses (nSILs) have been recently fabricated using sophisticated techniques for subwavelength imaging [4]. It is reported to resolve 220 nm line objects at 475 nm imaging wavelength ( $\lambda/2.2$  far-field resolution,  $\times 2$  magnification) [5]. Compared with macroscopic SILs, wavelength-scale nSILs can produce a 25% smaller focus spot, which enhances the resolution [4]. Due to the shortage of high-index lens materials it remains practically impossible for SILs to resolve nano-objects below 100 nm with visible light sources [4, 5].

Recently a breakthrough 50-nm-resolution optical nanoscope is reported that uses ordinary glass microspheres ( $n = 1.46$ ,  $2 \mu\text{m} < \text{diameter} < 9 \mu\text{m}$ ) as far-field superlens [6]. It is experimentally demonstrated that nanoscope can overcome the white-light diffraction limit, and attain resolution between  $\lambda / 8$  and  $\lambda / 14$  and a magnification between  $\times 4$  and  $\times 8$ . Although the idea of the object magnification with spherical particles was discussed previously [7], it was not clear up to which extend one can produce magnification and what is the mechanism of the image formation. To our best knowledge, the near field virtual image formation and magnification mechanism which reveals the ultimate achievable subwavelength resolution is not discussed so far. In this chapter a novel methodology based on rigorous multipole expansion is developed to unveil the mechanism of subwavelength imaging with microscope nanoscope for the first time.

## **5.2 Near Field Optics, Microscopic vs. Mesoscopic**

Generally, a near-field region is referred to a region with size in nanoscopic or mesoscopic scales. The mesoscopic scale is referred to the situations where the sizes are in the order of the incident wavelength  $\lambda$ . In the visible light region this scale corresponds roughly to the length range from  $0.1 \mu\text{m}$  to  $1 \mu\text{m}$ . By nanoscopic, one usually means low-dimensional structures smaller than  $100 \text{ nm}$  [8]. If these structures can be identified with single molecules, the nanoscopic regime also means the molecular range. However, structures smaller than  $1 \text{ nm}$  are commonly viewed as belonging to the atomic range.

When  $\lambda$  is much smaller than the size of the scatterers, one speaks of the macroscopic regime. Geometrical optics is a first-order approximation which describes the scattering of light by macroscopic objects. On a more refined level, Kirchhoff's diffraction theory uses a scalar field to account for phenomena where light displays a wave character on a macroscopic scale. Kirchhoff's theory attributes ideal properties to the scatterers such as a perfect conductivity or a real refractive index.

Microscopic systems are objects which are so small when compared to the incident wavelength that the non-retarded approximation becomes applicable. This approximation considers the scatterers as dipoles or a set of dipoles whose susceptibilities may include dissipative effects. For visible wavelengths, this regime corresponds to the atomic range. Near-field optics deals with phenomena involving evanescent electromagnetic waves that become significant when the sizes of the objects are in the order of  $\lambda$  or even smaller [8].

In view of the above classification, it is clear that near-field optics is thus concerned with the scattering of electromagnetic waves by mesoscopic and nanoscopic systems. Even in the situations where atomic size structure is involved, near-field optical detection is affected by the nano- and mesoscopic systems embedding the atomic size structure. Evanescent waves are important in near-field optics because the typical size of the objects is comparable to  $\lambda$  and the decay of evanescent waves occurs within a range given by the wavelength  $\lambda$  and the angle of incidence [8].

### 5.3 Optical Resonance and Near-Field Enhancement Effects

The first analysis of the optical resonance was done with respect to conventional applications in colloid and aerosol physics. According to Diao *et al.* [9], the optical resonance of a dielectric sphere is caused by sphere cavity resonance (SCR). In SCR, the incident field excites resonant but undamped modes in dielectric spheres which are distributed as evanescent waves around the sphere. In the near-field region of the sphere cavity, the field distribution is dominant with these evanescent waves, and is sensitive to the size parameter of the sphere. The SCR resonances are very sharp, and the efficient divergence of radiation for corresponding modes is very small. It means that optical resonances produce high intensities in the near-field region and, naturally, it can lead to formation of “hot spots”. Figure 5.1 demonstrates the COMSOL simulation of the formation of hot spot by a dielectric nanosphere.

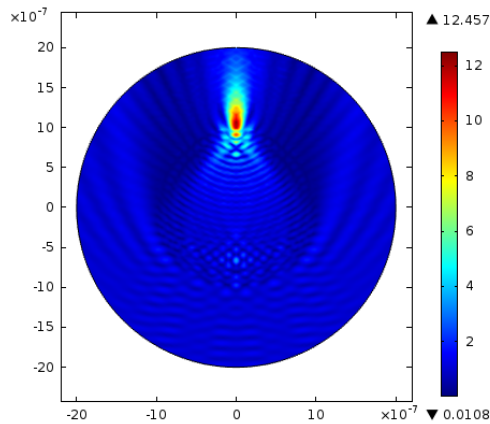


**Figure 5.1** Subwavelength focusing of light by dielectric nanosphere

$$\epsilon_r = 2.56 \quad a = 200 \text{ nm} \quad \text{at} \quad \lambda = 248 \text{ nm}$$

However it should be noted that the focusing capability of dielectric sphere depends critically on two factors, the size parameter of the sphere defined



as  $q = 2\pi a/\lambda$  and the refractive index of the sphere. In modeling, SCR can be described by Mie theory. This is an exact solution to Maxwell equation for an arbitrary sphere under plane wave excitation. The geometrical optics (for big particle with  $\lambda \gg a$ ) and dipole approximation (for small particle with  $\lambda \ll a$ ) can be regarded as the two limiting cases of Mie theory. In near field optics (NFO) where mesoscopic size particles are concerned, the simulation by dipole approximation could lead to inaccurate results due to the excitation of higher-order multipole resonance modes in particles. It needs careful and theoretical analysis with sufficient number of mode terms. The inclusion of a small term in Mie series beyond dipole approximation could significantly distort the phase portrait of optical near-field and produce a completely different near-field distribution.

#### **5.4 Theoretical Challenge for Light Interaction with Mesoscopic Structures**

The theory of electromagnetic waves describes satisfactorily their interaction with objects which are macroscopic or microscopic relative to the incident wavelength. However, the theoretical knowledge about the scattering of electromagnetic waves by mesoscopic systems remains limited. Since many situations involve nanoscopic and mesoscopic systems simultaneously, incomplete information about the mesoscopic range impedes our understanding of nanoscopic systems. Most approximations are not appropriate for studying mesoscopic systems. Unlike macroscopic systems (successfully described by Kirchhoff theory) and

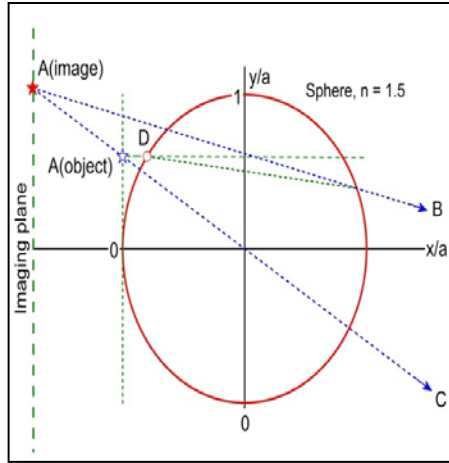
microscopic systems (for which retardation is negligible), mesoscopic systems require the detailed solution of the full set of Maxwell equations. Again, the main origin of their problems can be traced to the crucial role played by the evanescent components of the field in the near-field zone close to mesoscopic scatterers. In the mesoscopic range, the accurate treatment of evanescent waves requires one to deal carefully with the electromagnetic boundary conditions at each interface. To ensure the accuracy of simulation results, exact models are used in this chapter.

## **5.5 Formulation of the Problem and Methodology**

When the size of the particle is much bigger than  $\lambda$ , the magnification effect can be illustrated with the help of geometrical optics. The virtual image of a small object for this case is magnified by a factor of  $n / (2 - n)$  for  $1 < n < 2$ . Naturally for a sub-diffraction object in the near field, the geometrical optics is not applicable and one should solve Maxwell equations. However, as a reciprocal effect to the Mie theory, one can expect that an object with size in the order of at least  $\lambda / 8$  can be converted into image with a size  $\lambda$ , which can be seen by a conventional optical microscope [10]. In other words if a dielectric nano- or microparticle is capable to form a subwavelength size “hot spot”, reciprocally it can magnify an object of subwavelength size up to a dimension beyond the diffraction limit. An analogy to this phenomenon in geometrical optics, with different mechanism, is magnified virtual image of an object with magnifying glass lenses, figure 5.2. The magnified virtual near-field image formation by dielectric microsphere is demonstrated experimentally in [6]. The schematic of the experiment is shown in figure 5.3.



(a)



(b)

**Figure 5.2** Magnified Virtual Image Formation (a) Virtual image forms by glass lens (b) Ray tracing technique to determine virtual image formation in geometrical optics[16]

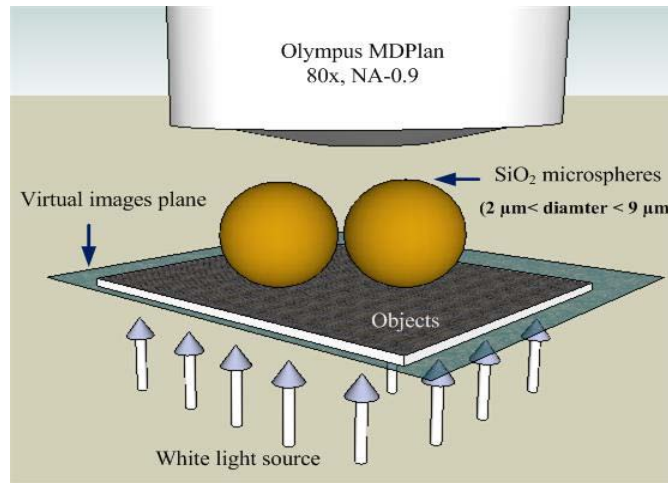


**Figure 5.3** Experimental configuration of white-light microsphere nanoscope with  $\lambda/8 - \lambda/14$  imaging resolution. Schematic of the transmission mode microsphere superlens integrated with a classical optical microscope. The spheres collect the near-field object information and form virtual images that can be captured by the conventional lens, reprinted with permission of [6].

In figure 5.3, the microspheres are placed on the top of the object surface by self-assembly. A halogen lamp with a peak wavelength of  $600 \text{ nm}$  is used as the white-light illumination source. The microsphere superlenses collect the

underlying near-field object information, magnify it (forming virtual images which keep the same orientation as the objects in the far-field) and pick it up by a conventional  $\times 80$  objective lens [6].

In order to explain the mechanism of virtual image formation in near-field and to evaluate the capability of the microsphere in far-field subwavelength imaging within the white light source, the following configuration in figure 5.4 is analytically investigated.

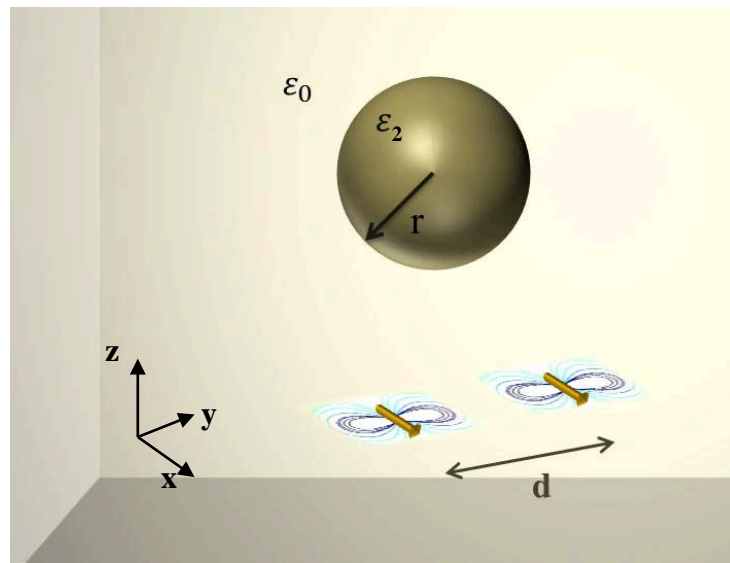


**Figure 5.4** Analytical investigation of virtual image formation in the near-field with the system of two radiating dipole and dielectric microsphere. The dielectric microsphere operates as a superlens to create magnified virtual image of two dipoles.

The two Hertzian dipoles are located in nanometric distance below the dielectric sphere with permittivity  $\epsilon_2$ . The spacing between the dipoles,  $d$ , is set to be subwavelength to represent an object with subwavelength feature. The field radiated by two dipoles is enhanced by microsphere; for the appropriate size

parameter and permittivity of the sphere, it is expected to observe the magnified virtual image in the image plane which is placed in the near-field of dipoles.

The analytical investigation procedure consists the following major steps:

- Expansion of electric field and magnetic field of arbitrarily located and polarized Hertzian dipole in the spherical coordinate.

The subwavelength focus shown in figure 5.1 is due to the field that is scattered by sphere. Consequently, to calculate the scattered field by the sphere the incident field should be represented in the coordinate consistent with the geometry of the boundary of the sphere. This step of the analysis is in fact the most rigorous part of the problem. Since the scattering problem is a linear system, the achieved exact solution in this step, can be applied for any arbitrarily located and polarized collection of dipoles, i.e. two dipoles with subwavelength spacing.

- Calculation of the scattering coefficients for the scattered field.

The point of interest in this problem is the behavior of the field scattered by sphere and the contribution of the scattered field in the virtual image formation in near-field.

- Reconstruction of virtual image, using the reciprocity principle and extrapolation of timed averaged Poynting vector.

In cases of macroscopic spheres, in which geometrical optics applies, the virtual image magnification factor can be calculated through ray tracing, however as sphere size reduces to the mesoscopic and nanoscopic sizes, geometrical ray tracing becomes invalid; the optical rays going through

such small spheres could form optical vortices and singularities inside the sphere [6]. In fact in such regimes the light's ray no longer propagates along the straight line, hence the rays are not useful for ray tracing.

### 5.5.1 Rigorous Multipole Expansion

In this section the electromagnetic field of radiating dipole is derived analytically for a dipole with arbitrary location and polarization. In the cases of no free charges and currents, the electric and magnetic fields inside and outside the sphere both satisfy the vector Helmholtz equation [11].

$$(\nabla^2 + k^2)\mathbf{E} = 0, (\nabla^2 + k^2)\mathbf{H} = 0, \quad (5.1)$$

where  $k = \frac{\omega}{c}\sqrt{\epsilon}$  is the wave vector and  $\nabla^2$  is the Laplacian. The magnetic field can be expressed as a curl of auxiliary vector potential,  $\mathbf{A}$ , which simplifies the vector wave equation to the following differential equation for  $\mathbf{A}$ ,

$$(\nabla^2 + k^2)\mathbf{A} = 0. \quad (5.2)$$

The wave equation should be solved in spherical coordinate due to the spherical geometry of the problem. The magnetic vector potential,  $\vec{A}_{dip}$ , of a dipole at the coordinate  $\vec{r}$  due to an oscillating dipole at  $\vec{r}'$  with dipole moment  $\vec{p}$  is

$$\vec{A}_{dip} = -ik\vec{p} \frac{e^{ik|\vec{r}-\vec{r}'|}}{|\vec{r}-\vec{r}'|}, \quad (5.3)$$

According to the addition theorem the spherical expansion the of the vector potential, when  $r < r'$ , is [11],

$$\vec{A}_{dip} = 4\pi^2 \vec{p} \sum_l \sum_{m=-l}^l j_l(kr) h_l^{(1)}(kr') Y_{l,m}^*(\hat{r}') Y_{l,m}(\hat{r}), \quad (5.4)$$

where  $j_l$  and  $h_l^{(1)}$  are spherical Bessel function of first kind and spherical Hankel function of first kind, respectively, and  $Y_{l,m}$  is the spherical harmonics function of degree  $l$  and order  $m$ [12],

$$Y_{l,m} = (-1)^m \sqrt{\frac{2l+1}{4\pi} \frac{(l-m)!}{(l+m)!}} P_l^m(\cos\theta) e^{im\varphi}, \quad (5.5)$$

$P_l^m(\cos\theta)$  is associated Legendre function. The magnetic field ( $\vec{B}_{dip} = \nabla \times \vec{A}_{dip}$ ) of dipole is:

$$\begin{aligned} \vec{B}_{dip} = & (4\pi k^3 \sum_{l,m} j'_l(kr) h_l^{(1)}(kr') \hat{r} \times \vec{p} Y_{lm}^*(r) \\ & + \frac{4\pi i k^2}{r} \sum_{l,m} j_1(kr) h_l^{(1)}(kr') Y_{l,m}^*(r) [\hat{r} \times \vec{L} Y_{l,m}(r) \times \vec{p}]), \end{aligned} \quad (5.6)$$

where  $\vec{L} = -i\vec{r} \times \nabla$ , which is angular momentum operator. For more systematic calculation the magnetic field is decomposed to two components with multipole expansion technique.

$$\begin{aligned} \vec{B}_{dip} = & \sum_{l,m} \{ a_E(l,m) j_l(kr') \vec{Y}_{lm}(r) \\ & - (ic/\omega) a_M(l,m) \nabla \times [j_l(kr) \vec{Y}_{lm}(r)] \}, \end{aligned} \quad (5.7)$$

$\vec{Y}_{lm}(r)$  is vector spherical harmonics,

$$\vec{Y}_{lm}(r) = \frac{1}{\sqrt{l(l+1)}} \vec{L} Y_{m,l}, \quad (5.8)$$

$a_E$  and  $a_M$  are the coefficients dependant on the position and orientation of the dipole and are derived using orthogonal properties of spherical harmonics.

For instance  $a_E$  is calculated in the following procedure:

$$a_E(l', m') j_l(kr) = \int \vec{Y}_{l'l'm'}^*(\hat{r}) \cdot \vec{B}_{dip} d\Omega, \quad (5.9)$$

Substituting equation (5.8) in equation (5.9), the left side of equation (5.9) is:

$$\begin{aligned} & \frac{4\pi i k^2}{r} \vec{p} \cdot (-i \sum_{l,m} k r j'_1(kr) h_l^{(1)}(kr') Y_{lm}^* \int \vec{Y}_{l'l'm'}^*(r) \times \\ & [\hat{r} Y_{lm}(\hat{r})] d\Omega \quad (5.10) \quad - \\ & - \sum [l(l+1)]^{1/2} j_1(kr) h_l^{(1)}(kr') Y_{lm}^* \int \hat{r} [\vec{Y}_{l'l'm'}^*(r) \cdot \vec{Y}_{l'l'm'}(r)] d\Omega, \end{aligned}$$

The following property transforms spherical harmonics to vector spherical harmonics [12]

$$\hat{r} Y_{lm}(\hat{r}) = -\left(\frac{l+1}{2l+1}\right)^{1/2} \vec{Y}_{l,l+1,m}(\hat{r}) + \left(\frac{l}{2l+1}\right)^{1/2} \vec{Y}_{l,l-1,m}(\hat{r}), \quad (5.11)$$

The relation between spherical harmonics and vector spherical harmonics in equation (5-11) reduces the integral in equation (5- 10) to a sum of integrals of cross products of vector spherical harmonics. Then the following relation is used to simplify the integration calculation [13]

$$\vec{Y}_{JLM}(\theta, \varphi) = \sum Y_{lm}(\theta, \varphi) e_q \langle l m 1 q | l 1 J M \rangle, \quad (5.12)$$

$$\begin{cases} e_{+1} = -\frac{1}{\sqrt{2}}(\hat{x} + i\hat{y}) & q = 1 \\ e_0 = \hat{z} & q = 0 \\ e_{-1} = \frac{1}{\sqrt{2}}(\hat{x} - i\hat{y}) & q = -1 \end{cases} \quad (5.13)$$



where  $\langle l m 1 q | l 1 J M \rangle$  is Clebsch-Gordan coefficient [13].  $a_E$  and  $a_M$  are derived applying orthogonal property of spherical harmonics

$$a_E(l, m) = \frac{2\pi i k^3}{[l(l+1)(2l+1)]^{1/2}} \vec{p} \cdot \left( \frac{(l+1)h_l(kr')}{[2l-1]^{1/2}} \vec{e}^- + \frac{(l+1)h_{l+1}(kr')}{[2l+3]^{1/2}} \vec{e}^+ \right), \quad (5.14)$$

where,

$$\epsilon_{\bar{x}} = [(l+m)(l+m-1)]^{1/2} Y_{l-1, m-1}^*(r') - [(l-m)(l-m-1)]^{1/2} Y_{l-1, m+1}^*(r'), \quad (5.15.a)$$

$$\epsilon_{\bar{y}} = -i\{[(l+m)(l+m-1)]^{1/2} Y_{l-1, m-1}^*(r') - [(l-m)(l-m-1)]^{1/2} Y_{l-1, m+1}^*(r')\} \quad (5.15.b)$$

$$\epsilon_{\bar{z}} = -2[(l+m)(l-m)]^{1/2} Y_{l-1, m}^*(r'), \quad (5.15.c)$$

$$\begin{aligned} \epsilon_x^+ &= [(l+m+1)(l+m+2)]^{1/2} Y_{l+1, m+1}^*(r') \\ &\quad - [(l-m+1)(l-m+2)]^{1/2} Y_{l+1, m-1}^*(r'), \end{aligned} \quad (5.15.d)$$

$$\begin{aligned} \epsilon_y^+ &= i\{[(l+m+1)(l+m+2)]^{1/2} Y_{l+1, m+1}^*(r')\} \\ &\quad - i[(l-m+1)(l-m+2)]^{1/2} Y_{l+1, m-1}^*(r'), \end{aligned} \quad (5.15.e)$$

$$\epsilon_z^+ = -2[(l+m+1)(l-m+1)]^{1/2} Y_{l+1, m}^*(r'), \quad (5.15.f)$$

$$a_M(l, m) = \frac{2\pi i (k^2 \omega / c) h_l(kr') \vec{p} \cdot \vec{M}}{[l(l+1)]^{1/2}}, \quad (5.16)$$

where

$$\begin{aligned} M_x &= [(l-m)(l+m+1)]^{1/2} Y_{l, m+1}^*(r') \\ &\quad + [(l+m)(l-m+1)]^{1/2} Y_{l, m-1}^*(r'), \end{aligned} \quad (5.17.a)$$

$$\begin{aligned} M_y &= i[(l-m)(l+m+1)]^{1/2} Y_{l, m+1}^*(r') \\ &\quad - i[(l+m)(l-m+1)]^{1/2} Y_{l, m-1}^*(r'), \end{aligned} \quad (5.17.b)$$

$$M_z = 2m Y_{l, m+1}^*(r'), \quad (5.17.c)$$

The analytical expressions derived in equation (5.15) – (5.17) along with equation (5.7) enable one to find the explicit expression for electric field and magnetic field of arbitrarily polarized radiating dipole located in any point in the space.

### 5.5.2 Scattered Field

The scattered field is connected to the incident field on the boundary of the scatterer. The scattered field is found by following the same well elaborated scheme in Mie theory [14]. When E-fields and H-fields are described with scalar potential,  ${}^e\pi$  and  ${}^m\pi$ , the solution of the wave equation in spherical coordinate can be decomposed to three independent ordinary differential equation as function of  $r, \theta,$  and  $\varphi$  respectively. The differential equations are solved with undetermined coefficient and the coefficients are found by using the boundary conditions. According to [14] it is sufficient to calculate the radial component of E-field and H-field in order to derive the scalar potentials  ${}^e\pi$  and  ${}^m\pi$ . The angular components of E-field and H-field are derived from  ${}^e\pi$  and  ${}^m\pi$ . Hence to derive  ${}^m\pi$  the radial component of H-field is required. The first term in equation (5.7) includes only the angular component, consequently the second term is calculated first to determine the radial component. After few steps of calculation and taking to account that  $r^2\nabla^2 Y_{m,l} = -l(l+1)Y_{m,l}$  the radial component of H- field is

$$H_{dipole}^r = \frac{1}{k^2} \sum_{l,m} \frac{ck\sqrt{l(l+1)}}{\omega} a_M(l, m) \frac{\psi_l(kr)}{r^2} Y_{m,l}, \quad (5.18) \quad \psi_l(kr)$$

is Ricatti-Bessel function and defined as  $\frac{J_l(kr)}{kr}$ . The magnetic scalar potential,  ${}^m\pi$ , is calculated based on the following differential equation,

$$H_r = k^2 r^m \pi + \frac{\partial^2(r^m \pi)}{\partial r^2}. \quad (5.19)$$

Based on the expression for the H-field in equation (5.18), the trial solution for  $r^m \pi$  is

$$r^m \pi = \frac{1}{k^2} \sum_{l,m} \alpha_{l,m} j_l(kr) Y_{m,l}. \quad (5.20)$$

Equation (5.20) is substitute to equation (5.19), and we have

$$\alpha_{l,m} \left[ k^2 j_l(kr) + \frac{\partial^2(j_l(kr))}{\partial r^2} \right] = \frac{ck\mu\sqrt{l(l+1)}}{\omega} a_M(l, m) \frac{\psi_l(kr)}{r^2}. \quad (5.21)$$

By simple rearrangement equation (5.21) gets the familiar following form,

$$\frac{d^2(\psi_l)}{dr^2} + \left( k^2 - \frac{\alpha}{r^2} \right) \psi_l = 0. \quad (5.22)$$

The solution to this differential equation is Ricatti-Bessel function if  $\alpha = l(l+1)$ , consequently the unknown coefficient of equation (5-21) is,

$$\alpha_{l,m} = \frac{ck}{\omega\sqrt{l(l+1)}} a_M(l, m). \quad (5.23)$$

The scalar potential  ${}^e\pi$  is determined with the same procedure; the trial solution takes the form of

$$r^e \pi = \sum_{l,m} \beta_{l,m} j_l(kr) Y_{m,l}, \quad (5.24)$$

$$E_r = k^2 r e\pi + \frac{\partial^2(r e\pi)}{\partial r^2}. \quad (5.25)$$

Since  $\nabla \times \vec{H}_{dip} = -i \frac{\omega \varepsilon}{c} \vec{E}_{dip}$ , the radial component of E field :

$$E_{dipole}^r = i \frac{c}{\omega \varepsilon} \frac{1}{r^2 \sin \theta} \left\{ \frac{\partial(r H_\varphi \sin \theta)}{\partial \theta} - \frac{\partial(r H_\theta)}{\partial \varphi} \right\}. \quad (5.26)$$

After several steps of calculation the radial component of E field is

$$E_{dipole}^r = \frac{1}{k^2} \sum_{l,m} -\frac{\sqrt{l(l+1)}}{\sqrt{\varepsilon}} a_E(l, m) \frac{\psi_l(kr)}{r^2} Y_{m,l}, \quad (5.27)$$

$$\beta_{l,m} = -\sqrt{\frac{l(l+1)}{\varepsilon}} a_E(l, m). \quad (5.28)$$

The explicit expressions are found for scalar potentials of the fields of a dipole

$$r e\pi = \frac{1}{k_1^2} \sum_{l,m} \frac{-1}{\sqrt{\varepsilon l(l+1)}} a_E(l, m) \psi_l(kr) Y_{m,l}, \quad (5.29)$$

$$r^m \pi = \frac{c}{\omega k_1} \sum_{l,m} \frac{1}{\sqrt{l(l+1)}} a_M(l, m) \psi_l(kr) Y_{m,l}. \quad (5.30)$$

The complete solution of fields are derived from the scalar potentials,

$$E_r = k^2 r e\pi + \frac{\partial^2(r e\pi)}{\partial r^2}, \quad H_r = k^2 r^m \pi + \frac{\partial^2(r^m \pi)}{\partial r^2} \quad (5.31.a)$$

$$E_\theta = \frac{1}{r} \frac{\partial^2(r e\pi)}{\partial r \partial \theta} + \frac{i\omega\mu}{c} \frac{1}{r \sin \theta} \frac{\partial(r^m \pi)}{\partial \varphi}, \quad H_\theta = \frac{1}{r} \frac{\partial^2(r^m \pi)}{\partial r \partial \theta} - \frac{i\omega\varepsilon}{c} \frac{1}{r \sin \theta} \frac{\partial(r e\pi)}{\partial \varphi} \quad (5.31.b)$$

$$E_\varphi = \frac{1}{r \sin \theta} \frac{\partial^2(r e\pi)}{\partial r \partial \varphi} - \frac{i\omega\mu}{c} \frac{1}{r} \frac{\partial(r^m \pi)}{\partial \theta}, \quad H_\varphi = \frac{1}{r \sin \theta} \frac{\partial^2(r^m \pi)}{\partial r \partial \varphi} + \frac{i\omega\varepsilon}{c} \frac{1}{r} \frac{\partial(r e\pi)}{\partial \theta}. \quad (5.31.c)$$

The boundary condition imposes the continuity of the tangential components of E-field and H-field over the surface of the scatterer which is sphere in this problem. It is evidently sufficient that four quantities

$$\frac{\omega\varepsilon}{c}(r^e\pi), \quad \frac{\omega\mu}{c}(r^m\pi), \quad \frac{\partial(r^m\pi)}{\partial r}, \quad \frac{\partial(r^e\pi)}{\partial r}, \quad (5.32)$$

also be continuous over the surface

$$\frac{\partial}{\partial r}\{r(e\pi^{(i)} + e\pi^{(s)})\}_{r=a} = \frac{\partial}{\partial r}\{r(e\pi^{(w)})\}_{r=a}, \quad (5.33.a)$$

$$\frac{\partial}{\partial r}\{r(m\pi^{(i)} + m\pi^{(s)})\}_{r=a} = \frac{\partial}{\partial r}\{r(m\pi^{(w)})\}_{r=a}, \quad (5.33.b)$$

$$\frac{\omega\varepsilon_1}{c}\{r(e\pi^{(i)} + e\pi^{(s)})\}_{r=a} = \frac{\omega\varepsilon_2}{c}\{r(e\pi^{(w)})\}_{r=a}, \quad (5.33.c)$$

$$\frac{\omega\mu_1}{c}\{r(m\pi^{(i)} + m\pi^{(s)})\}_{r=a} = \frac{\omega\mu_2}{c}\{r(m\pi^{(w)})\}_{r=a}. \quad (5.33.d)$$

The scalar potentials for scattered field and the field inside the sphere take the same form as equation (5.29) and (5.30). Since the sphere's center is assumed to be at the origin, the radial component of the scalar potential for the field inside the sphere should be chosen such that the field remains finite. Consequently for the scalar potentials inside the sphere,  $e\pi^{(w)}$  and  $m\pi^{(w)}$ , the Hankel function,  $h_l(kr)$ , is replaced with the Bessel function of the first kind,  $J_l(kr)$ , which is finite at the origin.

$$r^e\pi^{(w)} = \frac{1}{k_2^2}\sum_{l,m} {}^eA_{l,m} \psi_l(k_2r)Y_{m,l}, \quad (5.34)$$

$$r^m\pi^{(w)} = \frac{c}{\omega k_2}\sum_{l,m} {}^mA_{l,m} \psi_l(k_2r)Y_{m,l}. \quad (5.35)$$

Here  $k_2 = \frac{\omega\sqrt{\varepsilon_2\mu_2}}{c}$  is the propagation constant for the sphere. The scalar

potential for the scattered field takes the same radial function as dipole field

$$r^e \pi^{(s)} = \frac{1}{k_1^2} \sum_{l,m} {}^e B_{l,m} \xi_l(kr) Y_{m,l}, \quad (5.36)$$

$$r^m \pi^{(s)} = \frac{c}{\omega k_1} \sum_{l,m} {}^m B_{l,m} \xi_l(kr) Y_{m,l}. \quad (5.37)$$

Equations (5.29), (3.30), and (5.34-37) are replaced into the boundary condition equation set (5.33) to determine the scattering coefficients.

$$\frac{1}{\varepsilon_1 \sqrt{\varepsilon_1}} \frac{\partial}{\partial r} \{ {}^e B_{l,m} \xi_l(k_1 r) + \frac{1}{\sqrt{l(l+1)}} (-a_E) \psi_l(k_1 r) {}^e B_{l,m} \}_{r=a} = \frac{1}{\varepsilon_2 \sqrt{\varepsilon_2}} \frac{\partial}{\partial r} \{ {}^e A_{l,m} \psi_l(k_2 r) \}_{r=a}, \quad (5.38.a)$$

$$\frac{\partial}{\partial r} \{ \psi_l(kr) \frac{1}{\sqrt{l(l+1)}} a_M(l, m) + {}^m B_{l,m} \xi_l(k_1 r) \}_{r=a} = \frac{\partial}{\partial r} \{ {}^m A_{l,m} \psi_l(k_2 r) \}_{r=a}, \quad (5.38.b)$$

$$\frac{\omega \varepsilon_1}{c} \frac{1}{\varepsilon_1 \sqrt{\varepsilon_1}} \{ {}^e B_{l,m} \xi_l(k_1 r) + \frac{1}{\sqrt{l(l+1)}} (-a_E) \psi_l(k_1 r) {}^e B_{l,m} \}_{r=a} = \frac{\omega \varepsilon_2}{c} \frac{1}{\varepsilon_2 \sqrt{\varepsilon_2}} \{ ({}^e A_{l,m} J_l(k_2 r)) \}_{r=a}, \quad (5.38.c)$$

$$\frac{1}{k_1} \{ \psi_l(k_1 r) \frac{1}{\sqrt{l(l+1)}} a_M(l, m) + \xi_l(k_1 r) {}^m B_{l,m} \}_{r=a} = \frac{1}{k_2} \{ {}^m A_{l,m} \psi_l(k_2 r) \}_{r=a}. \quad (5.38.d)$$

${}^m B_{l,m}$  and  ${}^e B_{l,m}$  which characterize the scattered wave are derived by elimination of  ${}^m A_{l,m}$  and  ${}^e A_{l,m}$  from the above equation set.

$${}^e B_{l,m} = - \frac{\sqrt{\varepsilon_2} \psi'_l(k_1 a) \psi_l(k_2 a) - \sqrt{\varepsilon_1} \psi'_l(k_2 a) \psi_l(k_1 a)}{\sqrt{\varepsilon_1} \psi'_l(k_2 a) \xi_l(k_1 a) - \sqrt{\varepsilon_2} \xi'_l(k_1 a) \psi_l(k_2 a)} \frac{a_E(l, m)}{\sqrt{l(l+1)}}, \quad (5.39)$$

$${}^m B_{l,m} = \frac{\sqrt{\varepsilon_1} \psi'_l(k_1 a) \psi_l(k_2 a) - \sqrt{\varepsilon_2} \psi'_l(k_2 a) \psi_l(k_1 a)}{\sqrt{\varepsilon_2} \xi'_l(k_1 a) \psi_l(k_2 a) - \sqrt{\varepsilon_1} \psi'_l(k_2 a) \xi'_l(k_1 a)} \frac{a_M(l, m)}{\sqrt{l(l+1)}}. \quad (5.40)$$

### 5.5.3 Verification of Calculations

The analytical solution provided in section 5.5.1 and 5.5.2 can be easily verified by setting the location of the radiating dipole far away from the sphere, such that the dipole's field mimics a plane wave. Consequently for sufficiently distanced dipole from the sphere, it is expected that the calculations converge to the Mie theory. The following configuration is set for the test, as shown in figure 5.5 where  $d/\lambda_{radiation} \sim 8e^7$ . The sphere is placed at the origin and the dipole on the z axis and far away from the sphere. Without the loss of generality the polarization of the dipole is chosen to be in  $\hat{x}$  direction.

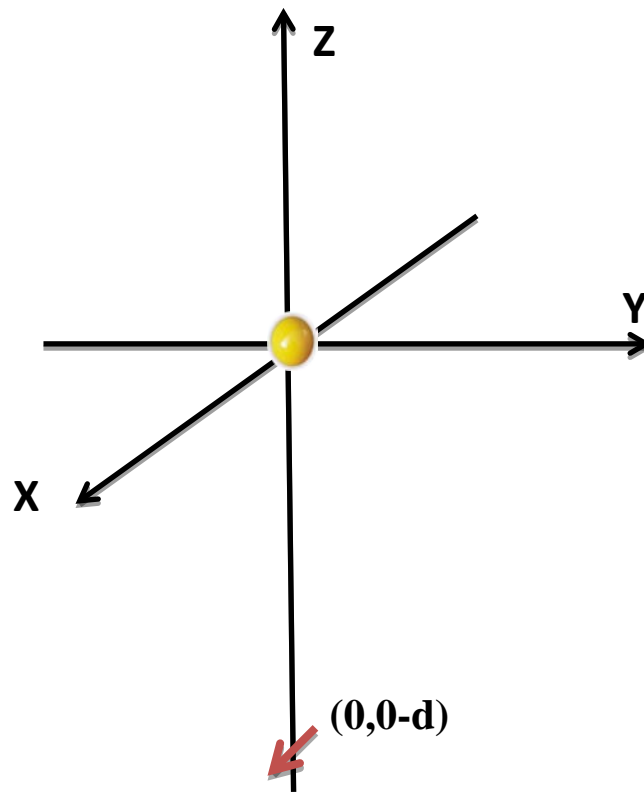


**Figure 5.5** The test set up. The sphere is located at the far-field region of the dipole

Since dipole is located on (0, 0, -d),  $\theta = \pi$ , and the only nonzero values of  $a_E$  and  $a_M$  are for  $m=0$  and  $\pm 1$ . For the following values of  $m$ , equations (5.15) and (5.17) can be written in simpler form,

$$m = 1$$

$$m = -1$$

$$\vec{\varepsilon} = (-1)^{l-1} \left( \frac{l(l+1)(2l-1)}{4\pi} \right)^{\frac{1}{2}} (1, -i, 0), \quad \vec{\varepsilon} = (-1)^l \left( \frac{l(l+1)(2l-1)}{4\pi} \right)^{\frac{1}{2}} (1, i, 0) \quad (5.41.a)$$

$$\vec{\varepsilon}^\dagger = (-1)^l \left( \frac{l(l+1)(2l+3)}{4\pi} \right)^{\frac{1}{2}} (1, -i, 0), \quad \vec{\varepsilon}^\dagger = (-1)^{l+1} \left( \frac{l(l+1)(2l+3)}{4\pi} \right)^{\frac{1}{2}} (1, i, 0) \quad (5.41.b)$$

$$\vec{M} = (-1)^l \left( \frac{l(l+1)(2l+1)}{4\pi} \right)^{\frac{1}{2}} (1, -i, 0), \quad \vec{M} = (-1)^l \left( \frac{l(l+1)(2l+1)}{4\pi} \right)^{\frac{1}{2}} (1, i, 0) \quad (5.41.c)$$

and for  $m=0$

$$\vec{\varepsilon} = 2l(-1)^l \left( \frac{(2l-1)}{4\pi} \right)^{\frac{1}{2}} (0, 0, 1), \quad \vec{\varepsilon} = (-1)^l \left( \frac{l(l+1)(2l-1)}{4\pi} \right)^{\frac{1}{2}} (0, 0, 1), \quad \vec{M} = 0 \quad (5.41.d)$$

With the simplified expressions in equation (5.41),

$$a_E^d(l, \pm 1) = \pm ik^3 \sqrt{\pi} (-1)^l (2l+1)^{-\frac{1}{2}} (p_x \pm ip_y) \times [lh_{l+1}^1(kd) - (l+1)h_{l-1}^1(kd)]$$

$$a_E^d(l, 0) = ik^3 \sqrt{\pi} (-1)^l (p_z) \times \left[ \frac{4\pi l(l+1)}{2l+1} \right]^{\frac{1}{2}} \times [h_{l+1}^1(kd) + h_{l-1}^1(kd)], \quad (5.42.b)$$

$$a_M^d(l, \pm 1) = ik^3 \sqrt{\pi} (-1)^l (\pi(2l+1))^{\frac{1}{2}} (p_x \pm ip_y) \times h_l^1(kd), \quad (5.42.c)$$

$$a_M^d(l, 0) = 0. \quad (5.42.d)$$

For  $d \gg a$  the spherical Hankel function in equation (5.42) is approximated by the following expression

$$h_l^1(z) \sim (-i)^{l+1} \frac{e^{iz}}{z}. \quad (5.43)$$

Equation (5.43) simplifies equation (5.42) to the following form,

$$a_E^d(l, \pm 1) \sim \mp (i)^{l+1} k^3 \sqrt{\pi(2l+1)} (p_x \pm ip_y) \times \frac{e^{ikd}}{kd}, \quad (5.44.a)$$

$$a_E^d(l, 0) \sim 0, \quad (5.44.b)$$

$$a_M^d(l, \pm 1) \sim - (i)^{l+2} k^3 \sqrt{\pi(2l+1)} (p_x \pm ip_y) \times \frac{e^{ikd}}{kd}, \quad (5.44.c)$$

$$a_M^d(l, 0) = 0. \quad (5.44.d)$$



For a dipole oriented in x direction  $a_E^d$  and  $a_M^d$  are derived by an appropriate linear combination of equations (5.44.a) and (5.44.c),

$$a_E^d(l, \pm 1) \sim (i)^{l+1} k^3 \sqrt{\pi(2l+1)} (p_x) \times \frac{e^{ikd}}{kd} (\delta_{m,-1} - \delta_{m,+1}), \quad (5.45.a)$$

$$a_M^d(l, \pm 1) \sim - (i)^{l+2} k^3 \sqrt{\pi(2l+1)} (p_x) \times \frac{e^{ikd}}{kd} (\delta_{m,-1} + \delta_{m,+1}). \quad (5.45.b)$$

$a_E^d$  and  $a_M^d$  in equation (5.27) and (5.18) are replaced with (5.45.a) and (5.45.b) to derive the radial component of E-field and H-field for dipole in figure 5.5.

$$H_{dipole}^r = \sum_{l,m} i^{l-1} \frac{e^{ikd}}{d} a_M(l, m) \frac{\psi(kr)}{(r)^2} P_l^1(\cos\theta) \sin\varphi, \quad (5.46.a)$$

$$E_{dipole}^r = \sum_{l,m} i^{l-1} \frac{\omega e^{ikd}}{c\mu d} a_E(l, m) \frac{\psi(kr)}{\kappa(r)^2} P_l^1(\cos\theta) \cos\varphi. \quad (5.46.b)$$

For convenience in calculations normalization factor of  $\frac{c\mu d}{k\omega} e^{-ikd}$  is introduced. This factor is introduced to compensate the difference between magnetic vector potential of a plane wave in [15] and magnetic vector potential of dipole, equation (5.2) in far-field region.  $H_{dipole}^r$  and  $E_{dipole}^r$  are:

$$H_{dipole}^r = \sum_{l,m} i^{l-1} \frac{kc}{\omega\mu} a_M(l, m) \frac{\psi(kr)}{(kr)^2} P_l^1(\cos\theta) \sin\varphi, \quad (5.47.a)$$

$$E_{dipole}^r = \sum_{l,m} i^{l-1} a_E(l, m) \frac{\psi(kr)}{(kr)^2} P_l^1(\cos\theta) \cos\varphi. \quad (5.47.b)$$

The two following properties of spherical harmonics are used in derivation of equation (5.47)

$$\begin{cases} (Y_{l,m} + (-1)^m Y_{l,-m}) = -2 \sqrt{\frac{2l+1}{4\pi l(l+1)}} P_l^m(\cos\theta) \cos(m\varphi) & m > 0 \\ (Y_{l,m} + (-1)^m Y_{l,-m}) = -2i \sqrt{\frac{2l+1}{4\pi l(l+1)}} P_l^{|m|}(\cos\theta) \sin(|m|\varphi) & m < 0 \end{cases}. \quad (5.48)$$

Equation (5.47) is identical to the given expressions in [15] for spherical expansion for H-field and E-field of a plane wave. This complete agreement proves the accuracy of the calculation for scattering due to radiating dipole. The Debye potentials and scattering coefficients are calculated with the same routine introduced in section 5.5.2,

$$r^m \pi = \frac{1}{k^2} \sum_{l,m} \frac{kc}{\omega\mu} \alpha_{l,m} \psi(kr) P_l^1(\cos\theta) \sin\varphi, \quad (5.49.a)$$

$$r^e \pi = \frac{1}{k^2} \sum_{l,m} \beta_{l,m} \psi(kr) P_l^1(\cos\theta) \sin\varphi. \quad (5.49.b)$$

where  $\alpha_{l,m}$  and  $\beta_{l,m}$  is  $i^{l-1} \frac{2l+1}{l(l+1)}$ . The fields inside of the sphere are described in the same fashion

$$r^m \pi = \frac{1}{k_2^2} \sum_{l,m} \frac{k_2 c}{\omega\mu} {}^m A_{l,m} \psi_l(k_2 r) P_l^1(\cos\theta) \sin\varphi, \quad (5.50.a)$$

$$r^e \pi^{(w)} = \frac{1}{k_2^2} \sum_{l,m} {}^e A_{l,m} \psi_l(k_2 r) P_l^1(\cos\theta) \cos\varphi. \quad (5.50.b)$$

Here  $k_2 = \frac{\omega\sqrt{\epsilon_2}}{c}$  is the propagation constant for the sphere. The Debye potential for the scattered fields are,

$$r^m \pi = \frac{1}{k_1^2} \sum_{l,m} \frac{k_1 c}{\omega\mu} {}^m B_{l,m} h_l(k_1 r) P_l^1(\cos\theta) \sin\varphi, \quad (5.51.a)$$

$$r^e \pi^{(w)} = \frac{1}{k_1^2} \sum_{l,m} {}^e B_{l,m} h_l(k_1 r) P_l^1(\cos\theta) \cos\varphi. \quad (5.51.b)$$

After imposing the boundary condition provided in equation (5.33.a), the scattering coefficients are,

$${}^e B_{l,m} = i^{l+1} \frac{2l+1}{l(l+1)} \frac{\sqrt{\epsilon_2} \psi'_l(k_1 a) \psi_l(k_2 a) - \sqrt{\epsilon_1} \psi'_l(k_2 r) \psi_l(k_1 a)}{\sqrt{\epsilon_1} h'_l(k_1 a) \psi_l(k_2 a) - \sqrt{\epsilon_2} h_l(k_1 a) \psi_l(k_2 a)}, \quad (5.52.a)$$

$${}^m B_{l,m} = i^{l+1} \frac{2l+1}{l(l+1)} \frac{\sqrt{\epsilon_2} \psi'_l(k_2 a) \psi_l(k_1 a) - \sqrt{\epsilon_1} \psi'_l(k_1 r) \psi_l(k_2 a)}{\sqrt{\epsilon_1} h'_l(k_1 a) \psi_l(k_2 a) - \sqrt{\epsilon_2} h_l(k_1 a) \psi_l(k_2 a)}. \quad (5.52.b)$$

The scattering coefficients in equation (5.52) are the exact given expression provided in Mie theory. An algorithm is developed by MATLAB for the general

case of field scattered by arbitrarily located and polarized dipole, section 5.5.1 and 5.5.2. To test the code and verify the calculations the dipole is set far away enough. Figure 5.6 (a) presents the field of the E-field's intensity on the z axis. The radius and index of refraction of the sphere is  $1\mu m$  and 1.6 respectively and the wavelength of the radiation is  $248\text{ nm}$ . For the reference, a sphere with the same configuration is illuminated with plane wave ( $\lambda = 248\text{ nm}$ ) in COMSOL multiphysics. Figure 5.6 (b) presents the intensity of field inside and outside of the sphere on the z axis. As can be seen the intensity of E-field in figure 5.6 (a) and figure 5.6 (b) are identical which reveals the validity of the calculations and the accuracy of the developed algorithm.

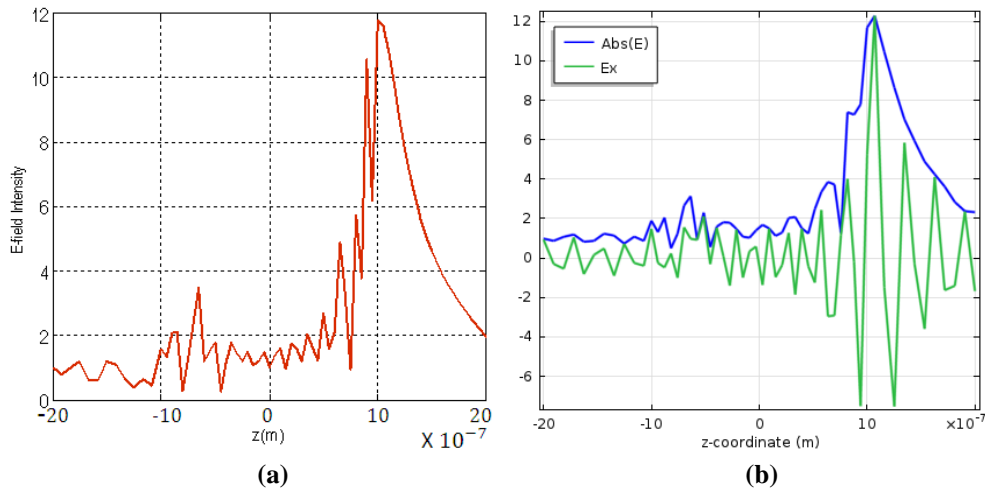


**Figure 5.6** The intensity of E-Field, inside and outside of a dielectric sphere (a) Full wave based algorithm in MATLAB for general case of dipole radiation in presence of sphere when dipole is set far away from the sphere as shown in figure 5.5 (b) COMSOL multiphysics simulation the same sphere shined by a plane wave

The lower accuracy of result in figure 5.6 (b) was due to the increment in simulation time for denser mesh in COMSOL, however the algorithm developed in MATLAB, based on the exact solution of Maxwell equations provided the result with higher accuracy and in considerably higher pace.

### 5.5.4 Poynting Vector Lines Extrapolation and Virtual Image Formation

The intensity distribution around particles with feature sizes much bigger than  $\lambda$  can be estimated by ray tracing. However for objects smaller than  $\lambda$ , geometrical optics suffers lack of accuracy. The Poynting vector ( $S = E \times H$ ) specifies the magnitude and direction of the rate of transfer of electromagnetic energy at all points of space [16]. Consequently, in near field region the Poynting vector lines can accurately map the intensity distribution around and inside of the particle. The purpose here is to plot the Poynting vector in order to observe the mechanism of image formation in the near field. The total time-averaged Poynting vector can be written as,

$$\langle S_{out} \rangle = 1/2 \operatorname{Re}(E_{out} \times H_{out}^*), \quad (5.53.a)$$

$$\langle S_{in} \rangle = 1/2 \operatorname{Re}(E_{in} \times H_{in}^*), \quad (5.53.b)$$

where *out* and *in* refer to the distribution outside and inside of the particle respectively. The relation between the  $r$  and  $\theta$  components of Poynting vector in the x-z plane ( $\varphi = 0$ ) are [16],

$$\frac{d_r}{d_\theta} = r \frac{\langle S \rangle_r}{\langle S \rangle_\theta}. \quad (5.54)$$

The near-field virtual image formation is investigated for the following configuration, figure 5.7.

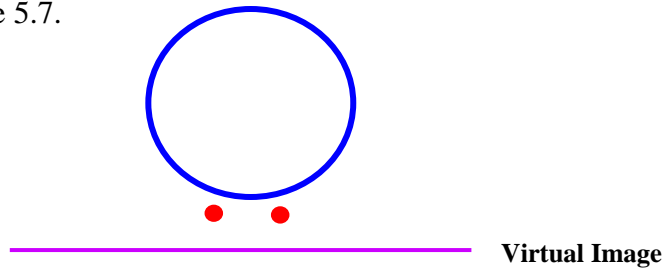


**Figure 5.7** Virtual image formation investigation

The system of two dipole with spacing  $d$ , one dipole is located at  $(x, z) = (-d/2, z_d)$  and the other one is at  $(x, z) = (d/2, z_d)$ , are located in the nanometric distance below the dielectric microsphere. The exact solutions of the incident field, scattered field and field inside the microsphere are calculated based on derived expression in sections 5.5.2 and 5.5.3. However it should be noted that the region of interest in this problem is divided to two sub-regions; (i) The sub-region where the distance of the dipoles from the origin ( $r'$ ) is greater than the distance of the point which the field is calculated ( $r$ ), ( $r' > r$ ) (ii) The sub-region where ( $r' < r$ ). For the first sub-region the calculation provided in sections 5.5.2 and 5.5.3 is directly used however for the second sub-region it is necessary to interchange  $j_l$  and  $h_l^1$  for  $r'$  and  $r$  in equation (5.4) and hence to all following equations to conduct calculation correctly.

The Poynting vectors inside and outside of the microsphere are calculated by solving the differential equation provided in equation (5.54). Since we are interested in the virtual image formation, the lines of Poynting vector are plotted mostly for the lower half of the microsphere. One can estimate the possible magnification in the near field on the basis of reciprocity principle. According to this principle, two points on the line of Poynting vector can be conjugated if the propagation direction is changed to the opposite [10], as shown in figure 5.8.

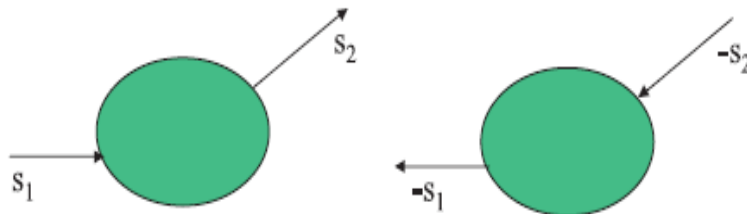


**Figure 5.8** Reciprocal configurations [10]

Thus forward and backward flow arises along the same Poynting vector line. Based on the reciprocity principle, the extrapolation of the Poynting vector line could be done by plotting a tangential line to the line with some curvature. The results of Poynting vector computation and investigation of virtual image formation in near-field, for three different spacing,  $d$ , are shown in figure 5.9, 5-11, and 5-12. The radius and index of the refraction,  $n$ , of the microsphere and the working wavelength are taken from [6] which is the origin of the inspiration for this chapter. The radius and dielectric permittivity of the sphere is  $a = 2.37 \mu m$  and  $n = 1.46$  respectively and the working wavelength is  $\lambda = 600 nm$ . For the first trial the spacing is set to be  $d = 100 nm$ ; figure 5.9 (a) demonstrates the Poynting vector lines inside and outside of the sphere. As is can be seen the lines are not straight line anymore which verifies the inefficiency of ray tracing for virtual image formation inspection in the near-field. Figure 5.9 (a) presents the extrapolation of Poynting vector and magnified virtual image formation in the virtual image plane. As is can be seen, the virtual images of two point dipoles are circles with magnified radius in comparison with the dipole. The spacing between the dipoles is also magnified to the factor  $1.8 \times a$ , which is around  $426.6 nm$ , hence the magnification factor of x4 is achieved.

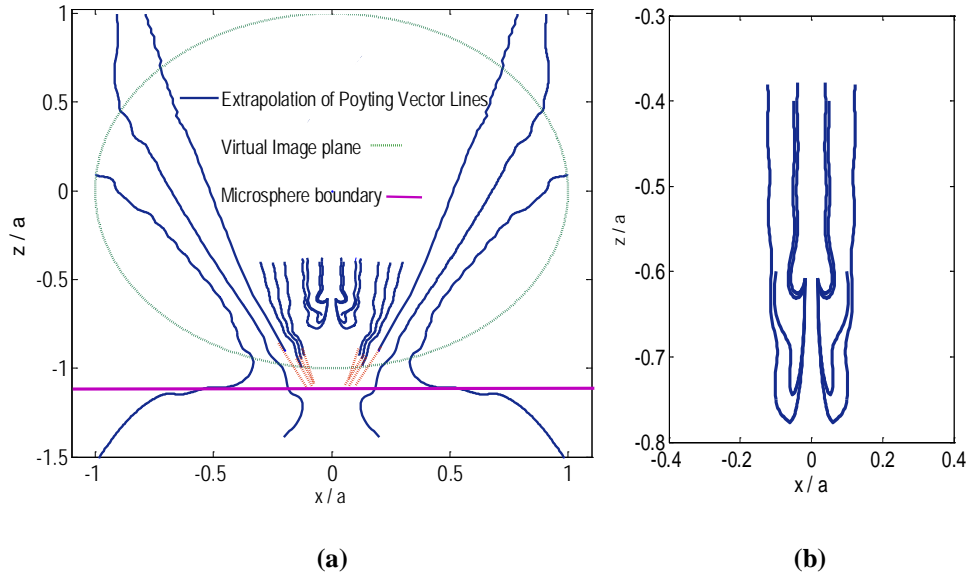


**Figure 5.9** Magnified virtual image formations in the near-field (a) Extrapolation of Poynting vector. Solid navy lines represent the Poynting vector found by equation (5.54), dashed green line is the boundary of microsphere, and dashed red lines are used to extrapolate the Poynting vector lines. The image plane is located 273 nm below the microsphere (b) energy vortex formation

As the diffraction limit at  $\lambda = 600 \text{ nm}$  is around  $333 \text{ nm}$ , the magnified virtual image is detectable with conventional optical microscope and far-field imaging of an object with subwavelength feature is possible. The peculiar phenomenon that contributes significantly to the virtual image formation is in fact the energy vortices formed inside the particle as is shown in more detail in figure 5.9 (b). There exist few lines which remain inside the particle; this phenomenon might be analogous to the internal reflection caused inside the dielectric nanoparticle with small refractive index and radius much bigger than  $\lambda$  as shown in figure 5.10. For the small value of  $n$ , the “*input window*” becomes very small. Figure 5.10 illustrates an interesting effect: a particle can transfer energy from the near-field region to a far-field region through a very small “*effective aperture*” [16].

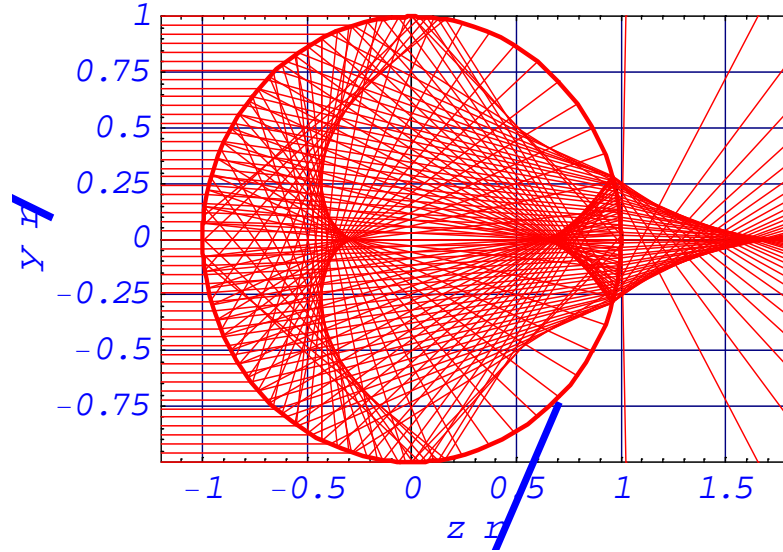


**Figure 5.10** Ray-tracing for a big particle with small  $n, r$  is the radius of the particle [16]

Analogously the formation of the energy vortexes which depends on the specific range of radius for microspheres,  $2 \mu m < a < 9 \mu m$  [6], can considerably contribute to the success of far-field imaging with dielectric microspheres. In the second set, the dipoles are located closer to each other,  $d = 40 \text{ nm}$ . As it is demonstrated in figure 5.11 (a), the extrapolated Poynting vector lines converge to each other and the images of individual dipole sources are not distinguishable from each other. Figure 5.11 (b) presents the energy vortex formed in this case. It should be noted that the energy vortexes shown in figure 5.9, 5.11, and 5.12 contain more intensity lines that are not presented here as the developed algorithm for Poynting vector lines diverges for several initial points. However, for each case, enough number of Poynting vector lines are extrapolated to judge the success of imaging fairly. Another subject of interest is that *up to which spacing between the dipoles, the virtual image of individual sources is distinguishable in the image plane.*



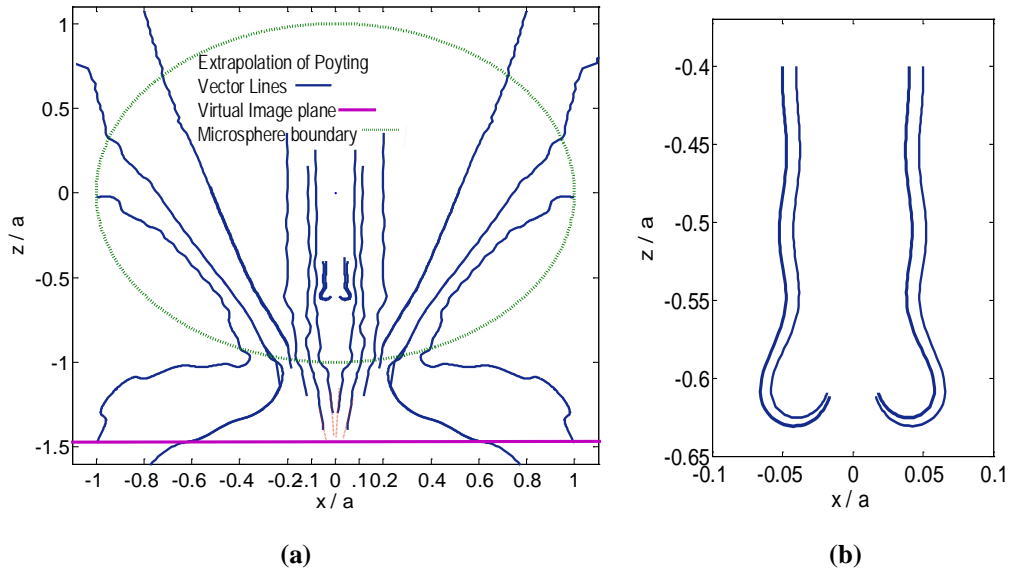


**Figure 5.11** Magnified virtual image formation in near field = 40 nm (a) Convergence of extrapolated intensity lines (b) Energy vortex

The ultimate spacing between two dipoles is found to be  $d = 64$  nm with the current version of the algorithm. Figure 5.12 demonstrates the formation of the virtual image of point dipoles in the image plane by extrapolating the Poynting vector lines and figure 5.12 (b) presents the energy vortex. It should be noted that the spacing of  $d = 50$  nm is experimentally reported in [6] which the current version of Poynting vector algorithm is unable to reconstruct. However the author believes that by slight improvement in the point-by-point iterative solution technique for the differential equation (5.54) the improved result can be provided shortly. In addition, the difference between the analytical prediction here and experimental demonstration in [6] might arise from the constructive effect of mutual near-field interaction of microsphere superlenses. Furthermore, it is experimentally shown that the gold coating layer on the anodic aluminum oxide surface not only enhanced the resolving power but also increased the magnificati-

-on factor of the microsphere superlens [6]. In addition it should be mentioned that this limit is determined in case that the virtual images merge to each other. However in the case that the two magnified virtual images are partially overlapping the far field imaging might be still possible depending on the overlapping percentile. Consequently, even higher resolution is achievable considering a threshold for the overlapping percentile.

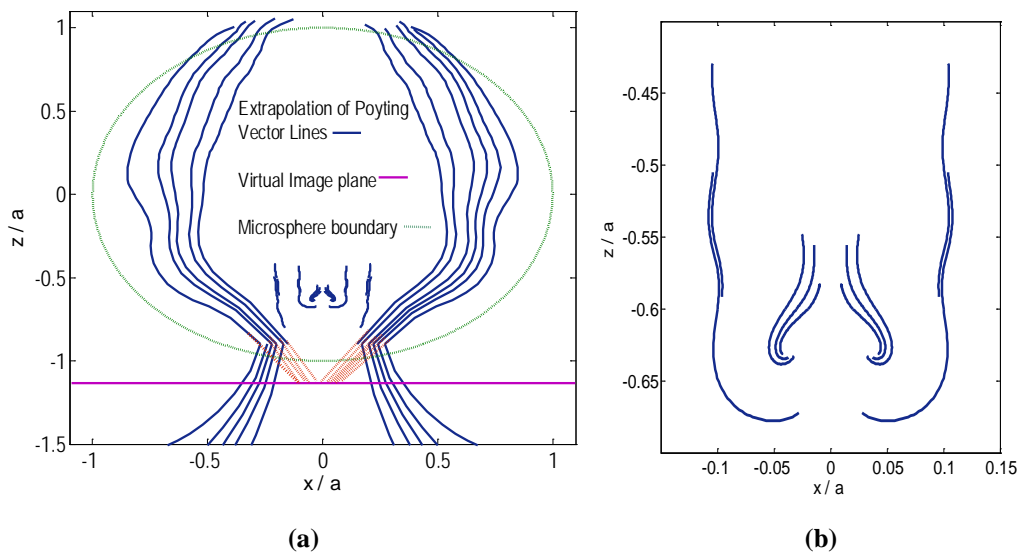


**Figure 5.12** Magnified virtual image formation in the near-field  $d = 64 \text{ nm}$  (a) Ultimate achievable resolution  $\approx \lambda/10$  (b) Energy vortex

Consequently the effect of surface contribution could also be one of the main reasons for the difference of the resolution predicted by calculation here and the resolution demonstrated experimentally in [6].

## 5.6 Conclusion

In this chapter a novel methodology based on rigorous multipole expansion is developed to unveil the mechanism of far-field subwavelength imaging with microscope nanoscope for the first time. A systematic methodology is proposed to unveil the mechanism of virtual image formation in the near field region. First the electromagnetic field radiated by arbitrarily located and polarized dipole is expanded in spherical coordinate by rigorous multipole expansion method. A dielectric sphere is then illuminated by the dipole and the explicit expressions are found for scattered field and the field inside the particle. An algorithm based on this full-wave solution is developed in MATLAB and the calculations are verified by reconstruction of Mie theory, when the dipole is set far away from the sphere. To investigate the image formation the Poynting vector lines are calculated by numerically solving a differential equation in  $x$ - $z$  plane as Ray tracing fails in near-field optics. It is revealed that the formation of energy vortexes inside the particle contributes considerably to the success of dielectric microsphere in far-field imaging of an object with subwavelength features. The image formation for three cases is investigated: (i) The dipoles are set 100 nm apart. In this case it is shown that the magnified virtual image is successfully formed in the virtual image

plane, and the image is magnified by factor  $\times 4$ . Hence the image is observable with conventional optical microscope and far-field imaging is realized. (ii) The spacing between the dipoles is decreased to 64 nm. In this case the virtual image of individual dipoles merges to each other in the image plane which reveals the ultimate resolution,  $\lambda/10$ , that can be achieved in the set up of microscope nanoscope reported in [6]. However the author believes that by refinement in the Poynting vector line calculation, more accurate result and probably higher achievable resolution can be predicted. In addition, the difference between the ultimate resolution predicted by calculation here and the resolution demonstrated experimentally in [6] might be due to the constructive effect of the surface. It is shown experimentally that the gold coating layer on the anodic aluminum oxide surface not only enhanced the resolving power but also increased the magnification factor of the microsphere superlens [6]. (iii) The spacing between the dipoles is decreased from 64 nm to 40 nm. In this case the virtual images of two dipoles are indistinguishable; hence no acceptable resolution is achieved.

## Reference

- [1] I. I. Smolyaninov, Y. J. Hung, & C. C. Davis, "Magnifying superlens in the visible frequency range." *Science* 315, 1699-1701 (2007).
- [2] Z. Liu, and X. Zhang et al. "Far-field optical hyperlens magnifying sub-diffraction-limited objects." *science* 315.5819: 1686-1686. (2007).
- [3] A. V. Itagi, and W. A. Challener. "Optics of photonic nanojets." *JOSA A* 22.12 :2847-2858, (2005).
- [4] J. Y. Lee "Near-field focusing and magnification through self-assembled nano-scale spherical lenses." *Nature* 460.7254: 498-501 (2009).
- [5] G. M. Whitesides , and B. Grzybowski. "Self-assembly at all scales." *Science* 295.5564: 2418-2421. (2002).
- [6] Z. Wang, W. Guo, L. Li, Z. Liu, B. Luk'yanchuk, Z. Chen,, & M. Hong, "The optical microscopy with virtual image breaks a record: 50-nm resolution imaging is demonstrated." *arXiv preprint arXiv:1006.4037* (2010).
- [7] V. V. Yakovlev, and B. Luk'yanchuk. "Multiplexed nanoscopic imaging." *Lasert Phys.* - 14.8 1065-1071:(2004).
- [8] C. Girard, and A. Dereux. "Near-field optics theories." *Rep. on Prog. in Phys.* 59.5: 657. (1996).
- [9] J. J. Diao "Optical resonance of metal-coated nanoshell." *Chinese Physics* 12.1 :100,(2003).
- [10] R. J. Potton, "Reciprocity in optics." *Reports on Progress in Physics* 67.5 (2004): 717.
- [12] J. D. Jackson ,” Classical Electrodynamics”,*Wiley*,(1999)
- [13] M. E. Rose, “Elementary Theory of Angular Momentum”, *Wiley*, (1995).
- [14] A. R. Edmonds, ”Angular Momentum in Quantum Mechanics” *Princeton* ,(1957)
- [15] M. Born, “Principle of Optics”,*Cambridge University Press*,(1999).
- [16] B. Luk'yanchuk. “Frontiers in Optical Bio-imaging and Microscopy,” Singapore, *ICMAT Conf.* June (2011).

# **CHAPTER 6**

## **COMCLUSION AND FUTURE WORK**

### **6.1 Conclusion**

The research conducted in this thesis is concentrated on the application of scattered light from metallic and dielectric particle in subwavelength imaging. Subwavelength imaging is of great importance in numerous applications such as extension of optical lithography to ultra-small scales, biomedical imaging, and optical and magnetic data storage.

The loss of evanescent waves in imaging with conventional optical system results in irrecoverable image imperfection which is crucial in nano-science. During the past decade, numerous efforts have been devoted to overcome diffraction limit. In spite of the impressive progress in this field, surface plasmon polariton (SPP) energy loss, sophistications in nanofabrication, specific laser sources, and parameter configuration of SPP excitation are factors which hamper far-field and near-field subwavelength imaging in the whole visible spectrum. In this dissertation, analytic and numerical investigation is allocated to the

application of the field that is scattered by metallic or dielectric nanoparticles, for advances in near-field and far-field subwavelength imaging. The main contributions and results can be summarized as follows:

1. For subwavelength imaging consistent with available laser sources, an aggregate of plasmonic nanoparticles with different shapes and orientations embedded in a dielectric host, is suggested for near-field tunable subwavelength imaging. Appropriate geometrical specifications are allocated to the size, filling fraction, and probability distribution function (PDF) of metallic inclusions to suggest a well-defined structure for the metal-dielectric composite. This structure is used in next chapters to approximate the effective optical property of metal-dielectric composites by Maxwell-Garnett theory accurately. The effect of the size of nanoparticle is studied through Mie scattering theory; it is shown that the high frequency extension of MG, Mie Maxwell-Garnett (MGG), is reduced to the classical MG in the quasi static limit. The dielectric function of silver nanoparticles with radius smaller than silver's mean free path length is corrected in order to take into account the intrinsic size effect. In order to avoid the quantum effect and inter-particle mutual interaction the lower bound ( $r_{min} = 2 \text{ nm}$ ) and upper bound ( $r_{max} =$

10 nm) are set for the radius of the nanoparticles. In addition it is shown by scattering matrix method that as long as the inclusions are not overlapping and their radius size is restricted in quasistatic limit the effective permittivity is reduced to the expression derived by MG theory. It is concluded that if the single scattering is the dominant mechanism, the effective permittivity predicted by MG theory is quite accurate regardless of the statistical distribution of the particles, as long as the distribution is uniform. Consequently MG theory is quite accurate even at high concentrations (52% for full lattice) as long as the particles are distributed uniformly.

2. Based on the geometrical model developed for metal-dielectric composite, the methodology to design single and multilayer flat metamaterial lenses is presented. The composite layers of Ag spherical inclusions immersed in SiO<sub>2</sub> host are proposed as lens and implementable geometrical dimensions and composition have been determined with optimization. The sub-wavelength imaging is realized for different wavelengths in optical range. In addition metallic composites with deep subwavelength inclusions are also beneficial for elimination of the hotspots in the images of metallic superlens.



3. Subwavelength imaging with single layer and multilayer composite slabs which are made of non-spherical plasmonic inclusions embedded in dielectric host medium is studied. For composite made of randomly oriented non-spherical inclusions it is shown that by increment in the eccentricity of nanoparticles, the resonance peak of effective index of refraction is red shifted; hence the different shapes of nanoparticle is beneficial to design an optical system which is compatible with available resources. An optimum values for filling fraction, incident field's frequency, and slabs' thickness are found for single layer and multi layer lensing system.
4. As effective refraction index of a composite with aligned nano ellipsoid is anisotropic, a fully analytical algorithm is developed to investigate light interaction with arbitrary anisotropic layered structure. The explicit expressions are derived for the polarizations of the electric and magnetic field in general anisotropic medium. Based on the vector fields' polarizations, a procedure is introduced to calculate the transmission matrix for the structure with arbitrary numbers of anisotropic layers. This algorithm is suitable to investigate the near-field/far-field electromagnetic

wave interaction at any angle of incidence for numerous intriguing applications.

5. It is shown that the composite slab with aligned non-spherical inclusions is not only capable of realizing the subwavelength imaging at different wavelengths but also it is more robust to the material loss due to its different mechanism of imaging. Consequently for two composite slabs with the same thickness, one formed from randomly oriented inclusions (isotropic) and the other formed by aligned inclusions (anisotropic) of same shape and same size, it is shown that the image formed in the image plane by anisotropic slab has higher intensity in comparison with image formed by isotropic slab. Hence anisotropic slabs offer better signal to noise ratio in the image plane. Owing to its specific dispersion curve, it is also analytically shown that the anisotropic slab can preserve waves with higher tangential component of wave vector which results in higher resolution; it is demonstrated while composite with randomly oriented inclusions (isotropic) fails to resolve two Gaussian pulses spaced 60 nm, the composite with the same thickness made of aligned inclusion of same shape and size, successfully resolves the pulses in the image plane.

6. A novel methodology based on rigorous multipole expansion is developed to unveil the mechanism of far-field subwavelength imaging with dielectric microparticle for the first time. The crucial role of the evanescent components of the field in the near-field zone brings challenges to theoretical simulation; hence an analytic numeric solution based on the full set of Maxwell equations is developed to unveil the mechanism of virtual image formation in the near field region. An algorithm based on the analytic solution is developed in MATLAB, and the calculations are verified by reconstruction of Mie theory, when the dipole is set far away from the sphere. To investigate the image formation, the Poynting vector lines are calculated by numerically solving a differential equation in x-z plane as Ray tracing fails in near-field optics. It is revealed that the formation of energy vortexes inside the particle contributes considerably to the success of dielectric microsphere in far-field imaging of an object with subwavelength features.

## **6.2 Suggestions for future work**

1. The loss generated by the surface plasmon hampers the quality of subwavelength imaging with metal based superlenses i.e. metal-dielectric composite super lens crucially. However active optical

coating for nano particle can alleviate the loss drawback considerably. The Maxwell-Garnett effective medium theory can be extended for core-mantel particles in a host medium as shown in section 4 of chapter two. Hence, much higher resolution is predictable for active metal dielectric composites.

2. Our initial investigation has shown that for anisotropic layered superlens, gyrotropy could be beneficial upon careful design of permittivity tensor elements. In this dissertation the optical axis of nanoparticles is aligned to the lens's coordinate, consequently the effective permittivity tensor is diagonal. The gyrotropy can be achieved by an appropriate rotation of aligned non-spherical nanoparticle respective to the lens coordinate.
3. Theoretical modeling of mutual near-field interaction between dielectric micro particles in far-field subwavelength imaging with dielectric micro particles is suggested. In addition, as the microspheres are placed on the surface with subwavelength features the effect of surface can be analytically modeled for more accurate theoretical prediction. For instance it is shown experimentally that the gold coating layer on the anodic aluminum oxide surface not

only enhanced the resolving power but also increased the magnification factor of the microsphere superlens.

## List of Publication

### Journal

- [1] **Kiasat ,Y.** Alphones, A . “A CRLH CPW leaky-wave antenna with reduced beam squinting. “Proceeding of *APMC Conference*, Macau December 2008.
- [2] Hegde, R.S., Szabo, Z., Yew Li Hor., **Kiasat, Y.**, Er Ping Li., & Hoefler, W.J.R. “ The Dynamics of Nanoscale Superresolution Imaging With the Superlens.” *IEEE Transactions on Microwave Theory and Techniques* , October 2011.
- [3] **Y. Kiasat**, Z. Szabo, X. Chen, and E. Li, "Light interaction with multilayer arbitrary anisotropic structure: an explicit analytical solution and application for sub-wavelength imaging", *Journal of the Optical Society of America*, B, Vol. 31, pp. 648-655, 2014.
- [4] Szabo,Z. **Kiasat, Y.**, & Er Ping ,L” Sub-Wavelength Imaging with Composite Material”, *Optical Society of America*, B, Vol. 31.6, pp. 1298-1307, 2014
- [5] **Kiasat, Y** ,Szabo,Z., & Er Ping ,L” Optical Metamaterial for Tunable Low Loss Sub-wavelength Imaging” manuscript unver priparation
- [6] **Kiasat, Y.** ,Lukyanchuk,B., & Er Ping ,L. “Ultimate achievable Resolution with Nanoscope : Analytical Explanation of Magnified Near-Field Virtual image” ,manuscript under preparation.

### Conference

- [1] Szabo,Z. **Kiasat, Y.**, & Er Ping ,L. “Composite Materials for, Sub-wavelength Imaging.” *MRS Conference*, Sanfransisco, April 2011.
- [2] **Kiasat, Y.** Szabo,Z.,& Er Ping ,L.” Advances in Subwavelength Imaging with Composite-Dielectric Multilayer Structures “*ICMAT Conference*, Singapore ,June 2011.
- [3] **Kiasat, Y.** Szabo,Z., & Er Ping ,L.” Sub-Wavelength Imaging with Ellipsoidal Nano-Particles” *Metamaterial Workshop*, Singapore, June 2011.
- [4] Szabo,Z. **Kiasat, Y.**, & Er Ping ,L.” Isotropic Metal-Dielectric Composites for Subwavelength Imaging” *Meta 2012 Conference*, Presentation ,Paris, April 2012.
- [5] **Kiasat, Y.** ,Lukyanchuk,B., & Er Ping ,L. “Analytical Explanation of Superresolution with Virtual Image in the Near Field”, *Meta13 Conference* , Presentation ,Sharjah,United Arab Emirates, March 2013.

[6] **Kiasat, Y** ,Szabo,Z., & Er Ping ,L. “Sub-Wavelength Imaging with Non-Spherical Plasmonic Nano-particles”,*Meta13 Conference* , Presentation ,Sharjah,United Arab Emirates,March2013.

[7] **Kiasat, Y** ,Szabo, Z., Xudong, C & Er Ping, L “Optical Metamaterial for Tunable Low Loss Sub-wavelength Imaging” *Meta14 Conference* , Presentation Singapore May 2014.